

Polymerization of MIP-1 chemokine (CCL3 and CCL4) and clearance of MIP-1 by insulin-degrading enzyme

Min Ren^{1,7}, Qing Guo^{1,7}, Liang Guo²,
Martin Lenz³, Feng Qian⁴, Rory R Koenen⁵,
Hua Xu⁶, Alexander B Schilling⁶,
Christian Weber⁵, Richard D Ye⁴,
Aaron R Dinner³ and Wei-Jen Tang^{1,*}

¹Ben-May Department for Cancer Research, The University of Chicago, Chicago, IL, USA, ²Department of Physics, Illinois Institute of Technology, Chicago, IL, USA, ³James Franck Institute, The University of Chicago, Chicago, IL, USA, ⁴Department of Pharmacology, University of Illinois at Chicago, Chicago, IL, USA, ⁵Institute for Molecular Cardiovascular Research, RWTH Aachen University, Aachen, Germany and ⁶Proteomics and Informatics Services Facility, University of Illinois at Chicago, Chicago, IL, USA

Macrophage inflammatory protein-1 (MIP-1), MIP-1 α (CCL3) and MIP-1 β (CCL4) are chemokines crucial for immune responses towards infection and inflammation. Both MIP-1 α and MIP-1 β form high-molecular-weight aggregates. Our crystal structures reveal that MIP-1 aggregation is a polymerization process and human MIP-1 α and MIP-1 β form rod-shaped, double-helical polymers. Biophysical analyses and mathematical modelling show that MIP-1 reversibly forms a polydisperse distribution of rod-shaped polymers in solution. Polymerization buries receptor-binding sites of MIP-1 α , thus depolymerization mutations enhance MIP-1 α to arrest monocytes onto activated human endothelium. However, same depolymerization mutations render MIP-1 α ineffective in mouse peritoneal cell recruitment. Mathematical modelling reveals that, for a long-range chemotaxis of MIP-1, polymerization could protect MIP-1 from proteases that selectively degrade monomeric MIP-1. Insulin-degrading enzyme (IDE) is identified as such a protease and decreased expression of IDE leads to elevated MIP-1 levels in microglial cells. Our structural and proteomic studies offer a molecular basis for selective degradation of MIP-1. The regulated MIP-1 polymerization and selective inactivation of MIP-1 monomers by IDE could aid in controlling the MIP-1 chemotactic gradient for immune surveillance.

The EMBO Journal advance online publication, 19 October 2010; doi:10.1038/emboj.2010.256

Subject Categories: signal transduction; structural biology

Keywords: chemokine; chemotactic gradient; insulin-degrading enzyme; MIP-1 polymerization; X-ray crystallography

Introduction

Chemokines (chemotactic cytokine) are 8–14 kDa peptides required for the recruitment of immune cells to the site of infection or inflammation and the development of secondary lymphoid organs (Allen *et al*, 2007). In humans, ~50 chemokines and 20 G-protein-coupled chemokine receptors form a complex signalling network (Wells *et al*, 2006). Macrophage inflammatory protein-1 (MIP-1), MIP-1 α and MIP-1 β (also known as CC motif chemokine ligand 3 (CCL3) and CCL4, respectively) were first found based on their proinflammatory properties (Wolpe *et al*, 1988). MIP-1 proteins are inducible in most immune cells in response to various proinflammatory stimuli and are potent chemoattractants to cells vital for innate and adaptive immunity (Menten *et al*, 2002; Maurer and von Stebut, 2004). MIP-1 can activate several chemokine receptors (CCR1 and CCR5), which initiate diverse cellular responses that regulate both acute and chronic inflammation. Consequently, the deregulation of MIP-1 proteins is associated with altered susceptibility to infection and human diseases (Kobayashi *et al*, 2002; Menten *et al*, 2002; Maurer and von Stebut, 2004). In addition, MIP-1 α knockout mice show altered inflammation reactions to the infection of various viral, bacterial and parasitic pathogens (Cook *et al*, 1995; Sato *et al*, 1999; Lindell *et al*, 2001). On the basis of the protective activity of haematopoietic stem cells and the inhibition of HIV-1 infections by their binding with the HIV-1 coreceptor, CCR5, MIP-1 proteins were also explored as possible therapeutics for cancer and AIDS (Graham *et al*, 1990; Dunlop *et al*, 1992; Cocchi *et al*, 1995; Horuk, 2009).

The monomer of CC chemokines is presumed to be the form that binds and activates their cognate receptors. However, several CC chemokines can form oligomers, and mutations that alter assembly lead to selective reduction of biological activities. For example, the ability of MIP-1 β , CCL5 (RANTES) and CCL2 (MCP-1) to oligomerize is crucial for their *in vivo* cellular recruitment into mouse peritoneal cavity (Proudfoot *et al*, 2003). The oligomerization of CCL5 is crucial for CCR1-mediated leukocyte arrest on inflamed endothelium (Baltus *et al*, 2003). Interestingly, oligomerization-defective mutations of CCL2 can suppress the normal and pathological responses to chemokines (Handel *et al*, 2008).

Of 28 CC chemokines, only MIP-1 α and MIP-1 β are highly acidic and can form high-molecular-weight (MW) aggregates (600 kDa or higher) (Graham *et al*, 1994). Such MIP-1 aggregates can form under physiologically relevant concentrations given the high levels of MIP-1 proteins that immune cells can secrete upon stimulation: up to 1 pg MIP-1 β per hour per dendritic cell (Sallusto *et al*, 1999). Consistent with this notion, MIP-1 and RANTES are secreted as high-MW aggregates from HIV-1-specific cytotoxic T lymphocyte (Wagner *et al*, 1998). The aggregation of MIP-1 proteins is dynamic and reversible, allowing the intricate regulation of the level of

*Corresponding author. Ben-May Department for Cancer Research, The University of Chicago, 929 E 57th Street, Chicago, IL 60637, USA.
Tel.: +1 773 702 4331; Fax: +1 773 702 4476;
E-mail: wtang@uchicago.edu

⁷These authors contributed equally to this work

Received: 20 May 2010; accepted: 23 September 2010

MIP-1 monomer (Graham *et al*, 1994). NMR structures of MIP-1 dimer reveal a common fold for CC chemokines, in which two anti-parallel β -strands formed by the N-terminal loop of MIP-1 constitute the primary contact of the MIP-1 dimer (Lodi *et al*, 1994). However, these structures neither offer a molecular basis for reversible MIP-1 aggregation nor explain how point mutations located outside the dimer interface (such as D27A and E67A in MIP-1 α) can effectively reduce MIP-1 aggregation (Graham *et al*, 1994; Czaplewski *et al*, 1999).

As in the case of other chemokines, MIP-1-mediated chemotaxis is highly regulated. Glycosaminoglycans (GAGs), a family of sulphated or acetylated polysaccharides composed of alternating glucosamine units that are the key components of proteoglycan, can fine-tune diverse mammalian physiological functions, including chemotaxis (Handel *et al*, 2005; Bishop *et al*, 2007). Proteoglycan-bound MIP-1 β on endothelium is used to effectively activate and induce the adhesion of circulating leukocytes for their extravasation (Tanaka *et al*, 1993). Furthermore, the binding of chemokines to GAGs is postulated to facilitate the formation of chemokine gradients and the presentation of chemokines to leukocytes in tissues (Kuschert *et al*, 1998; Lortat-Jacob *et al*, 2002). Consequently, GAG binding defective MIP-1 β mutant is inactive *in vivo* (Proudfoot *et al*, 2003). The activity of MIP-1 is also regulated by proteolysis (Wolf *et al*, 2008). Protease CD26/DPP IV can efficiently process MIP-1 proteins to more active forms, whereas cathepsin D can degrade and inactivate MIP-1 proteins (Proost *et al*, 2000; Wolf *et al*, 2003). The physiological relevance of such proteolytic modifications and their relationship with MIP-1 aggregation is currently unknown. Therefore, the protease(s) responsible for MIP-1 clearance and the mechanism of MIP-1 turnover *in vivo* remains to be elucidated.

In this report, we have determined polymer structures for MIP-1 α , MIP-1 β and an MIP-1 α deaggregation mutant, D27A, to reveal the molecular basis for the rod-shaped, double-helical polymer formation of MIP-1. Using small angle X-ray scattering (SAXS) and size exclusion chromatography (SEC), we show that MIP-1 proteins form polydisperse, rod-shaped polymers in solution and that heparin binding can profoundly affect MIP-1 polymerization. Our structures reveal that polymerization buries the receptor-binding sites of MIP-1. Consistent with this notion, we show that depolymerization mutations enhance the ability of MIP-1 α to arrest monocytes onto human endothelial monolayer under flow conditions. However, we also show that the same depolymerization mutations profoundly reduce the ability of MIP-1 α to recruit cells into mouse peritoneum.

In search of the physiologically relevant protease that could render the depolymerized MIP-1 mutants less effective for their *in vivo* function, we found that insulin-degrading enzyme (IDE) can selectively inactivate only monomeric MIP-1, and reduced expression of IDE leads to elevated MIP-1 levels in cultured cells. IDE is a 110 kDa ubiquitously expressed, zinc metalloprotease that has a key role in the clearance of insulin and amyloid β (A β), peptides vital for the development of diabetes mellitus and Alzheimer's disease (AD), respectively (Farris *et al*, 2003; Leissring *et al*, 2003; Sladek *et al*, 2007; Malito *et al*, 2008). Our recent structural studies revealed that two roughly equally sized, 55 kDa domains of IDE (IDE-N and IDE-C) form an enclosed catalytic

chamber (Shen *et al*, 2006). The unique properties of this catalytic chamber allow IDE to selectively bind substrates with a defined size, charge distribution, N-terminal position and tendency to form amyloid fibril (Shen *et al*, 2006; Malito *et al*, 2008; Manolopoulou *et al*, 2009; Guo *et al*, 2010). We also applied proteomics and structural analyses to decipher the molecular mechanism of MIP-1 inactivation by IDE.

Results

Polymer structures of MIP-1 α and MIP-1 β

To address the structural basis of MIP-1 aggregation, we purified and crystallized recombinant human MIP-1 α and MIP-1 β from *E. coli* in the absence of harsh conditions (such as low pH, high salt and organic solvent, which were used in the previous NMR analyses) (Table I). The chemotaxis activities of these proteins were comparable with commercial peptides (Supplementary Figure S1). MIP-1 proteins were readily crystallized in <3 days. The MIP-1 α and MIP-1 β structures were refined to 2.65 and 2.6 Å, respectively (Table I, Supplementary Figure S2).

MIP-1 α and MIP-1 β share 67% sequence identity and our MIP-1 polymer structures reveal that MIP-1 α and MIP-1 β form nearly identical rod-shaped, double-helical polymers (RMSD = 0.766 Å for MIP-1 α and MIP-1 β tetramers) (Figure 1). MIP-1 β polymer is slightly longer than MIP-1 α polymer (~0.3 Å per MIP-1 dimer). These structures can be viewed as polymerized MIP-1 dimers, a basic unit revealed by the NMR structures of MIP-1 proteins (Lodi *et al*, 1994; Czaplewski *et al*, 1999). In polymeric MIP-1, each dimer rotates 36° to bind to the adjacent dimer such that a decamer completes an 180° turn (Figure 1B and C). Each decamer of MIP-1 dimers is ~44 Å wide and 110 Å long (Figure 1C). Both MIP-1 proteins exhibit highly negatively charged convex surfaces; the concave surface of MIP-1 α is mostly neutral, whereas that of MIP-1 β is weakly positively charged (Figure 1D).

Within the MIP-1 polymer, the MIP-1 monomer displays the common structural fold of CC chemokines: a 10 amino acid long N-terminal loop followed by a short 3_{10} helix, a β -sheet composed of three anti-parallel β -strands, and a C-terminal α -helix that packs against the β -sheet (Figure 1E, Supplementary Figure S3). The crystal structures of MIP-1 monomer overlap well with the available NMR structures of wild-type MIP-1 β and MIP-1 α D27A mutant (Figure 1E) (Lodi *et al*, 1994; Czaplewski *et al*, 1999). RMSD values range from 1.6 to 2.0 and 1.0 to 1.1 Å for MIP-1 α and MIP-1 β , respectively, whereas the corresponding RMSD values within the NMR structures range from 1.1 to 1.5 and 0.1 to 0.3 Å, respectively. Similar to the NMR structures, the N-terminal loop of two MIP-1 monomers within MIP-1 polymers also comes together to form an antiparallel β -sheet to form an MIP-1 dimer (Figure 1E). However, comparison of MIP-1 dimers in the NMR and crystal structures reveals a noticeable rigid body movement between MIP-1 monomers (Figure 1E). The centre of mass of MIP-1 β monomer shifts 7 Å and undergoes a 27° rotation (relative to the C α atom of threonine 9), whereas MIP-1 α has a smaller translation (5 Å) and rotation (7°). This movement renders the dimer of MIP-1 α and MIP-1 β inside the MIP-1 polymers to be more compact.

Our MIP-1 polymer structures reveal for the first time the novel interaction between MIP-1 dimers that lead to

Table I Crystallographic statistics of MIP-1 and MIP-1 α -bound IDE

	MIP-1 α	MIP-1 β	MIP-1 α (D27A)	IDE/MIP-1 α
Crystallization condition ^a	Na/KPO ₄ (1.6 M, pH 7)	8% PEG8000 0.1 M Tris pH 7 0.2 M MgCl ₂	0.2 M NH ₄ Ac 0.1 M HEPES (pH 7.8) 26% PEG3350	11.5% PEGMME 5000 0.1 M HEPES pH 7 10% Tacsimate 10% Dioxane
<i>Data collection</i>				
Beam line	APS-19ID	APS-19ID	APS-19ID	APS 14-BMC
Wavelength (Å)	0.9792	0.9792	0.9792	0.9762
Space group	P6222	C222 ₁	P2 ₁ 2 ₁ 2 ₁	P6 ₅
<i>Cell dimension (Å)</i>				
<i>a</i>	182	60	57	263
<i>b</i>	182	88	114	263
<i>c</i>	77	187	174	91
α	90	90	90	90
β	90	90	90	90
γ	120	90	90	120
Resolution (Å)	50–2.65	50–2.6	50–2.18	50–3.0
R_{sym} (%) ^b	8.3 (46.0) ^c	12.1 (49.9)	7.6 (46.4)	14.2 (53.0)
I/σ	40.7 (5.2) ^c	17.6 (3.8)	31.6 (4.8)	16.9 (3.0)
Redundancy ^d	10.6 (11.0) ^c	7.2 (7.2)	4.7 (4.9)	5.0 (5.0)
Completeness (%)	99.9 (100) ^c	100 (100)	99.8 (100.0)	99.6 (100.0)
Unique reflections	22 235	15 529	61 457	67 744
<i>Refinement</i>				
R_{work} ^e	22.3	18.6	21.1	18.2
R_{free}	26.5	26.0	28.5	23.7
<i>No. of atoms</i>				
Protein	2605	2649	9142	15678
Water	13	145	448	133
<i>B-factors</i>				
Protein	52.4	33.3	39.3	50.5
Substrate				73.2
Water	51.8	29.6	39.1	45.5
<i>r.m.s.d.</i>				
Bond lengths (Å)	0.023	0.008	0.008	0.014
Bond angles (deg)	1.946	1.045	1.112	1.588
<i>Ramachandran plot (%)</i>				
Favourable	93.1	92.5	97.3	88.3
Allowed	6.9	7.2	2.7	11.7
Generously allowed	0	0.3	0	0
Disallowed	0	0	0	0
PDE code	2X69	2X61	2X6 g	3H44

^aMIP-1 proteins and IDE/MIP-1 α are crystallized at 2.5 and 5 mg/ml, respectively.^b $R_{\text{merge}} = \Sigma (I - \langle I \rangle) / \Sigma \langle I \rangle$.^cThe outer resolution shell. Values in parentheses indicate the highest resolution shell.^d $N_{\text{obs}}/N_{\text{unique}}$.^e $R_{\text{work}} = \Sigma_{\text{hkl}} |F_{\text{obs}}| - |F_{\text{calc}}| / \Sigma_{\text{hkl}} |F_{\text{obs}}|$.^f R_{free} , calculated the same as for R_{work} , but on 5% data excluded from the refinement calculation.

polymerization. The dimer–dimer interface of MIP-1 proteins has $\sim 1100 \text{ \AA}^2$ buried surface (Supplementary Figure S4). As a monomer, MIP-1 proteins have a dipolar charge distribution (Figure 1F). By formation of the MIP-1 polymer, the positively charged patch of MIP-1 crucial for receptor binding is buried (Figure 1F). The salt bridges between D27/E67 and R46/R48 and the hydrogen bond between D6 and S33 are key contacts between MIP-1 dimers (Figure 1G, Supplementary Figure S4). Consistent with this, D27 and E67 are highly conserved among the chemokines that tend to form high-MW aggregates (MIP-1 and RANTES), and mutation at either of these sites to alanine destabilizes MIP-1 α and MIP-1 β aggregates (Supplementary Figure S5) (Czaplewski *et al*, 1999). Our

structures show that F24, F29 and Y28, which are conserved among MIP-1 α , MIP-1 β and RANTES, also contribute to MIP-1 polymerization by hydrophobic interactions (Figure 1G, Supplementary Figure S5).

Structure of depolymerization mutant MIP-1 α D27A

MIP-1 α has been explored as a potential therapeutic agent (BB-10010) to protect haematopoietic progenitors (Hunter *et al*, 1995; Bernstein *et al*, 1997; Owen-Lynch *et al*, 1998; Hough *et al*, 2003). To avoid the complication of MIP-1 α polymerization and increase its solubility, a mutation of aspartate 27 to alanine is introduced. The MIP-1 D27A mutation has the most dramatic effect in reducing the

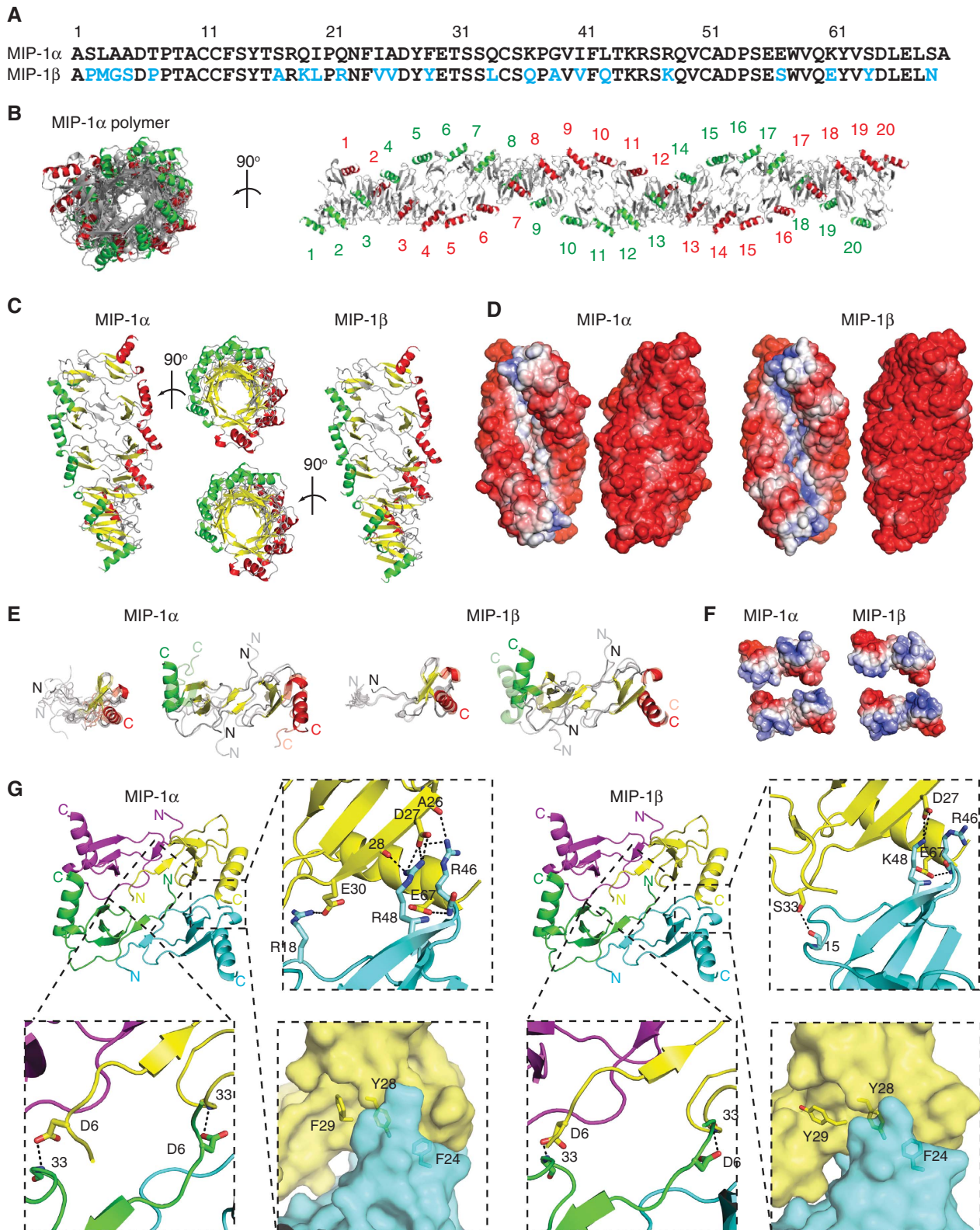


Figure 1 Structure of MIP-1 α and MIP-1 β polymer. **(A)** Sequence alignment of MIP-1 α and MIP-1 β with different residues highlighted in blue. **(B)** Crystal structure of MIP-1 α polymer. A 40mer is depicted to show the periodicity of two 360° turns, and 20 dimers within the 40mer are labelled. The C-terminal helix of each dimer pair is coloured in red and green, respectively. **(C)** Secondary structure and **(D)** surface charge comparison of the MIP-1 α and MIP-1 β decamer. The molecular surface is coloured from negative (red, -6 kT) to positive (blue, -6 kT) as calculated by APBS (38). **(E)** Structural comparison of MIP-1 X-ray structure (solid colour) from this study with NMR structures of MIP-1 α and MIP-1 β (transparent colour). Structure comparison of MIP-1 monomer is on the left and that of dimer is on the right. The PDB code for MIP-1 α and MIP-1 β NMR structures are 1B50 and 1HUN, respectively. **(F)** Charge complementarity between MIP-1 dimers. The molecular surface is coloured as calculated by APBS (< -6 kT in red, 0 kT in white, and > +6 kT in blue). **(G)** Detailed interaction of MIP-1 α at the dimer-dimer interface formed by the interaction of monomers diagonal to each other (top right panel) and between the side-by-side monomers (bottom right panel).

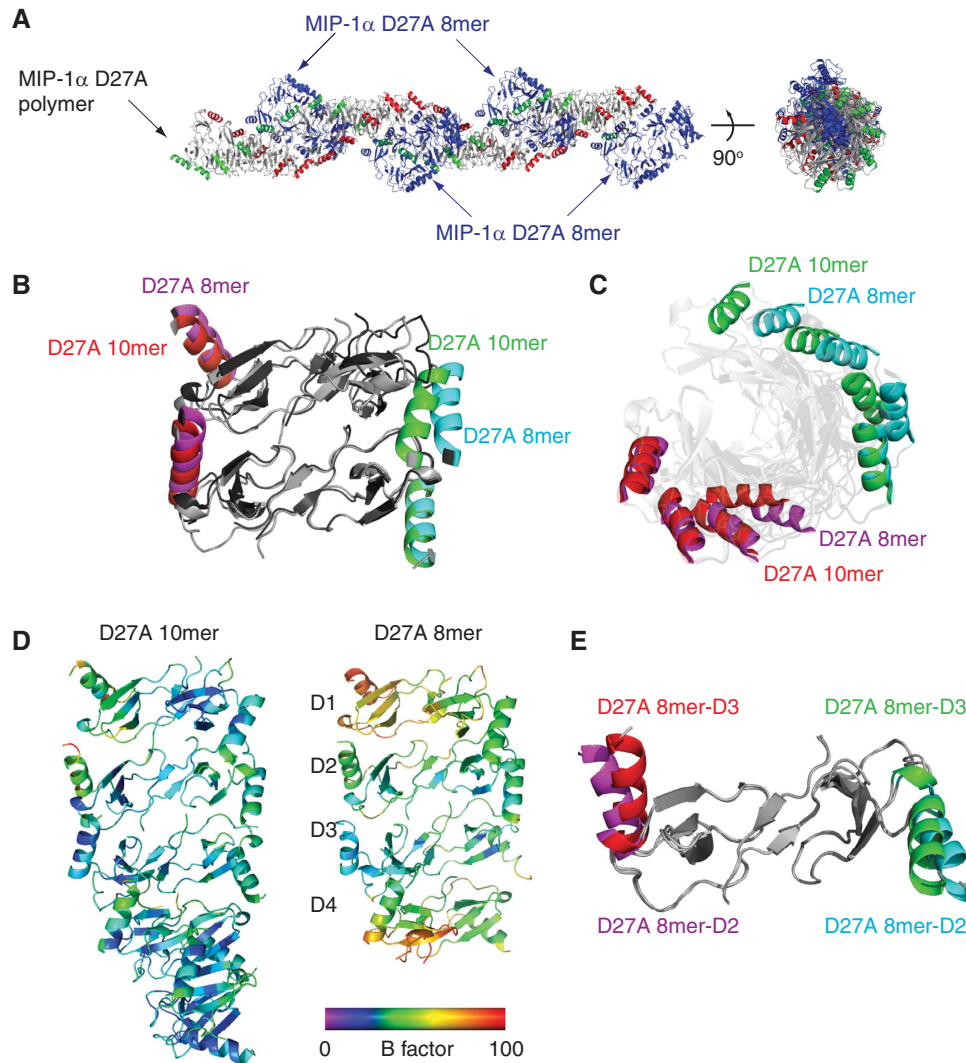


Figure 2 Characterization and structure analysis of MIP-1 α (D27A) polymer. (A) Overall structure of MIP-1 α D27A polymer, which consists of the MIP-1 α D27A polymer (coloured in red and green on their C-terminal α -helices) and MIP-1 α D27A octamer. Comparison of MIP-1 α D27A polymer and octamer either as tetramer (B) or octamer (C), revealing the difference in their degree of rotation. (D) Comparison of MIP-1 α D27A polymer and octamer based on their thermal B factor. (E) Comparison of two dimers within the MIP-1 α D27A octamer, revealing the conformational change in the C-terminal α -helices in one of the four dimers within the MIP-1 α D27A octamer.

aggregation (Czaplewski *et al*, 1999). However, the mechanism by which the D27A mutation hinders MIP-1 α polymerization was unclear. To understand this mechanism, we purified MIP-1 α D27A and, as expected, it is active in an *in vitro* chemotaxis assay (Supplementary Figure S1). We subsequently solved the polymer structure of this mutant at 2.1 Å resolution.

Our MIP-1 α D27A structure reveals two polymer states (Figure 2A). The first state is a MIP-1 α D27A polymer identical to those formed by wild-type MIP-1 α , revealing its full potential to form rod-shaped polymers. Interestingly, the second state is a rod-shaped helical octamer decorating the rod-shaped polymer (Figure 2A). These two states make minimal contact and thus are unlikely to be biologically significant. However, the structure of the MIP-1 α D27A octamer is noticeably different from the MIP-1 α D27A polymer (Figure 2A). Instead of the 36° rotation found in the MIP-1 α D27A polymer, the adjacent dimer within the MIP-1 α D27A octamer has only rotated ~31°, leading to a total of

15° under-rotation of this octamer (Figure 2B and C). The octamer is less ordered, on the basis of the fact that its overall thermal B factor is significantly higher than that of the MIP-1 α D27A polymer, and its terminal monomers have high individual B factors (Figure 2D). In addition, one of the four dimers within the MIP-1 α D27A octamer has a noticeable conformational change in the C-terminal α -helix (Figure 2E). Together, our data suggest that the MIP-1 α D27A octamer represents a less-stable intermediate state of MIP-1 polymer and offers the molecular basis for depolymerization caused by D27A mutation.

MIP-1 proteins form polydisperse, rod-shaped polymers in solution

We then characterized MIP-1 polymers in solution biophysically, particularly, with respect to their size and shape. The SEC data confirmed that both MIP-1 α and MIP-1 β behaved as high-MW polymers as previously reported (Figure 3A). The MW of MIP-1 α and MIP-1 β at 1 mg/ml are approximately

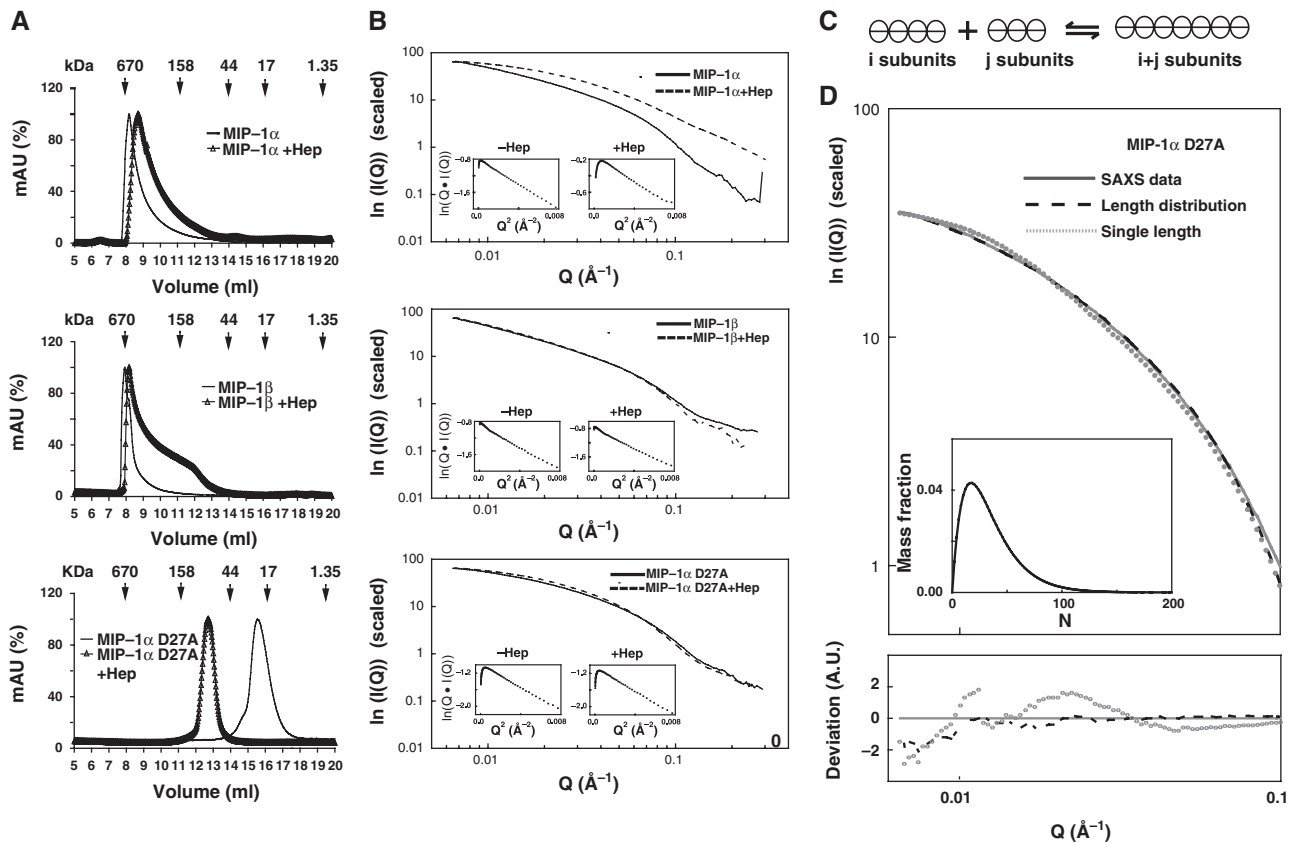


Figure 3 Characterization of MIP-1 α and MIP-1 β polymers in solution. (A) SEC of 1 mg/ml MIP-1 α , MIP-1 β and MIP-1 α D27A with or without 0.1 mg/ml heparin. SEC was performed using phosphate-buffered saline (PBS). (B) Experimental scattering curves for 1 mg/ml MIP-1 α , MIP-1 β and MIP-1 α D27A with or without 0.1 mg/ml heparin in PBS. Insets: cross-section, Guinier rod plots. (C) Schematic representation of our model for the polymerization process. The detailed mathematical modelling is appended in the Supplementary Material. (D) Fitting of the experimental data (solid line) with the calculated scattering from either the best polymer distribution given by our model (dashed line) or the best single polymer (dotted line) with difference between the experimental and fitted theoretical curves shown on bottom. Inset: size distribution of the polymers length distribution. The fitting errors $I_0 \times I_{\text{theo}}^L(q) - I_{\text{exp}}(q) + I_b$ are represented in the deviation curve. Parameter values were chosen to minimize the fit function $\int_0^{q_{\text{max}}} [I_0 \times I_{\text{theo}}^L(q) - I_{\text{exp}}(q) + I_b]^2 dq / q_{\text{max}}$, as described in the Supplementary Material.

400–600 and 600–3000 kDa, respectively. This indicates that MIP-1 can form polymers that contain more than 50 monomers in solution (Supplementary Table S2). We then used SAXS to assess the shape of MIP-1 in solution. If MIP-1 polymers were rod shaped, we would expect to observe linearity of the cross-section, Guinier rod plot over a wide but intermediate range of scattering vectors, q . This is indeed the case (Figure 3B). This is further supported by the asymmetric shape of the distance distribution function ($P(r)$) with a linear slope on the right side (Supplementary Figure S6). Thus, MIP-1 α and MIP-1 β form rod-shaped polymers in the physiological buffer. The radii of the rod-shape particles (49 and 47 Å for MIP-1 α and MIP-1 β , respectively) are close to the width of the MIP-1 polymer structures (44 Å plus a layer of water). Furthermore, the values of the cross-section radius of gyration (R_c) for MIP-1 α and MIP-1 β are nearly identical. Thus, the SAXS data agree with the MIP-1 polymer structures. Consistent with our SEC data, the SAXS data also indicate that MIP-1 β forms polymers with an averaged length greater than MIP-1 α at a given concentration (Supplementary Table S2).

Our data also support the idea that the D27A mutation hinders MIP-1 α polymerization. The SEC data showed that the D27 mutation reduces MIP-1 α aggregation from

400–600 kDa to 50–150 kDa (Figure 3A). Consistent with this, SAXS data indicated that the MIP-1 α D27A mutant yields shorter polymers than the wild-type MIP-1 α (Figure 3B, Supplementary Table S2). In agreement with our MIP-1 α D27A structure, the scattering data indicated that this mutant also forms rod-shaped polymers in solution (Figure 3B, Supplementary Figure S6).

Heparin, a highly sulphated GAG, is frequently used to examine the effect of GAG on the aggregation of chemokines. Our SEC data showed that the addition of heparin increased the elution volume of the MIP-1 peak and broadened the elution profile (Figure 3A). Thus, heparin can trigger a reduction in MIP-1 α and MIP-1 β polymer size and increase their polydispersity. Our SAXS analysis also showed that heparin significantly altered the scattering pattern of MIP-1 α in such a way that MIP-1 α maintained its rod shape but reduced its size from a 40–50mer to a 20–30mer (Figure 3B, Supplementary Table S2). Together, our data indicate that heparin binding leads to MIP-1 depolymerization. Our SEC data showed that heparin increased the averaged size of MIP-1 α D27A larger, which may be due to the molecular mass of heparin and/or the altered polymerization of the MIP-1 α mutant (Figure 3A). However, the addition of heparin did not alter the SAXS pattern for MIP-1 α D27A, suggesting that

heparin does not significantly affect the polymerization of MIP-1 α D27A (Figure 3B, Supplementary Table S2).

To better understand the polymer length distribution, we used a simple equilibrium model for the polymerization process (see Supplementary Mathematical Modeling for details; van Dongen and Ernst, 1984). We propose that the basic unit in the model is the MIP-1 dimer. This is based on the fact that MIP-1 α and MIP-1 β stay dimeric under relatively harsh conditions to reduce the aggregation of MIP-1 in previous NMR studies (Lodi *et al*, 1994; Czaplewski *et al*, 1999). Furthermore, the binding energy calculation using our MIP-1 polymer structures and PISA web-server shows that the dimerization energy of MIP-1 monomers is much higher than the polymerization energy of MIP-1 dimers. In our polymerization model, dimers come together to form polymers, and two polymers of arbitrary sizes can coalesce to form a longer one (Figure 3C). This process is reversible, and therefore a long polymer can break into two smaller polymers. Based on this, we derived analytical expressions for the concentrations of polymers of all sizes as a function of only two parameters: the binding affinity between MIP-1 dimers (which we assume to be independent of the dimer position within the polymer) and MIP-1 concentration (Supplementary Mathematical Modeling). This model implies that the average MIP-1 polymer size is concentration dependent and polymers of different sizes coexist. Consistent with these hypotheses, our SEC data show that the average MIP-1 polymer size is concentration dependent and the elution profile of MIP-1 α and MIP-1 β is asymmetric and skewed towards low-MW fractions (Figure 3A, Supplementary Figure S7).

To further examine the polydispersity of MIP-1 proteins in solution, we then fit our experimental scattering data with the theoretical scattering intensity expected for either a monodisperse or polydisperse polymer solution. We found that polydisperse polymer populations expected from our reversible polymerization model fit our experimental data for MIP-1 α D27A significantly better than any unique poly-

mer size (Figure 3D). In addition, our polymer model offered a fit of comparable quality with that obtained for a single polymer size for the SAXS data of wild-type MIP-1 α and MIP-1 β (Supplementary Figure S8). Thus, our data together support the formation of reversible rod-shaped MIP-1 polymers in solution.

Effect of depolymerization mutations on the biological functions of MIP-1 α

Our structures reveal that polymerization would bury the CCR binding site of MIP-1. Thus, MIP-1 polymers should have a reduced potency in MIP-1-mediated responses and the depolymerization mutations could render MIP-1 more effective. To test this hypothesis, we examined the ability of MIP-1 to arrest human peripheral blood mononuclear cells (PBMCs) onto the human umbilical vein endothelial cell (HUVEC) monolayers that were activated by tumour necrosis factor- α (TNF- α) under flow conditions. We show that while the moderate ability of wild-type MIP-1 α (WT) to recruit PBMC is almost indistinguishable from the buffer control, the treatment with MIP-1 α D27A induces a three-fold increase in PBMC arrest onto the activated HUVEC monolayers (Figure 4A).

To further assess the function of MIP-1 α polymerization, we sought to analyse an additional depolymerization mutant. The mutation of proline 8 to alanine restricts MIP-1 β to its monomeric form and causes MIP-1 β to be ineffective in peritoneal cell recruitment (Laurence *et al*, 2000; Proudfoot *et al*, 2003). On the basis of our MIP-1 structures, proline 8 is not involved in the dimerization or polymerization directly, but its impact on the structure could affect assembly indirectly. We thus predicted and confirmed that the P8A mutation decreases MIP-1 α polymerization relative to wild-type MIP-1 α at various protein concentrations (Supplementary Figure S7). Accordingly, we show that the treatment of MIP-1 α P8A mutant also leads to an elevated arrest of PBMC onto the activated HUVEC monolayers (Figure 4A).

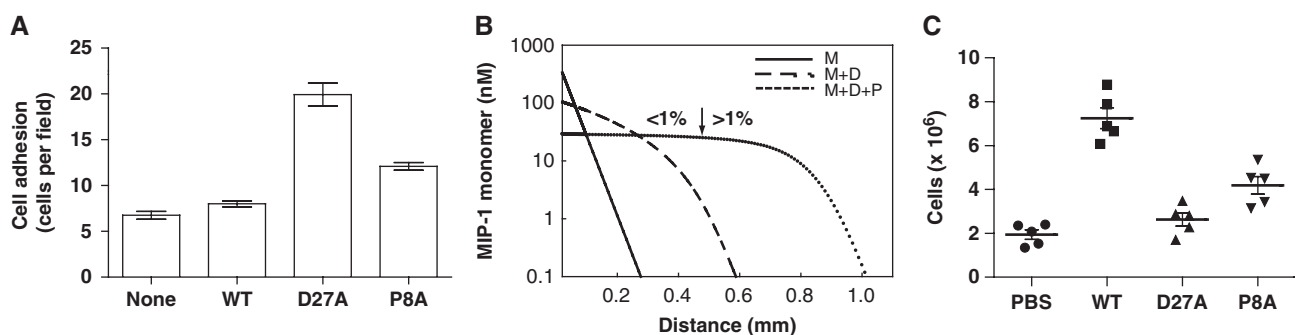


Figure 4 Effects of MIP-1 depolymerization mutations on biological functions of MIP-1. (A) Arrest of PBMCs onto TNF α -activated HUVECs under flow conditions after preincubation without or with MIP-1 α WT or D27A or P8A (1 μ g/ml). The *P*-values for MIP-1 α WT versus D27A or P8A are <0.02 . (B) Theoretical model for the MIP-1 monomer profile away from its secretion site in the presence of diffusion and degradation by IDE. Three curves are plotted, corresponding to three different set of chemical reactions: degradation only (solid line; M (monomer only)); degradation and dimerization (dashed line; M + D); degradation, dimerization and polymerization of the dimer (dotted line; M + D + P). The arrow marks the cutoff point, where the concentration drop across the cell is larger than 1% on the M + D + P gradient so that effective chemotaxis occurs far away from the source of MIP-1 (where it is steep), but not in its vicinity (where it plateaus). The parameters of the model are chosen as follows: diffusion constant: 1 μ m²/s; degradation rate: 10⁻³/s; MIP-1 secretion rate at the secretion site: 2 \times 10⁻¹¹ mol/m²/s; dimerization rate: 10⁶/M/s; dimer disassembly rate: 10⁻²/s; dimer-dimer binding rate: 10⁵/M/s; dimer-dimer unbinding rate: 10⁻²/s. The details in this mathematical modelling are appended in the Supplementary Material. (C) Peritoneal cell accumulations in response to wild-type MIP-1 α , MIP-1 α D27A or MIP-1 α P8A. Male C57BL/6 mice were intraperitoneally injected with 10 μ g of either MIP-1 α WT or D27A or P8A mutant for 20 h. Cells accumulated in the peritoneal cavity were collected and counted. Values shown are means \pm s.e.m. of measurements using five mice per group. The *P*-values for the comparison of MIP-1 α WT with PBS and MIP-1 α D27A mutant are <0.0001 and that with MIP-1 α WT and P8A mutant is 0.0012.

The reversible equilibrium of MIP-1 monomer with MIP-1 dimer and polymers would make MIP-1 a more effective chemoattractant over a longer range, if proteases that selectively degrade MIP-1 monomer but not MIP-1 dimer or polymer exist (Figure 4B; see Supplementary Mathematical Modeling for details). Our mathematical modelling predicts that the MIP-1 monomer concentration would decay exponentially if MIP-1 exists only as monomers. By allowing MIP-1 to dimerize, a fraction of the MIP-1 is protected from degradation, which results in a shallower gradient with a longer chemoattraction range. These effects would be more pronounced when taking into account both the dimerization and polymerization of MIP-1 (Figure 4B). Thus dimerization and polymerization would extend the effective range of the chemotactic gradient of MIP-1.

This model predicts that the depolymerization mutation would reduce the effective range for cell recruitment *in vivo* by MIP-1. To test this, we examined the ability of MIP-1 α D27A to recruit cells into mouse peritoneum. Intra-peritoneal injection of wild-type MIP-1 α significantly increased cell infiltration into mouse peritoneum by three- to four-fold over baseline (PBS control) (Figure 4C). However, MIP-1 α D27A failed to elicit such a response despite its normal *in vitro* chemotactic activity (Figure 4C, Supplementary Figure S1). We then show that MIP-1 α P8A mutant also has reduced potency for *in vivo* cell recruitment into mouse peritoneum (Figure 4C), despite its activity in an *in vitro* chemotaxis assay (Supplementary Figure S1). Together, our studies using two independent depolymerization mutations in MIP-1 α demonstrate that polymerization is crucial for the biological activities of MIP-1 α .

Identification of monomeric MIP-1 α and MIP-1 β as novel substrates of IDE

In searching for the candidate protease that selectively degrades MIP-1 monomer, we turned our attention to IDE. The size, charge distribution and the location of the N-termini of MIP-1 α and MIP-1 β monomer make them putative substrates for IDE (Malito *et al*, 2008; Manolopoulou *et al*, 2009; Guo *et al*, 2010). Our MIP1 structures reveal that MIP-1 α and MIP-1 β monomers have a volume of $\sim 14\,000\text{ \AA}^3$, which fits comfortably inside the catalytic chamber of IDE (Figure 5A). Both MIP-1 molecules possess dipolar charge distributions that complement well the charge distribution in the inner surface of the IDE catalytic chamber (Figure 5A). Upon proper alignment of electrostatic interactions between MIP-1 and the IDE catalytic chamber, the N-terminal end of MIP-1 can be readily inserted into the exosite of IDE, a key feature of high-affinity binding exhibited by IDE substrates (Malito *et al*, 2008; Guo *et al*, 2010). Whereas the closely related chemokine RANTES has a mostly positively charged surface, which would be repelled from the IDE-C catalytic chamber (Figure 5A). Thus, we predict that MIP-1 α and MIP-1 β monomers are high-affinity substrates for IDE, whereas RANTES monomer is not.

MALDI-TOF mass spectrometry (MS) analyses indicate that IDE indeed can cleave both MIP-1 α and MIP-1 β . MIP-1 α fragments were readily observed after a 30-second incubation of MIP-1 α with IDE in a 50:1 molar ratio. The cleavage rate is estimated to be ~ 0.7 per second. IDE can degrade MIP-1 α D27A faster (~ 5 per second), comparable with the cleavage rate of insulin by IDE (Manolopoulou *et al*, 2009).

This is consistent with the notion that IDE can only degrade MIP-1 α monomers, as the D27A mutation induces MIP-1 α depolymerization. We found that heparin modestly accelerated the degradation of MIP-1 α by IDE to ~ 1 per second, which correlates well with the effect of heparin in depolymerizing MIP-1 α . IDE could also degrade MIP-1 β , and the addition of heparin increased the cleavage rate (from 0.4 to 3 per minute) (Figure 5B). However, we did not observe any appreciable degradation of RANTES by IDE (Figure 5B).

We then examined whether IDE could also selectively degrade MIP-1 in mouse microglia BV-2 cells, which are known to secrete IDE and various chemokines (Ralat *et al*, 2009). We used short hairpin RNA (shRNA) delivered by lentivirus to selectively knockdown IDE expression (Figure 5C). We then examined the secretion of MIP-1 and RANTES from these cells by ELISA under basal- and lipopolysaccharide (LPS)-stimulated conditions (Figure 5D). We found elevated levels of MIP-1 α and MIP-1 β under both basal- and LPS-stimulated conditions in the IDE knockdown BV-2 cells as compared with BV-2 cells infected with control lentivirus. Interestingly, the RANTES level was decreased in IDE knockdown cells, suggesting a possible compensatory mechanism for RANTES clearance. These data suggest that IDE is involved in the clearance of MIP-1 α and MIP-1 β , but not in RANTES.

Analysis of the cleavage sites of MIP-1 α by IDE and functional consequences

We then focused on the degradation of MIP-1 α by IDE, as IDE exhibits much faster cleavage of MIP-1 α than MIP-1 β . We first assessed the ability of MIP-1 α to compete with the degradation of the fluorogenic bradykinin-mimetic peptide, Substrate V by recombinant human IDE (Figure 6A). The IC_{50} value of MIP-1 α is $\sim 170\text{ nM}$, comparable with other high-affinity substrates such as insulin (Manolopoulou *et al*, 2009). We also examined whether cleavage by IDE could affect the biological activities of MIP-1. We first studied the *in vitro* chemotactic activity of intact and IDE-digested MIP-1 α proteins on THP-1 cells, a human acute monocytic leukaemia cell line in a modified Boyden chamber assay. As expected, we observed a typical bell-shaped dose-response curve for intact MIP-1 α with a peak effective concentration at 1 nM (Figure 6B). The treatment of MIP-1 by IDE led to a reduction or loss of chemotactic activity (Figure 6B).

We then investigated whether IDE also affects the MIP-1 α -mediated increase of intracellular calcium in THP-1 cells. As expected, we observed a dose-dependent increase of $[Ca^{2+}]_i$ by MIP-1 α and that 1 and 10 nM MIP-1 α could elicit ~ 50 and 100% responses, respectively (Figure 5C, Supplementary Figure S9A). The treatment of MIP-1 α with IDE at a molar ratio of 10:1 caused a modest decrease in $[Ca^{2+}]_i$ change (Figure 6C). Thus, our data indicated that IDE cleavage could both inactivate MIP-1 α -mediated chemotaxis and modulate MIP-1 signalling. It is worth noting that the treatment of MIP-1 α by the lower level of IDE (50:1, MIP-1 to IDE ratio) resulted in noticeable cleavage of MIP-1 α and reduced the chemotactic activity, but did not significantly reduce the potency of MIP-1 to raise $[Ca^{2+}]_i$ (Figure 6B and C, Supplementary Figure S9B). Thus, the cleavage of MIP-1 α by IDE is less effective at reducing the change of $[Ca^{2+}]_i$ than chemotaxis (Figure 6B and C). It is conceivable that IDE-cleaved MIP-1 α products that are held together by

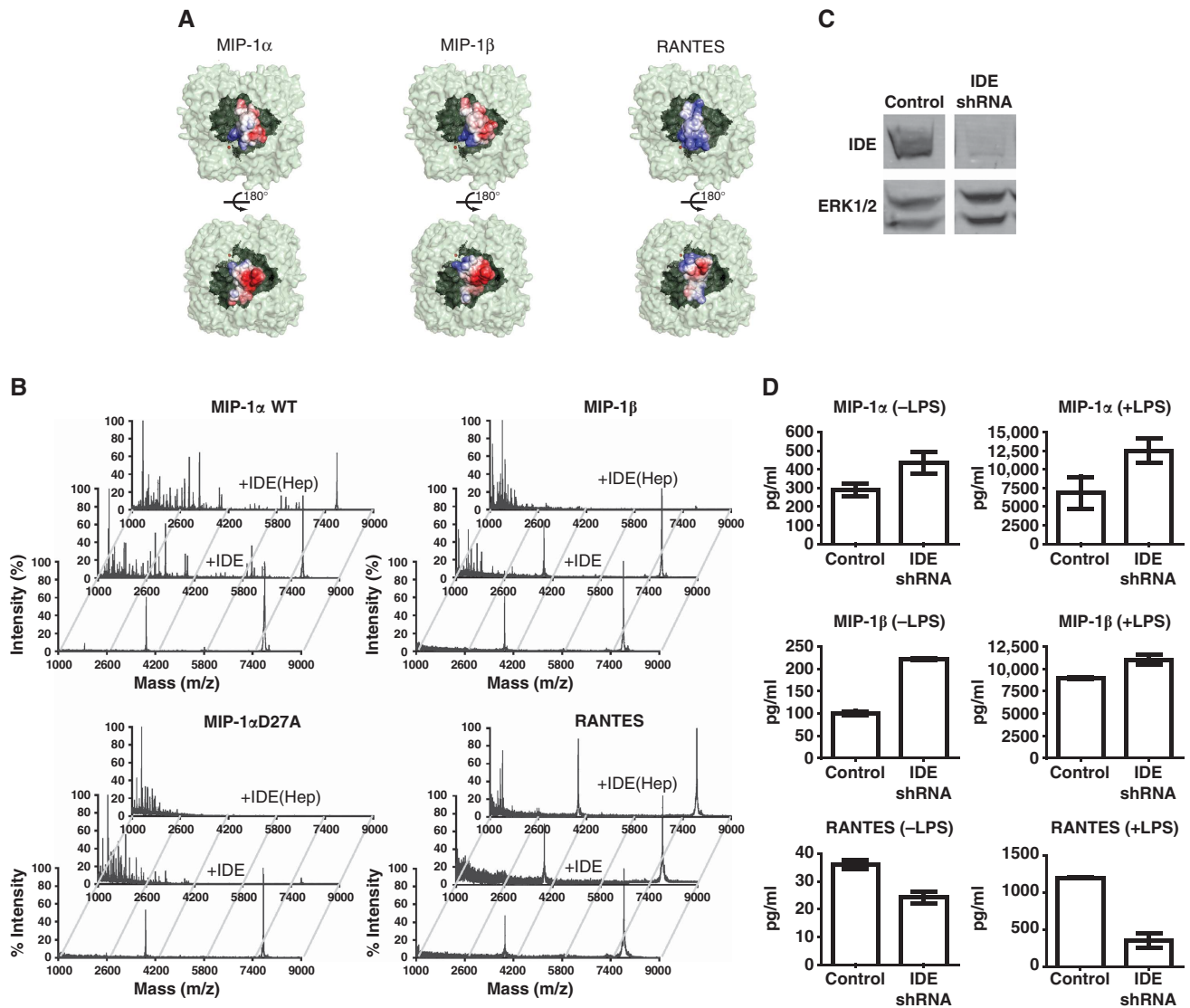


Figure 5 Identification of MIP-1 α as a high-affinity substrate for IDE. (A) MIP-1 α /MIP-1 β /RANTES are modelled into the catalytic chamber of IDE. IDE is depicted as light green and the chamber as dark green. Molecular surface of MIP-1 α /MIP-1 β /RANTES is coloured from negative (red, -6 kT) to positive (blue, $+6$ kT) as calculated by APBS (38). (B) Representative MS spectra of MIP-1 α WT (top), D27A and MIP-1 β (middle), RANTES (bottom) with and without IDE. MIP-1 α WT and D27A proteins ($8 \mu\text{M}$) alone or digested by IDE ($0.16 \mu\text{M}$) with or without the presence of heparin at 37°C for 30 s were analysed by MALDI-TOF MS. MIP-1 β and RANTES samples were treated similarly at 37°C for 15 min. (C) IDE expression of BV-2 stable lines encoding shRNA against mouse IDE. The total cell lysates of BV-2 cells that expressed the control shRNA or IDE shRNA were immunoblotted with anti-IDE (top panel) and anti-ERK1/2 (bottom panel). (D) The secretion of MIP-1 and RANTES by BV-2 cells that have reduced IDE expression. Secreted MIP-1 chemokine levels from IDE knockdown BV-2 cells with or without 10 ng/ml LPS stimulation for 3 h were determined by ELISA assays.

disulphide bonds are still able to partially activate CCR receptors for the transient increase of $[\text{Ca}^{2+}]_i$, but lose their potency in chemotaxis, which occurs on a much longer time scale.

To identify the cleavage sites of MIP-1 α by IDE, we took advantage of the high mass accuracy and high resolution of Fourier-transform ion cyclotron resonance (FTICR) MS-MS analysis to characterize the IDE cleavage sites. MIP-1 α contains two disulphide bonds (Figure 6D). IDE degrades MIP-1 α without the reduction of its disulphide bonds. The addition of a reducing agent after the completion of IDE digestion revealed more than 10 major peaks in the MS spectrum (Figure 6E). A total of 20 fragments were identified, with excellent matches to the calculated mass (Supplementary Tables S3 and S4). From the IDE-digested MIP-1 α fragments,

eight could be generated from the stochastic, single cleavage of MIP-1 α at residues between 18–19, 45–46, 46–47 and 48–49. They include the paired MIP-1 α segments: 1–18 and 19–70, 1–45 and 46–70, 1–46 and 47–70, 1–48 and 49–70 (Figure 6E). These cleavage sites were further confirmed by the proteolytic ^{18}O -labelling during IDE digestion (Supplementary Figure S10). Thus, our data indicate that these four sites are the preferred initial cleavage sites of MIP-1 α by IDE.

Structure analysis of MIP-1 α -bound IDE

To elucidate the molecular basis of MIP-1 α recognition by IDE, the crystal structure of catalytically inactive IDE in complex with MIP-1 α was solved at 3.0 \AA resolution (Table I, Supplementary Figure S2). The overall fold of IDE

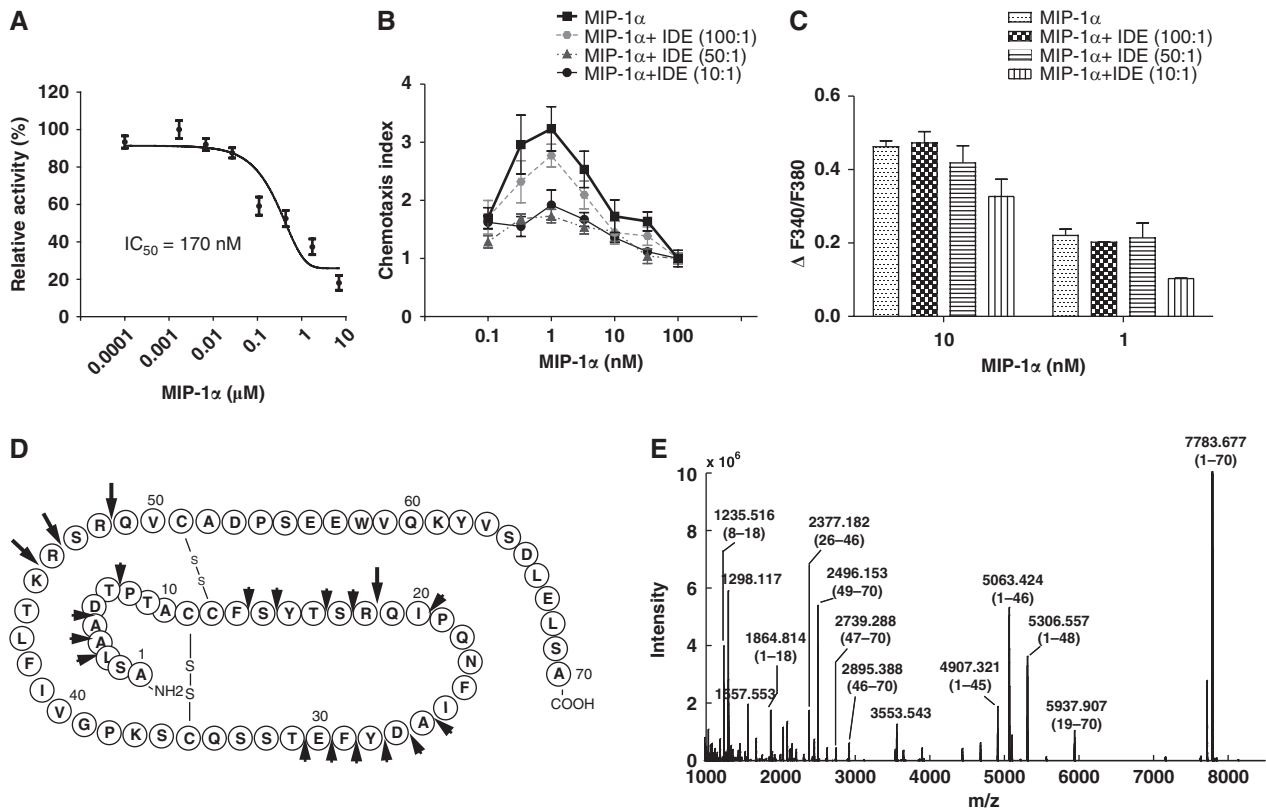


Figure 6 Functional analyses on the effect of MIP-1 degradation by IDE. (A) Inhibition of IDE-mediated degradation of substrate V by MIP-1 α . IDE activity on substrate V was measured at 37°C in the presence of indicated concentrations of MIP-1 α . (B, C) Effects of IDE on the chemotaxis and increase of $[Ca^{2+}]_i$ of MIP-1 α on THP-1 Cells. MIP-1 α was preincubated with IDE at the indicated molar ratio at 37°C for 15 min. For the chemotactic activity (B), chemotactic response was expressed as mean chemotaxis index. For the MIP-1-mediated increase of $[Ca^{2+}]_i$ (C), fura-2 loaded THP-1 cells were stimulated with either 1 or 10 nM MIP-1 α as the positive control or the same concentrations of MIP-1 α that were pretreated with IDE (MIP-1 α + IDE). MIP-1 α -dependent increases of $[Ca^{2+}]_i$ were monitored by ratio of fluorescence at 340 over 380 nm. The change of $[Ca^{2+}]_i$ is indicated by $\Delta F340/F380$, which is the difference between the peak F340/F380 value after addition of MIP-1 α and the basal level before stimulation. (D) Summary of IDE cleavage sites on the MIP-1 α primary sequence by mass spectrometry analysis is illustrated. Initial cleavage sites and secondary cutting sites are shown as big and small arrows, respectively. (E) Representative ESI-FTICR-MS spectrum of MIP-1 α after a 2-min IDE digestion.

is nearly identical to structures of IDE in complex with other known substrates (Figure 7A). Two discrete electron densities representing segments of MIP-1 α are clearly visible inside the catalytic chamber of IDE; one is at the exosite and the other one is at the catalytic site (Figure 7A and B). At the catalytic site of IDE, residues 45–50 of MIP-1 α and a zinc ion coordinated by H108, H112 and E189 of IDE are clearly visible (Figure 7B, Supplementary Figure S4). E111, a catalytic acid known to deprotonate the catalytic water, was mutated to glutamine for catalytic inactivation. This catalytic residue is close to the scissile bond between residues R48 and Q49 of MIP-1 α , one of the four initial cleavage sites identified by our MS analysis. At the exosite, the continuous density could be modelled well with the four N-terminal residues of MIP-1 α ; which resembles the previously observed binding of exosite with the N terminus of IDE substrates (Shen *et al*, 2006; Manolopoulou *et al*, 2009; Guo *et al*, 2010). In this case, the N-terminal loop of MIP-1 α forms a β -strand and inserts into the existing β -sheet of IDE, parallel to the β 12 strand. Residues L359, G361 and Q363 in strand β 12 form hydrogen bonds with N-terminal residues of MIP-1 α . Residue E341 from IDE is also in close vicinity and can form a hydrogen bond with the amino terminus of MIP-1 α . The remaining regions of MIP-1 α are not visible and are likely disordered as we did find

intact MIP-1 α by MS in the MIP-1 α -bound IDE crystal (data not shown).

To bind the catalytic chamber of IDE, both segments of MIP-1 α in the IDE-bound MIP-1 α structure must undergo a substantial conformational change upon their interaction with IDE (Figure 7C). The N-terminal segment of MIP-1 α alters its orientation in order to bind the exosite. The loop region of residues 45–50 also forms a β -strand that fits into the catalytic cleft of IDE. Compared with other substrate-bound IDE structures, we propose that IDE also uses the open-closed conformational switch to entrap and unfold MIP-1 α for its degradation (Supplementary Figure S11) (Shen *et al*, 2006; Manolopoulou *et al*, 2009; Guo *et al*, 2010).

Our MIP-1 α -bound IDE structure offers a molecular basis for the selective cleavage of MIP-1 α by IDE at the defined sites, leading to MIP-1 inactivation. The four IDE cleavage sites (between residues 18–19, 45–46, 46–47 and 48–49) reside at the two structurally adjacent loops and they overlap with residues that are indispensable for the biological functions of MIP-1 α (Figure 7D). When residues R18, Q19, K45, R46 and R48 were mutated into alanines, MIP-1 α -binding affinity to its cognate receptor CCR5 was greatly attenuated (Teng *et al*, 2008). Interestingly, residues of MIP-1 α crucial for receptor binding all map to the same side of the

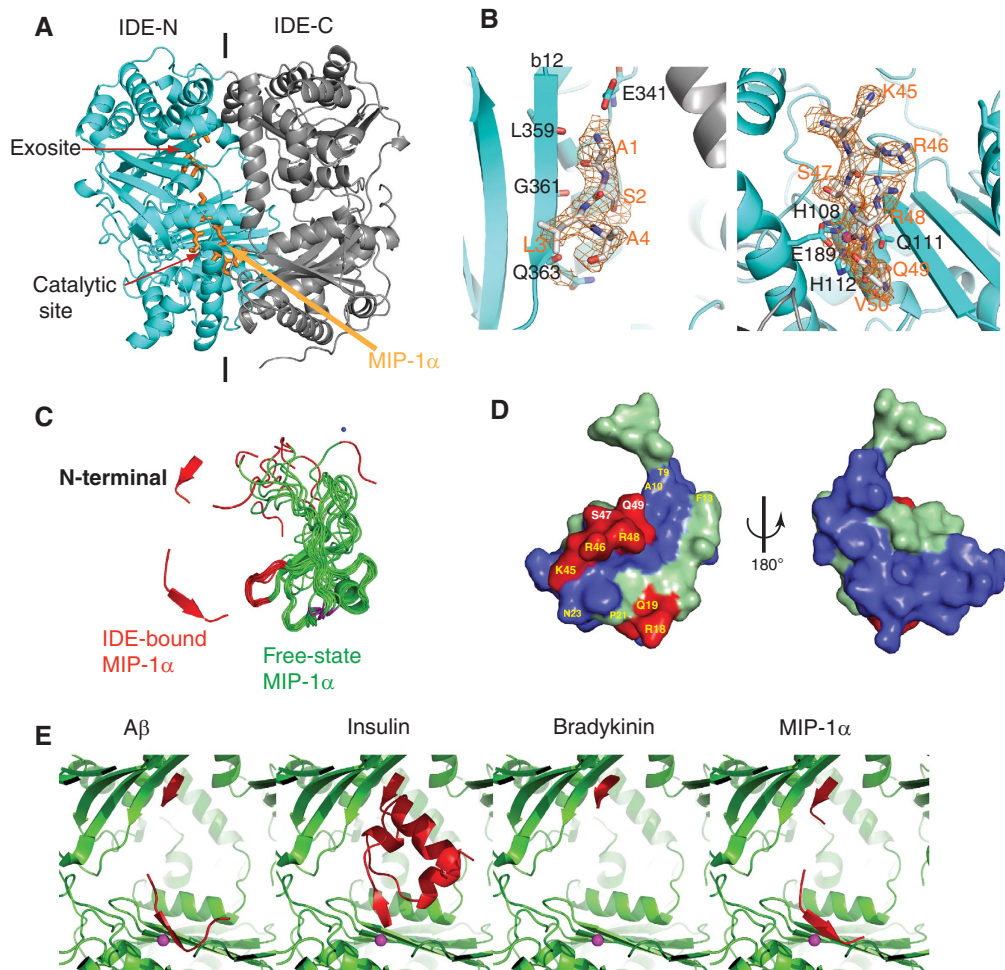


Figure 7 Structural analyses on MIP-1 α -bound IDE. (A) Overall secondary structure of IDE-CF-E111Q in complex with MIP-1 α . N- and C-terminal domains of IDE are coloured cyan and grey, respectively. MIP-1 α is coloured orange. (B) The detailed interaction of MIP-1 α at the exosite (left) and catalytic site (right). Composite omit map was coloured orange at 1 σ level; the atoms oxygen, nitrogen and carbon of substrates are shown in red, blue and orange, respectively. (C) Comparison of MIP-1 α in the free form (1B50, green) with IDE-bound form (3H44, red). The corresponding regions of MIP-1 α found in IDE-bound form are coloured as red. (D) The three-dimensional structure of MIP-1 α (2X69). The residues for IDE initial cleavage sites and secondary sites are coloured red and light green, respectively. Residues involved in receptor CCR5 binding are highlighted yellow. (E) Structural comparison of IDE in complex with A β (2G47), insulin (2WBY), bradykinin (3CWW) and MIP-1 α (3H44). IDE and its substrates are coloured green and red, respectively.

molecule, where four IDE initial cleavage sites reside (Figure 7D). Thus, IDE can specifically target functional residues of MIP-1 α and cleavage of MIP-1 α at any one of these four sites by IDE would likely perturb the local structure to prevent MIP-1 α from activating its receptor.

Structural comparison of MIP-1 α - and insulin-bound IDE structures revealed common and unique features for the interaction of IDE with these two structurally distinct substrates (Figure 7E). Both insulin and MIP-1 α have a dipolar charge distribution. Similar to the interaction of insulin with IDE, the mostly negatively charged surface of MIP-1 α is facing the positively charged IDE-C domain. The interaction with both exosite and IDE-C domain is likely to greatly enhance the binding affinity of MIP-1 α and insulin to IDE. In contrast of insulin, where the initial cleavages are ~ 15 Å away from the catalytic site, our MIP-1 α -bound IDE model places the four initial cleavages of MIP-1 α close to the catalytic site. Thus, instead of the major conformational change required for insulin to be cut by IDE, a relatively small repositioning of two adjacent loops that contain the

four cleavage sites would be needed for IDE to cut any of these four sites in a stochastic manner. Furthermore, based on the NMR structures, MIP-1 α molecules are highly flexible, especially at the N-terminal end (Figure 7C). This flexibility is also likely to contribute to the unfolding and cleavage of MIP-1 α by IDE.

Discussion

Protein polymerization governs diverse biological and pathological events (Frieden, 2007). Our studies simplify the polymerization of MIP-1 from a potentially complex process, such as amyloid fibre formation to a simple dimer-dimer interaction by charge and shape complementarity. Furthermore, our structural and biophysical analyses reveal that MIP-1 forms ordered, rod-shaped helical polymers and explain how the reversible polymerization of these chemokines occurs in solution. Our structural and biophysical analyses also offer the molecular basis of MIP-1 polymerization and how the D27A mutation affects MIP-1 α polymerization.

Using two depolymerization mutants (D27A and P8A), we also demonstrate vital roles of polymerization for two MIP-1 α -mediated functions. We show that while depolymerization mutations allow MIP-1 α to enhance the arrest of monocytes onto activated human endothelial monolayer, the same mutations render MIP-1 α ineffective in recruiting cells into mouse peritoneum. Various chemokines have different degrees of oligomerization (Handel *et al*, 2005). Together with previous studies of other CC chemokines, our data clearly show that the ordered and reversible self-assembly of chemokines has key roles in their biological functions (Baltus *et al*, 2003; Proudfoot *et al*, 2003; Handel *et al*, 2008).

GAG is known to bind and regulate the functions of various chemokines (Handel *et al*, 2005; Bishop *et al*, 2007). We found that the addition of heparin (an exemplary GAG) leads to depolymerization of MIP-1. The positively charged residues (R18, K45 and R46) residing at the dimer–dimer interface of MIP-1 polymers are critical for GAG binding (Koopmann *et al*, 1999; Proudfoot *et al*, 2003; Handel *et al*, 2005). Thus, the binding of heparin could reduce the degree of MIP-1 polymerization by capping the end of MIP-1 polymer or affecting the equilibrium of MIP-1 polymerization. However, the effect of GAG binding in MIP-1 polymerization *in vivo* is likely far more complicated. In different tissues, the heparan sulphate GAG chains are highly diverse in structure and their linked protein partners also vary. In addition to depolymerization, GAG could facilitate MIP-1 polymer formation by anchoring and clustering MIP-1 polymers together on the cell surface or extracellular matrix as well. The effects of GAGs on reversible MIP-1 polymerization *in vivo* and MIP-1-mediated biological functions await future investigation.

MIP-1 polymerization shares interesting similarities with the formation of actin filaments. Actin polymerization also requires minimal conformational change and results in rod-shaped, double-helical filaments (Dominguez, 2009; Kueh and Mitchison, 2009). In addition, diverse cellular components are involved in regulating the polymerization of both proteins (Disanza *et al*, 2005). GAGs and proteoglycans on cell surfaces or extracellular matrix could cap the end of MIP-1 polymers to regulate MIP-1 polymerization. The reversible binding of GAGs and proteoglycans to the end of MIP-1 polymers would immobilize MIP-1 and render cell recruitment from a chemotactic response to haptotaxis. Alternatively, GAGs could also sever MIP-1 polymers to facilitate the distribution of MIP-1 polymers for their biological functions. Similarly, a plethora of actin-binding proteins modulate the formation and distribution of actin filaments (Disanza *et al*, 2005). Capping proteins can block the elongation of actin polymerization. Through its severing activity, cofilin could increase the free barbed end of actin polymer for actin-based protrusion. Furthermore, multiple structural states exist in actin filament (Kueh and Mitchison, 2009). The less stable polymer state found in the MIP-1 α D27A octamer structure highlights the potential complexity in conformational states of chemokine polymers.

Our structural analyses of the wild-type and mutant forms of MIP-1 reveal that CC chemokine polymerization may be more common than previously anticipated. For example, RANTES shares 44% sequence identity with MIP-1 α and is also known to form large aggregates (Supplementary Figure S5). Although the isoelectric point (pI) for RANTES is 9.2, whereas that of MIP-1 α is 4.8, RANTES preserves the charged

residues (D27, E67, R46 and R48) vital for polymer formation (Supplementary Figure S5). As expected, our preliminary SAXS analysis suggests that RANTES indeed forms rod-shaped polymers (data not shown). The sequence alignment of 27 CC chemokines reveals that those charged residues crucial for the polymerization of MIP-1 α and MIP-1 β are not absolutely conserved. We found that D27A mutation reduces but does not abolish MIP-1 α polymerization. Thus, a chemokine missing one of these key contact sites, such as CCL8, may still be capable of forming polymers. The corresponding residues for D27 and E67 in CCL14 are serine and lysine, respectively (Supplementary Figure S5). This may explain why the packing of the CCL14 tetramer structure is distinct from that in the MIP-1 polymers (Supplementary Figure S3).

In the presence of IDE or other monomer-selective proteases, the reversible oligomerization (dimerization and polymerization) of MIP-1 offers two unique features in their chemotactic gradient. First, the oligomerization protects MIP-1 from proteolytic degradation, so that they have longer effective range for recruitment of macrophages and neutrophils. Second, the oligomerization enables the MIP-1 gradient to reflect the severity of infection or inflammation. In a mild infection, when little MIP-1 is made and MIP-1 dimer rarely forms, an exponentially decaying MIP-1 spatial gradient is likely to form in the steady state (similar to the purely monomeric case shown in Figure 4B). Such a gradient is steep so that the cells are targeted to the centre of the infection. However, in a moderate-to-severe infection, MIP-1 production is high, which favours the formation of MIP-1 dimers and polymers. In addition to the benefit of having a longer effective range, our model predicts that the MIP-1 gradient near the centre of secretion is less effective for directional chemoattraction (Figure 4B). Thus, cells are expected to move mostly to the periphery of the infection site, rather than to the centre. This would help to prevent the spread of invading pathogens in a severe infection. This intricate regulation of chemotactic gradient by the interplay between chemokine oligomerization and extracellular proteases may be applicable to other chemokines as well. The validity of this hypothesis on the chemotactic gradient of MIP-1 and other chemokines that also form oligomers and are subject to proteolytic degradation awaits future investigation (Allen *et al*, 2007; Wolf *et al*, 2008).

MIP-1 D27A mutant (BB-10010) was tested in clinical trials for reducing chemotherapy-associated myelotoxicity (Bernstein *et al*, 1997; Owen-Lynch *et al*, 1998; Hough *et al*, 2003). The choice of MIP-1 D27A mutant was made to avoid issues related to MIP-1 aggregation (Hunter *et al*, 1995). However, the treatment revealed no significant improvement in protecting haematopoietic stem cells. Our finding of the defective *in vivo* chemotactic function of MIP-1 α D27A may partially explain why BB-10010 did not exhibit the anticipated therapeutic benefit. The structural basis of MIP-1 polymerization and selective degradation of MIP-1 monomer by IDE may help bring better control of MIP-1 in the development of MIP-1-based therapy for several human diseases (Maurer and von Stebut, 2004).

In addition, our findings on how IDE can affect the clearance of MIP-1 in microglia add another layer of complexity to the role of IDE for the progression of AD. Studies in transgenic mice have revealed the role of IDE in A β degradation *in vivo* (Farris *et al*, 2003; Leissring *et al*, 2003).

Furthermore, the IDE gene resides on chromosome 10q, and lymphoblast samples from chromosome 10-linked AD families have reduced IDE activity (Kim *et al*, 2007). Microglia, the resident macrophages of CNS, are recruited to the site of A β deposit and have a key role in A β clearance (El Khoury and Luster, 2008). We show here that reduced IDE levels can lead to an increase in MIP-1 accumulation. Thus, the reduced IDE activity observed in AD patients may affect A β accumulation through the ability of MIP-1 to compete with IDE and/or alter the recruitment of microglia to the A β deposit in the brain. Therefore, our studies open a new avenue of investigation to identify novel IDE substrates and their roles in the progression of AD, diabetes mellitus and other human diseases. Such studies will undoubtedly aid the development of IDE-related therapeutics.

Materials and methods

Cloning, expression and purification of recombinant chemokines and IDE

The synthetic genes that encode the mature forms of human MIP-1 and RANTES with optimization for *E. coli* codon usage were constructed with an enterokinase cutting site (DDDDK) in front of these chemokines. MIP-1 α mutants were generated by site-directed mutagenesis. MIP-1 and RANTES were expressed as thioredoxin and His₆-tag fusion proteins in *E. coli* BL21(DE3) cells. The fusion proteins were purified by Ni-NTA column (Qiagen) followed by a Source-Q column (GE). Recombinant MIP-1 and RANTES were obtained by removing fusion tags with enterokinase and further purified by heparin affinity chromatography. Final products of MIP-1 and RANTES were analysed by MALDI-TOF MS, and its biological activity was assayed on THP-1 cells by chemotaxis assay (Supplementary Figure S1). Human IDE proteins were expressed in *E. coli* as described (Manolopoulou *et al*, 2009).

Structural analysis

The diffracting MIP-1 and MIP-1 α -bound IDE crystals were grown in the distinct crystallization conditions at 18°C by hanging drop, vapour diffusion (Table I). X-ray diffraction data were measured at 100 K on the ID-19 or 14-BMC at the SBC, Argonne National Laboratory and were processed using HKL3000 (Table I). The initial phase was solved by SAD using selenomethionyl MIP-1 α (V3M/L63M) (Supplementary Table S1, Supplementary Figure S2). Native MIP-1 α (WT and D27A) and MIP-1 β structure determinations were performed by molecular replacement using the MIP-1 α (V3M/L63M), as a search model with the program Phaser. MIP-1 α -bound IDE structure was determined by molecular replacement using IDE-E111Q structure (2G47) as a search model. Structural building and refinement were performed by using REFMAC, Phoenix and Coot.

SEC and SAXS analysis of MIP-1

The size distribution of MIP-1 polymers was determined by using a S200 10/300 GL column. SAXS data were collected at the 18-ID (BioCAT) beamline using the Mar 165 CCD detector at room temperature (23°C) using 1.033 Å as the incident X-ray wavelength. All data processing was carried out using Igor Pro (WaveMetrics Inc.) with macros written by the BioCAT staff following standard procedures and further analysed with GNOM (Svergun, 1991).

PBMC recruitment onto the activated HUVEC monolayer

Endothelial cell medium and HUVEC were obtained from Promocell (Heidelberg, Germany). HUVECs were grown to confluency on 35 mm dishes and activated with 10 ng/ml TNF- α for 3 h before the experiment. Human blood was obtained in citrate/dextran by venipuncture from healthy donors, who gave informed consent. PBMCs were isolated by density gradient centrifugation using Ficoll-Paque medium and washed with PBS before suspension in HEPES-buffered Hank's balanced salt solution containing 0.5% human serum albumin (HH buffer) at 500 000 cells/ml. Activated HUVECs were incubated with 1 μ g/ml either MIP-1 α WT or P8A or

D27A or H₂O at 37°C. After 60 min, HUVEC dishes were assembled in a parallel wall flow chamber and PBMCs were perfused at 1.5 dynes/cm². Adherent cells were recorded by video microscopy at \times 100 magnification and quantified in multiple high-power fields.

In vivo cell accumulation assay

Nine-week-old male C57BL/6 mice (Charles River laboratories; $n = 5$) were intraperitoneally injected with 10 μ g of either MIP-1 α WT or D27A mutant or P8A mutant in 200 μ l PBS. After 20 h, mice were killed by CO₂ asphyxiation. Then the peritoneal cavity was washed 3–4 times with a total of 8 ml of ice-cold Ca²⁺/Mg²⁺-free HBSS containing 1 mM EDTA. The cavity lavage was collected and total cells in the lavage were counted. The experiments were conducted using protocols approved by the Institutional Animal Care and Use Committee at the University of Illinois at Chicago.

MIP-1 degradation by IDE

MIP-1 α competition assay and MS analysis of IDE degradation were performed as previously described (Manolopoulou *et al*, 2009). For MALDI/TOF MS or LC-ESI-FTICR MS/MS analysis, enzyme reactions were performed at 37°C and a given chemokine/IDE molar ratio (usually 50:1) with and without 0.8 mg/ml heparin. Reactions were stopped by the addition of an equal volume of stop solution (200 mM EDTA, 0.2% TFA). Samples were further incubated with 10 mM TCEP at room temperature for 30 min to reduce the disulphide bonds before being applied to MS analysis.

shRNA knockdown of IDE in BV-2 cells

IDE expression in BV-2 cells is knockdown by lentivirus-mediated shRNA expression. Plasmids (a set of five) encoding shRNA that could knockdown mouse IDE expression were purchased from Open Biosystem (RMM4534-NM-031156), and lentivirus were produced by co-transfecting shRNA plasmids with pHR8.2AR packaging plasmid and pCMV VSVG envelope plasmid into HEK293T cells. BV-2 stable lines that contain the specific shRNA were obtained by lentivirus infection and selection with 5 μ g/ml puromycin. IDE knockdown levels were tested by western blotting with a polyclonal anti-IDE antibody raised against human IDE and affinity purified using an immobilized IDE column. Secreted chemokine level from IDE knockdown BV-2 cells that have the most profound IDE knockdown were measured by ELISA assays (R&D system).

Chemokine response assays in THP-1 cells

Cell migration of THP-1 was measured in 96-well Multiscreen™ filter plate (Millipore) as described previously (Gouwy *et al*, 2008). For calcium mobilization assay, THP-1 cells were loaded with 2 μ M fura-2 AM (Invitrogen). Fura-2 fluorescence was measured with a FluoroMax-3 fluorometer (HORIBA Jobin Yvon Inc.) at excitation wavelengths of 340 and 380 nm and emission wavelength of 510 nm.

Supplementary data

Supplementary data are available at *The EMBO Journal* Online (<http://www.embojournal.org>).

Acknowledgements

We are grateful to the staff of APS SBC and Biocars for help in data collection. This work was supported by NIH GM81539 to W-J Tang. Use of the Advanced Photon Source was supported by the US Department of Energy, Office of Basic Energy Sciences, under contract no. W-31-109-ENG-38. Use of proteomics service facility was supported by Chicago Biomedical Consortium. We thank Drs Peter V Usatyuk and Viswanathan Natarajan for advice on calcium immobilization assay, Dr Angelo Scanu for advices and cell lines in the chemotaxis assays, Dr Tobin Sosnick for the SAXS analysis, Dr Tracy Handel for her insightful comments and Vasiliios Kalas for his critical reading of the paper.

Conflict of interest

The authors declare that they have no conflict of interest.

References

- Allen SJ, Crown SE, Handel TM (2007) Chemokine: receptor structure, interactions, and antagonism. *Annu Rev Immunol* **25**: 787–820
- Baltus T, Weber KSC, Johnson Z, Proudfoot AEI, Weber C (2003) Oligomerization of RANTES is required for CCR1-mediated arrest but not CCR5-mediated transmigration of leukocytes on inflamed endothelium. *Blood* **102**: 1985–1988
- Bernstein SH, Eaves CJ, Herzig R, Fay J, Lynch J, Phillips GL, Christiansen N, Reece D, Ericson S, Stephan M, Kovalsky M, Hawkins K, Rasmussen H, Devos A, Herzig GP (1997) A randomized phase II study of BB-10010: a variant of human macrophage inflammatory protein-1 α for patients receiving high-dose etoposide and cyclophosphamide for malignant lymphoma and breast cancer. *Br J Haematol* **99**: 888–895
- Bishop JR, Schuksz M, Esko JD (2007) Heparan sulphate proteoglycans fine-tune mammalian physiology. *Nature* **446**: 1030–1037
- Cocchi F, DeVico AL, Garzino-Demo A, Arya SK, Gallo RC, Lusso P (1995) Identification of RANTES, MIP-1 α , and MIP-1 β as the major HIV-suppressive factors produced by CD8⁺ T cells. *Science* **270**: 1811–1815
- Cook DN, Beck MA, Coffman TM, Kirby SL, Sheridan JF, Pragnell IB, Smithies O (1995) Requirement of MIP-1 α for an inflammatory response to viral infection. *Science* **269**: 1583–1585
- Czaplewski LG, McKeating J, Craven CJ, Higgins LD, Appay V, Brown A, Dudgeon T, Howard LA, Meyers T, Owen J, Palan SR, Tan P, Wilson G, Woods NR, Heyworth CM, Lord BI, Brotherton D, Christison R, Craig S, Cribbes S et al (1999) Identification of amino acid residues critical for aggregation of human CC chemokines macrophage inflammatory protein (MIP)-1 α , MIP-1 β , and RANTES. Characterization of active disaggregated chemokine variants. *J Biol Chem* **274**: 16077–16084
- Disanza A, Steffen A, Hertzog M, Frittoli E, Rottner K, Scita G (2005) Actin polymerization machinery: the finish line of signaling networks, the starting point of cellular movement. *Cell Mol Life Sci* **62**: 955–970
- Dominguez R (2009) Actin filament nucleation and elongation factors—structure-function relationships. *Crit Rev Biochem Mol Biol* **44**: 351–366
- Dunlop DJ, Wright EG, Lorimore S, Graham GJ, Holyoake T, Kerr DJ, Wolpe SD, Pragnell IB (1992) Demonstration of stem cell inhibition and myeloprotective effects of SCI/rhMIP1 α *in vivo*. *Blood* **79**: 2221–2225
- El Khoury J, Luster AD (2008) Mechanisms of microglia accumulation in Alzheimer's disease: therapeutic implications. *Trends Pharmacol Sci* **29**: 626–632
- Farris W, Mansourian S, Chang Y, Lindsley L, Eckman EA, Frosch MP, Eckman CB, Tanzi RE, Selkoe DJ, Guenette S (2003) Insulin-degrading enzyme regulates the levels of insulin, amyloid β -protein, and the beta-amyloid precursor protein intracellular domain *in vivo*. *Proc Natl Acad Sci USA* **100**: 4162–4167
- Frieden C (2007) Protein aggregation processes: in search of the mechanism. *Protein Sci* **16**: 2334–2344
- Gouwy M, Struyf S, Noppen S, Schutyser E, Springael JY, Parmentier M, Proost P, Van Damme J (2008) Synergy between coproduced CC and CXC chemokines in monocyte chemotaxis through receptor-mediated events. *Mol Pharmacol* **74**: 485–495
- Graham G, Wright E, Hewick R, Wolpe S, Wilkie N, Donaldson D, Lorimore S, Pragnell I (1990) Identification and characterization of an inhibitor of haemopoietic stem cell proliferation. *Nature* **344**: 442–444
- Graham GJ, MacKenzie J, Lowe S, Tsang ML, Weatherbee JA, Issacson A, Medicherla J, Fang F, Wilkinson PC, Pragnell IB (1994) Aggregation of the chemokine MIP-1 α is a dynamic and reversible phenomenon. Biochemical and biological analyses. *J Biol Chem* **269**: 4974–4978
- Guo Q, Manolopoulou M, Bian Y, Schilling AB, Tang W-J (2010) Molecular basis for the recognition and cleavages of IGF-II, TGF- α , and amylin by human insulin-degrading enzyme. *J Mol Biol* **395**: 430–443
- Handel TM, Johnson Z, Crown SE, Lau EK, Proudfoot AE (2005) Regulation of protein function by glycosaminoglycans—as exemplified by chemokines. *Annu Rev Biochem* **74**: 385–410
- Handel TM, Johnson Z, Rodrigues DH, Dos Santos AC, Cirillo R, Muzio V, Riva S, Mack M, Déruaz M, Borlat F, Vitte P-A, Wells TNC, Teixeira MM, Proudfoot AEI (2008) An engineered monomer of CCL2 has anti-inflammatory properties emphasizing the importance of oligomerization for chemokine activity *in vivo*. *J Leukoc Biol* **84**: 1101–1108
- Horuk R (2009) Chemokine receptor antagonists: overcoming developmental hurdles. *Nat Rev Drug Discov* **8**: 23–33
- Hough RE, Lorigan PC, Poynton C, Newland A, Gupta RK, Foran J, Hancock BW (2003) A phase II protection study of BB-10010 in patients with high grade non-Hodgkin's lymphoma undergoing intensive chemotherapy. *Int J Oncol* **22**: 421–424
- Hunter MG, Bawden L, Brotherton D, Craig S, Cribbes S, Czaplewski LG, Dexter TM, Drummond AH, Gearing AH, Heyworth CM, Lord BI, McCourt M, Varley PG, Wood LM, Edwards RM, Lewis PJ (1995) BB-10010: an active variant of human macrophage inflammatory protein-1 α with improved pharmaceutical properties. *Blood* **86**: 4400–4408
- Kim M, Hersh LB, Leissring MA, Ingelsson M, Matsui T, Farris W, Lu A, Hyman BT, Selkoe DJ, Bertram L, Tanzi RE (2007) Decreased catalytic activity of the insulin-degrading enzyme in chromosome 10-linked Alzheimer disease families. *J Biol Chem* **282**: 7825–7832
- Kobayashi M, Takahashi H, Sanford AP, Herndon DN, Pollard RB, Suzuki F (2002) An increase in the susceptibility of burned patients to infectious complications due to impaired production of macrophage inflammatory protein 1 α . *J Immunol* **169**: 4460–4466
- Koopmann W, Ediriwickrema C, Krangel MS (1999) Structure and function of the glycosaminoglycan binding site of chemokine macrophage-inflammatory protein-1 β . *J Immunol* **163**: 2120–2127
- Kueh HY, Mitchison TJ (2009) Structural plasticity in actin and tubulin polymer dynamics. *Science* **325**: 960–963
- Kuschert GS, Hoogewerf AJ, Proudfoot AE, Chung CW, Cooke RM, Hubbard RE, Wells TN, Sanderson PN (1998) Identification of a glycosaminoglycan binding surface on human interleukin-8. *Biochemistry* **37**: 11193–11201
- Laurence JS, Blanpain C, Burgner JW, Parmentier M, LiWang PJ (2000) CC chemokine MIP-1 β can function as a monomer and depends on Phe13 for receptor binding. *Biochemistry* **39**: 3401–3409
- Leissring MA, Farris W, Chang AY, Walsh DM, Wu X, Sun X, Frosch MP, Selkoe DJ (2003) Enhanced proteolysis of beta-amyloid in APP transgenic mice prevents plaque formation, secondary pathology, and premature death. *Neuron* **40**: 1087–1093
- Lindell DM, Standiford TJ, Mancuso P, Leshen ZJ, Huffnagle GB (2001) Macrophage inflammatory protein 1 α /CCL3 is required for clearance of an acute *Klebsiella pneumoniae* pulmonary infection. *Infect Immun* **69**: 6364–6369
- Lodi PJ, Garrett DS, Kuszewski J, Tsang ML, Weatherbee JA, Leonard WJ, Gronenborn AM, Clore GM (1994) High-resolution solution structure of the beta chemokine hMIP-1 β by multidimensional NMR. *Science* **263**: 1762–1767
- Lortat-Jacob H, Grosdidier A, Imbert A (2002) Structural diversity of heparan sulfate binding domains in chemokines. *Proc Natl Acad Sci USA* **99**: 1229–1234
- Malito E, Ralat LA, Manolopoulou M, Tsay JL, Wadlington NL, Tang W-J (2008) Molecular bases for the recognition of the short peptide substrate and cysteine-directed modifications of human insulin-degrading enzyme. *Biochemistry* **47**: 12822–12834
- Manolopoulou M, Guo Q, Malito E, Schilling AB, Tang WJ (2009) Molecular basis of catalytic chamber-assisted unfolding and cleavage of human insulin by human insulin-degrading enzyme. *J Biol Chem* **284**: 14177–14188
- Maurer M, von Stebut E (2004) Macrophage inflammatory protein-1. *Int J Biochem Cell Biol* **36**: 1882–1886
- Menten P, Wuyts A, Van Damme J (2002) Macrophage inflammatory protein-1. *Cytokine Growth Factor Rev* **13**: 455–481
- Owen-Lynch P, Czaplewski L, Hunter M, Whetton A (1998) The growth inhibitory role and potential clinical value of macrophage inflammatory protein 1 α in myeloid leukaemias. *Leukemia Lymphoma* **30**: 41–53
- Proost P, Menten P, Struyf S, Schutyser E, De Meester I, Van Damme J (2000) Cleavage by CD26/dipeptidyl peptidase IV converts the chemokine LD78 β into a most efficient monocyte attractant and CCR1 agonist. *Blood* **96**: 1674–1680
- Proudfoot AEI, Handel TM, Johnson Z, Lau EK, LiWang P, Clark-Lewis I, Borlat F, Wells TNC, Kosco-Vilbois MH (2003) Glycosaminoglycan binding and oligomerization are essential

- for the *in vivo* activity of certain chemokines. *Proc Natl Acad Sci USA* **100**: 1885–1890
- Ralat LA, Ren M, Schilling AB, Tang W-J (2009) Protective role of Cys-178 against the inactivation and oligomerization of human insulin-degrading enzyme by oxidation and nitrosylation. *J Biol Chem* **284**: 34005–34018
- Sallusto F, Palermo B, Lenig D, Miettinen M, Matikainen S, Julkunen I, Forster R, Burgstahler R, Lipp M, Lanzavecchia A (1999) Distinct patterns and kinetics of chemokine production regulate dendritic cell function. *Eur J Immunol* **29**: 1617–1625
- Sato N, Kuziel WA, Melby PC, Reddick RL, Kostecki V, Zhao W, Maeda N, Ahuja SK, Ahuja SS (1999) Defects in the generation of IFN-gamma are overcome to control infection with *Leishmania donovani* in CC chemokine receptor (CCR) 5-, macrophage inflammatory protein-1 alpha-, or CCR2-deficient mice. *J Immunol* **163**: 5519–5525
- Shen Y, Joachimiak A, Rosner MR, Tang WJ (2006) Structures of human insulin-degrading enzyme reveal a new substrate recognition mechanism. *Nature* **443**: 870–874
- Sladek R, Rocheleau G, Rung J, Dina C, Shen L, Serre D, Boutin P, Vincent D, Belisle A, Hadjadj S, Balkau B, Heude B, Charpentier G, Hudson TJ, Montpetit A, Pshzhetsky AV, Prentki M, Posner BI, Balding DJ, Meyre D *et al* (2007) A genome-wide association study identifies novel risk loci for type 2 diabetes. *Nature* **445**: 881–885
- Svergun DI (1991) Mathematical methods in small-angle scattering data analysis. *J Appl Cryst* **24**: 485–492
- Tanaka Y, Adams DH, Hubscher S, Hirano H, Siebenlist U, Shaw S (1993) T-cell adhesion induced by proteoglycan-immobilized cytokine MIP-1 beta. *Nature* **361**: 79–82
- Teng MS, Shadbolt P, Fraser AG, Jansen G, McCafferty J (2008) Control of feeding behavior in *C. elegans* by human G protein-coupled receptors permits screening for agonist-expressing bacteria. *Proc Natl Acad Sci USA* **105**: 14826–14831
- van Dongen PGJ, Ernst MH (1984) Kinetics of reversible polymerization. *J Stat Phys* **37**: 301–324
- Wagner L, Yang OO, Garcia-Zepeda EA, Ge Y, Kalams SA, Walker BD, Pasternack MS, Luster AD (1998) Beta-chemokines are released from HIV-1-specific cytolytic T-cell granules complexed to proteoglycans. *Nature* **391**: 908–911
- Wells TNC, Power CA, Shaw JP, Proudfoot AEI (2006) Chemokine blockers—therapeutics in the making? *Trends Pharmacol Sci* **27**: 41–47
- Wolf M, Albrecht S, Märki C (2008) Proteolytic processing of chemokines: implications in physiological and pathological conditions. *Inter J Biochem Cell Biol* **40**: 1185–1198
- Wolf M, Clark-Lewis I, Buri C, Langen H, Lis M, Mazzucchelli L (2003) Cathepsin D specifically cleaves the chemokines macrophage inflammatory protein-1 alpha, macrophage inflammatory protein-1 beta, and SLC that are expressed in human breast cancer. *Am J Pathol* **162**: 1183–1190
- Wolpe SD, Davatellis G, Sherry B, Beutler B, Hesse DG, Nguyen HT, Moldawer LL, Nathan CF, Lowry SF, Cerami A (1988) Macrophages secrete a novel heparin-binding protein with inflammatory and neutrophil chemokinetic properties. *J Exp Med* **167**: 570–581

Supplemental Information

Methods

Cloning, Expression, and Purification of MIP-1 and IDE:

The synthetic genes that encode mature form of human MIP-1 and RANTES chemokines with optimization for E.coli codon usage, was constructed by synthetic PCR (Gao et al., 2003). Enterokinase cutting site (DDDDK) was included before the first amino acid. 12 overlapping primers were designed by DNAworks 2.4 (Hoover and Lubkowski, 2002), with KpnI and Not I site flanking the 5' and 3' end. Synthetic MIP-1 cDNA were cloned into pET32a (Novagen) and verified by DNA sequencing. MIP-1 α mutants were generated by site directed mutagenesis.

Chemokines were expressed as thioredoxin and His6 tag fusion proteins in BL21(DE3) cells. The fusion proteins were purified by Ni-NTA column as described previously (Guo et al., 2010) and further purified by a Source-Q column with an ascending NaCl gradient in the presence of 5mM EDTA.

Recombinant MIP-1 and RANTES proteins were obtained by removing fusion tags. 10 U of enterokinase (sigma) was combined with every mg fusion protein in 20mM Tris-HCl pH7.7, 5mM EDTA and incubated at 25°C for 16 hours. The reaction was desalted by PD-10 column (GE healthcare) then applied to Ni-NTA resin (Qiagen), non-binding fraction was collected then further purified by heparin affinity chromatography. Final products of MIP-1 were analyzed by MALDI-TOF

mass spectrometry, and its biological activity was assayed on THP-1 cells by chemotaxis assay (Fig. S1).

Wild type and mutant Human IDE proteins were expressed in E.coli Rosetta (DE3) with IPTG induction at 25°C for 16 hours. Recombinant IDE proteins were purified to homogeneity by Ni-NTA, Source-Q and Superdex S-200 columns as previously described (Im et al., 2007; Malito et al., 2008; Shen et al., 2006a).

Mass Spectrometry Analysis: For mass spectrometry analysis, enzyme reactions were carried out at 37°C by mixing equal volume of MIP-1 with IDE at the given molar ratio in the presence or absence of 0.8mg/ml heparin. 20µl reaction mixture was removed at indicated time, and stopped by 20µl stop buffer (200mM EDTA, 0.2% TFA). Samples were further incubated with 10mM TCEP at room temperature for 30 min to break the disulfide bonds and then subjected to either MALDI/TOF or LC-ESI-FTICR mass spectrometry analysis. For MALDI/TOF analysis, 10µl sample was purified by Zip-Tip C18 columns (Millipore), and applied to the metal plate with matrix (CHCA, in 70% ACN and 0.1% TFA). Mass spectra were obtained either in linear or positive reflector mode using a Voyager 4700 MALDI/TOF mass spectrometer (Applied Biosystems). For LC-ESI-FTICR-MS, MIP-1α samples (12µl) were injected into a nano RP-HPLC system (Dionex), with a C8 analytical column (Agilent). Peptides were eluted from the nano column with a linear gradient of 5-95% acetonitrile in 0.1% formic acid and sprayed into a LTQ-FT tandem MS instrument (Thermo Scientific). Spectra were acquired using positive ion nano ESI mode with the FTICR

acquiring precursor spectra from 200-2000 m/z. For tandem MS, precursor ions were fragmented by collision-induced dissociation (CID). MS/MS spectra were acquired in a data dependent manner from the 5 most intense precursor ions of each FTICR MS scan. The RAW data files are processed by Xtract™ function in Xcalibur™ (Thermo Fisher Scientific) to generate reduced data files containing the deconvoluted masses and intensities for MS spectra. For a reduced data file, all deconvoluted MS spectra are summed to create a single pseudo-MALDI TOF mass spectrum by use of an in-house developed program written in Python. In brief, the peaks in all MS spectra are merged and peaks with m/z values matching within 5 ppm are summed into a single peak with the summed intensity. MS and tandem MS/MS data were analyzed by online tools, FindPept (<http://ca.expasy.org/tools/findpept.html>), Mascot (http://www.matrixscience.com/search_form_select.html) and MassMatrix (<http://www.massmatrix.net>) (Xu and Freitas, 2009).

The confirmation of MIP-1 α degradation products by ^{18}O water labeling:

This technique utilizes a protease enzyme reaction in ^{18}O water to produce isotope-labeled peptides. ^{18}O labeling will result in 2Da mass addition, which can be resolved by comparing the isotope envelope pattern to ^{16}O samples. In contrast, any pre-existing fragments will not be modified and have identical isotope distribution. In our IDE-digested MIP-1 α spectra, all 8 fragments that represent the initial cleavage products (1-18 and 19-70, 1-45 and 46-70, 1-46 and 47-70, 1-48 and 49-70) could be identified. Peptides 1-18, 1-45, 1-46 and 1-48 were labeled with ^{18}O as shown by a mass shift in the isotope distribution;

while the other four peptides 19-70, 46-70, 47-70 and 49-70 were not labeled (Table S3, Figure S11).

Size exclusion chromatography: Purified human MIP-1 samples dialysis against phosphate buffer saline (PBS) pH 7.4 with or without 0.1mg/ml heparin, then concentrated to 1mg/ml using a centrifugal filter device (AmiconUltra4 3 kDa MWCO, Millipore). 100ul the concentrated protein was applied to an equilibrated Superdex200 10/300 GL size exclusion chromatography column. PBS with or without 0.1mg/ml heparin was used for equilibration of the column as well as for elution. The molecular mass standards used are thyroglobulin (670 kDa), γ -globulin (158 kDa), ovalbumin (44 kDa), myoglobin (17 kDa) and vitamin B12 (1.35 kDa).

The modeling of reversible MIP-1 polymers and fit to the experimental data:

The modeling of SAXS data was based on the RA₂ model of van Dongen and Ernst (van Dongen and Ernst, 1984). At equilibrium, the concentration of k-mers,

c_k should read $c_k = \frac{c_t}{2}(1 - \alpha)^2 \alpha^{k/2-1}$ where k can only be an even integer, c_t is total

MIP-1 monomer concentration, and $\alpha = 1 + \frac{K_d}{c_t} - \sqrt{\left(\frac{K_d}{c_t}\right)^2 + \frac{2K_d}{c_t}}$. Here, K_d is the

equilibrium dissociation constant for a dimer-dimer bond. This predicts that the

average degree of polymerization is $2 \cdot \left(\frac{1 + \alpha}{1 - \alpha}\right)$, which depends on c_t . The

theoretical scattering curves for uniform length polymers were calculated using

Crysol and then combined into the scattering curves expected for a polymer

distribution using Matlab. Fits to the experimental data were performed using

Matlab and included three adjustable parameters: a constant scattering background, the total scattered intensity and either the polymer length (for single-length fits) or the parameter α (for polymer length distribution fits). Denoting by $I_{theo}^{\alpha}(q)$ the theoretically expected scattering intensity for a polydisperse polymer solution characterized by the parameter α with the normalization condition $I_{fit}^{\alpha}(0)=1$, we fitted the experimental curves by minimizing the fit function $\int_0^{q_{max}} [I_0 \times I_{theo}^{\alpha}(q) - I_{exp}(q) + I_b]^2 dq/q_{max}$ with respect to α , the zero-angle scattered intensity I_0 and a q-independent background intensity I_b . Here q_{max} is the largest scattering wavevector for which data was collected. A similar procedure was used for the monodisperse polymer solution fit, where the adjustable parameter α is replaced by L, the polymer length. The fitting errors $I_0 \times I_{theo}^{\alpha}(q) - I_{exp}(q) + I_b$ are represented in the deviation curve.

MIP-1 α competition assay: MIP-1 α competition assay was performed as previously described. IDE enzyme activities were assayed using substrate V (7-Methoxycoumarin-4-yl-acetyl-NPPGFSAFK-2,4-dinitrophenyl) (Manolopoulou et al., 2009; Shen et al., 2006b). 85 μ l of 0.35 μ M substrate V was mixed with 10 μ l of MIP-1 α at various concentrations. The reactions were initiated by addition of 5 μ l of IDE protein (0.2mg/ml), carried out at 37 $^{\circ}$ C for 15min. The substrate V degradation was monitored by fluorescence intensity on a Tecan Safire microplate reader with excitation and emission wavelengths at 327nm and 395nm respectively. Data were plotted and analyzed with PRISM software (Graphpad).

Cellular Assays: IDE expression in BV-2 cells is knockdown by lenti-virus mediated shRNA expression. A set of 5 plasmids which encode shRNA targeting mouse IDE gene were purchased from Open Biosystem (RMM4534-NM-031156). Lenti-virus were produced by co-transfecting shRNA plasmids with pHR8.2ΔR packaging plasmid and pCMV VSVG envelope plasmid into HEK293T cells. Virus containing media was harvested 48hr post transfection. BV-2 cells were infected with virus for 24 hours in the presence of 8ug/ml polybrene, and then stable lines were obtained by 2-week selection with 5ug/ml puromycin. IDE knockdown levels were confirmed by western blotting with a polyclonal anti-IDE antibody. Secreted MIP-1 level from IDE knockdown BV-2 cells were measured by ELISA assays. Stable BV-2 cells lines were seed at 2.5×10^4 /well in 24-well plate one day before the assay. Fresh culture media with or without 10ng/ml LPS was changed (0.5ml/well) and after 3 hours incubation at 37°C media harvested. Chemokine levels in these samples were measured by anti-mouse MIP-1 α , MIP-1 β and RANTES ELISA kits (R&D system) according to manufactures instruction. Chemokine concentrations (pg/ml) were calculated from the standard curve measured within the same assay.

Chemotaxis Assay: Cell migration was measured in 96-well Multiscreen™ filter plate (Millipore) as described in (Gouwy et al., 2008). Cytokines were diluted into the assay medium (RPMI 1640 without phenol red, supplemented with 10mM HEPES pH7.4, 0.1% heat inactivated BSA) at indicated concentration. 150 μ l sample was placed in the lower well of 96-well receiver plate. THP-1 cells were washed once with dPBS, then resuspended in assay medium at a concentration

of 2.5×10^6 /ml. 100ul cell suspension was loaded into upper wells of 96-well filter plate (5µm pore size). Cells were allowed to migrate for 3 hrs at 37°C. After removing the upper 96-well filter plate, the cell number in the lower receiver plate were quantified using the ATPlite™ luminescence assay system (PerkinElmer) according to manufacturer's instruction. The chemotaxis index was calculated by dividing the luminescence values of the sample over assay medium alone.

Calcium Mobilization Assay: THP-1 cells were washed once, and then loaded with 2µM fura-2 AM (Invitrogen) in assay medium (same as chemotaxis assay) at 37°C for 30min. Subsequently, cells were washed once with dPBS then resuspended in assay medium at 10^6 cell/ml. 2ml fura-2 loaded cell suspension was transferred to a cuvette with a magnetic stirring bar. Fura-2 fluorescence was measured with a FluoroMax-3 fluorometer (HORIBA Jobin Yvon Inc.) at excitation wavelengths of 340 and 380 nm and emission wavelength of 510 nm. MIP-1α incubated with or without IDE were diluted into the assay medium, and added into cell suspension at indicated concentration.

Figure Legends

Figure S1 The assessment of recombinant MIP-1 proteins (A) WT MIP-1 α , (B) WT MIP-1 α (purchased from Peprtech), (C) WT MIP-1 β , (B) WT MIP-1 β (purchased from Peprtech), (E) MIP-1 α L3M V63M, (F) MIP-1 α D27A (G) RANTES and (H) MIP-1 α P8A in their purity by MALDI-TOF MS spectrum and in their *in vitro* chemotactic activity using THP-1 cells. Chemotactic response was expressed as mean chemotaxis index, and shown as the *insert* graph.

Figure S2 Density of the MIP-1 protein and complex of IDE_CF_E111Q with MIP-1 α . (A) the $2f_o-f_c$ map of the MIP-1 proteins at 2.5 δ level; (B). The composite omit map of the MIP1a in complex of IDE/MIP-1 α at 1.5 δ

Figure S3 The structure comparison of CCL chemokine structures. MIP-1 α crystal structure from our MIP-1 α polymer structure is compared with CCL family protein structures that are (A) monomer, (B) dimer, (C) tetramer available from RCSB database. The monomers in the dimer and tetramer were colored differently. The PDB codes are as listed.

Figure S4 Structure analysis of the dimer interaction of MIP-1 α (**S4-1**), MIP-1 β (**S4-2**) as well as that between IDE and MIP-1 α (**S4-3**). In **Figure S4-1** and **S4-2**, (A) Details of the hydrogen bond and salt bridge built between different monomers. (B) The accessible surface area (ASA) and buried surface area (BSA) of the interfacing residues between monomers. (C) The buried interface area between monomers. The area was calculated through the PISA server

(http://www.ebi.ac.uk/msd-srv/prot_int/cgi-bin/pisever). The monomer designation (A-D) is indicated in the figure on the right.

Figure S5 The sequence alignment of the CCL proteins (A) and phylogenetic tree of CCL proteins (B). The key residues involving MIP1 α dimer contact were colored red as the cysteine colored green.

Figure S6 $p(r)$ function distributions for 1mg/ml MIP-1 proteins without (left) or with (right) 0.1mg/ml heparin. With the use of a q -range of 0.0068 to 0.343, a maximum dimension (D_{\max}) and the interatomic distance distribution functions $p(r)$ were computed by GNOM.

Figure S7 SEC analysis of various concentrations of (A) MIP-1 α , (B) MIP-1 β and (C) MIP-1 α P8A. SEC was performed on S-200 column in phosphate-buffered saline (PBS). The elution volume of molecular standard proteins is indicated by the dotted lines.

Figure S8 Comparison of the MIP-1 α and MIP-1 β experimental SAXS data (black) with the theoretical scattering patterns from a single length polymer (green) or a polymer length distribution as calculated from our model (red). The size distribution of mass from polymer distribution is shown as an inset and the fitting error is shown under the fitting curve. The fitting errors $I_0 \times I_{theo}^a(q) - I_{exp}(q) + I_b$ are represented in the deviation curve. The D values from the fit function $\int_0^{q_{\max}} [I_0 \times I_{theo}^a(q) - I_{exp}(q) + I_b]^2 dq/q_{\max}$ for single length and polymer distribution are listed. Inset: size distribution of the polymers length distribution.

Figure S9 MIP-1 α mediated intracellular calcium response in THP-1 cells. (A) Dose-dependent changes of intracellular calcium concentrations by MIP-1 α . Fura-2 loaded THP-1 cells were stimulated with the indicated concentrations of MIP-1 α . Stimulus dependent $[Ca^{2+}]_i$ changes were monitored by ratio of fluorescence at 340nm over 380nm. The change of $[Ca^{2+}]_i$ is indicated by $\Delta F_{340}/F_{380}$ which is the difference between the peak F_{340}/F_{380} value after addition of MIP-1 α and basal level before stimulation. (B) MALDI-TOF-MS spectra of IDE digested MIP-1 α samples used in examining the effect of the degradation of MIP-1 α by IDE (Figure 5C).

Figure S10 Comparison of mass spectra of IDE digested MIP-1 α peptides in $H_2^{18}O$ and $H_2^{16}O$. IDE digested MIP-1 α peptides were analyzed by LC-ESI-FTICR MS. The spectra from digestion in $H_2^{16}O$ are shown in red; spectra from digestion in 50% $H_2^{18}O$ are shown in blue. Spectra from the same peptide fragments are overlaid and shown as (A) residues 1-48, (B) residues 49-70, (C) residues 1-46, (D) residues 47-70 and (E) residues 1-70.

Figure S11 Model of catalysis mechanism for IDE. MIP-1 α is depicted as red; IDE-N and IDE-C are depicted as light blue and grey surfaces, respectively. IDE^o is theoretically modeled based on the substrate free *E. coli* ptilysin (1Q21); IDE^c corresponds to the atomic coordinate of IDE-CF-E111Q-MIP-1 α (3H44). The detail description of mechanism is in the discussion.

Reference

- Gao, X., Yo, P., Keith, A., Ragan, T. J., and Harris, T. K. (2003). Thermodynamically balanced inside-out (TBIO) PCR-based gene synthesis: a novel method of primer design for high-fidelity assembly of longer gene sequences. *Nucleic Acids Res* 31, e143.
- Gouwy, M., Struyf, S., Noppen, S., Schutyser, E., Springael, J. Y., Parmentier, M., Proost, P., and Van Damme, J. (2008). Synergy between coproduced CC and CXC chemokines in monocyte chemotaxis through receptor-mediated events. *Mol Pharmacol* 74, 485-495.
- Guo, Q., Manolopoulou, M., Bian, Y., Schilling, A. B., and Tang, W.-J. (2010). Molecular Basis for the Recognition and Cleavages of IGF-II, TGF- α , and Amylin by Human Insulin-Degrading Enzyme. *Journal of Molecular Biology* 395, 430-443.
- Hoover, D. M., and Lubkowski, J. (2002). DNAWorks: an automated method for designing oligonucleotides for PCR-based gene synthesis. *Nucleic Acids Res* 30, e43.
- Im, H., Manolopoulou, M., Malito, E., Shen, Y., Zhao, J., Neant-Fery, M., Sun, C. Y., Meredith, S. C., Sisodia, S. S., Leissring, M. A., and Tang, W. J. (2007). Structure of substrate-free human insulin-degrading enzyme (IDE) and biophysical analysis of ATP-induced conformational switch of IDE. *J Biol Chem* 282, 25453-25463.
- Malito, E., Ralat, L. A., Manolopoulou, M., Tsay, J. L., Wadlington, N. L., and Tang, W.-J. (2008). Molecular bases for the recognition of the short peptide substrate and cysteine-directed modifications of human insulin-degrading enzyme. *Biochemistry* 47, 12822-12834.
- Manolopoulou, M., Guo, Q., Malito, E., Schilling, A. B., and Tang, W. J. (2009). Molecular basis of catalytic chamber-assisted unfolding and cleavage of human insulin by human insulin-degrading enzyme. *J Biol Chem* 284, 14177-14188.
- Shen, Y., Joachimiak, A., Rosner, M. R., and Tang, W.-J. (2006a). Structures of human insulin-degrading enzyme reveal a new substrate recognition mechanism. *Nature* 443, 870-874.
- Shen, Y., Joachimiak, A., Rosner, M. R., and Tang, W. J. (2006b). Structures of human insulin-degrading enzyme reveal a new substrate recognition mechanism. *Nature* 443, 870-874.
- van Dongen, P. G. J., and Ernst, M. H. (1984). Kinetics of reversible polymerization. *J Stat Phys* 37, 301-324.
- Xu, H., and Freitas, M. A. (2009). MassMatrix: a database search program for rapid characterization of proteins and peptides from tandem mass spectrometry data. *Proteomics* 9, 1548-1555.

Polymerization of human MIP-1 chemokines (CCL3 and CCL4) and clearance of MIP-1 by human insulin degrading enzyme

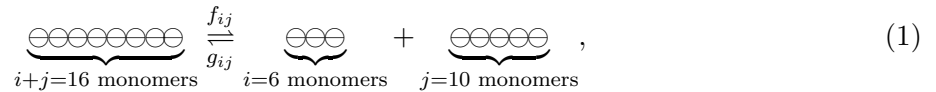
supplemental mathematical modeling

Ren *et al.*

1 Equilibrium polymer length distribution

1.1 Description of the polymerization model

Here we describe the polymerization model used in the main text. This model is the equilibrium version of the RA_2 model of Ref. [1]. We use it to describe a solution of MIP-1 dimers with concentration $c_t/2$ (*i.e.*, c_t is the total monomer concentration). These dimers can reversibly assemble into linear polymers according to the following scheme:



where f_{ij} and g_{ij} are the kinetic dissociation and association rates, respectively. Note that here each circle represents a dimer, *i.e.*, two monomers. In this approach, we assume that the MIP-1 dimer concentration is much larger than the dissociation constant corresponding to the dissociation of a dimer into monomers. Therefore we assume that only dimers or polymers of dimers are present throughout this section¹. As a consequence, i and j are assumed to be even integers in all the following.

The approach of Ref. [1] relies on two main assumptions:

- No circular polymers are formed. This is reasonable if the persistence length of the polymers (the typical length over which they bend due to thermal fluctuations) is much larger than their contour length.
- Identical chemical groups have *a priori* equal chemical reactivity. This means that the kinetic association constant g_{ij} in the reaction pictured in Eq. (1) is independent of i and j : $g_{ij} = g$. This is reasonable in the limit of long polymers. Indeed, in this limit the reactivity of the polymer's end groups should go to a well-defined constant.

¹The assumption that most of MIP-1 are either dimers or polymers is likely fulfilled in our SAXS experiments where $\sim 100 \mu\text{M}$ MIP-1 was used, and the dimerization constant of MIP-1 is estimated to be in nM range. Note however that relaxing this assumption, *i.e.*, taking the equilibrium between monomers and dimers into account does not modify the form of the polymer length distribution. Essentially, there is an effective dimer concentration lower than c_t , because a fraction of MIP-1 is monomeric.

1.2 Additional conditions

Assuming a constant g as discussed in the previous section, we enforce two additional conditions and deduce the value c_k of the equilibrium concentration of k -mers (polymers comprising k monomers).

1. *Normalization condition.* This requires that the total fragmentation rate of a k -mer be proportional to the number of dimer-dimer bonds in this k -mer. Since there are $k/2$ dimers in the k -mer, this number of bonds is equal to $k/2 - 1$. Similar to the above, this is expected in the limit of long polymers, as in this limit most fragmentation events occur deep within the polymer. At the locations of these events, the ends of the polymer are far enough from the fragmentation site for the fragmentation rate to be independent of their location. In other words, we assume that all bonds are equally breakable, in agreement with the assumption of *a priori* equal chemical reactivity. This condition reads:

$$\frac{1}{2} \sum_{i+j=k \text{ even}} f_{ij} = \lambda \left(\frac{k}{2} - 1 \right), \quad (2)$$

where λ is a proportionality constant and where the sum runs over all strictly positive even integers i and j whose sum is k (also an even integer).

2. *Detailed balance condition.* In a stationary state the number of k -mers lost to the i - and j -mers through fragmentation is exactly compensated by the number of k -mers formed out of i - and j -mers:

$$f_{ij}c_{i+j} = g_{ij}c_i c_j = g c_i c_j, \quad (3)$$

where the assumption $g_{ij} = g$ discussed in the previous section was used.

1.3 Equilibrium distribution

Combining Eqs. (2) and (3) and noting that $c_{i+j} = c_k$ for all terms in the sum, we obtain

$$\lambda \left(\frac{k}{2} - 1 \right) c_k = \frac{g}{2} \sum_{i+j=k \text{ even}} c_i c_j. \quad (4)$$

It can easily be checked by substitution into Eq. (4) that the solution of this recursion reads

$$c_k = \frac{2\lambda}{g} \left(\frac{g c_2}{2\lambda} \right)^{k/2}, \quad (5)$$

where the dimer concentration c_2 remains to be determined. This is done by imposing that the total monomer concentration in the solution is equal to c_t , which reads

$$c_t = \sum_{k=2,4,6,\dots,\infty} k c_k = \frac{4\lambda}{g} \left(c_2 \frac{d}{d c_2} \right) \sum_{l=1}^{+\infty} \left(\frac{g c_2}{2\lambda} \right)^l, \quad (6)$$

where we made the change of dummy variable $l = k/2$, which implies that the sum over l runs over all strictly positive integers. We can sum the geometric series in Eq. (6), noting that its convergence requires $g c_2 / 2\lambda < 1$:

$$c_t = \frac{2c_2}{(1 - g c_2 / 2\lambda)^2}. \quad (7)$$

We solve this quadratic equation for c_2 , which yields two solutions. One of these is such that $gc_2/2\lambda > 1$, which is unphysical as discussed above [this corresponds to a diverging series in Eq. (6), and therefore to an infinite total concentration]. The other solution is always well-behaved, and reads

$$\alpha = \frac{gc_2}{2\lambda} = 1 + \frac{2\lambda}{gc_t} - \sqrt{\left(\frac{2\lambda}{gc_t}\right)^2 + \frac{4\lambda}{gc_t}}. \quad (8)$$

1.4 Dimer-dimer dissociation constants

We define the equilibrium dissociation constant associated with the reaction Eq. (1) as

$$K_d(i, j) = \frac{c_i c_j}{c_{i+j}}. \quad (9)$$

Substituting the expression of Eq. (5) for the concentrations into this equation, we find that K_d does not depend on i and j , which reflect the fact that all bonds are treated as identical (they all have the same binding energy). In particular, K_d is equal to the dissociation constant of a tetramer into two dimers, and thus characterizes the binding affinity between MIP-1 dimers. It reads

$$K_d = \frac{2\lambda}{g}. \quad (10)$$

Combining Eqs. (3) and (9), we find that f_{ij} does not depend on i and j either and reads

$$f = gK_d. \quad (11)$$

Substituting Eq. (10) in Eqs. (5) and (8), we rewrite our polymer length distribution as a function of only two parameters: the binding affinity K_d between MIP-1 dimers and the total MIP-1 concentration c_t :

$$c_k = \frac{c_t}{2}(1 - \alpha)^2 \alpha^{k/2-1} \quad \text{with} \quad \alpha = 1 + \frac{K_d}{c_t} - \sqrt{\left(\frac{K_d}{c_t}\right)^2 + \frac{2K_d}{c_t}}, \quad (12)$$

where $0 \leq \alpha < 1$. Therefore the fraction c_k/c_t of polymers of length k depends on K_d/c_t only.

1.5 Discussion of the length distribution and average polymer length

To get a better feeling of the meaning of this distribution, we now turn our interest to the fraction of the total MIP-1 mass that is included in k -mers. We note that the mass comprised in k -mers is proportional to kc_k , *i.e.*, the number of monomers in each k -mer. Moreover, the total number of MIP-1 monomers is c_t , and therefore

$$\text{mass fraction}(k) = \frac{kc_k}{c_t} = \frac{k(1 - \alpha)^2 \alpha^{k/2-1}}{2}. \quad (13)$$

Interestingly, the relative mass distribution specified by this expression is a function of only one quantity: the ratio K_d/c_t of the dimer-dimer dissociation constant to the total monomer concentration. We illustrate this dependence in Fig. SM1.

To quantify the typical polymer size associated with the curves presented in this figure, we calculate the average of the distribution of Eq. (13). This quantity is also known as the degree of

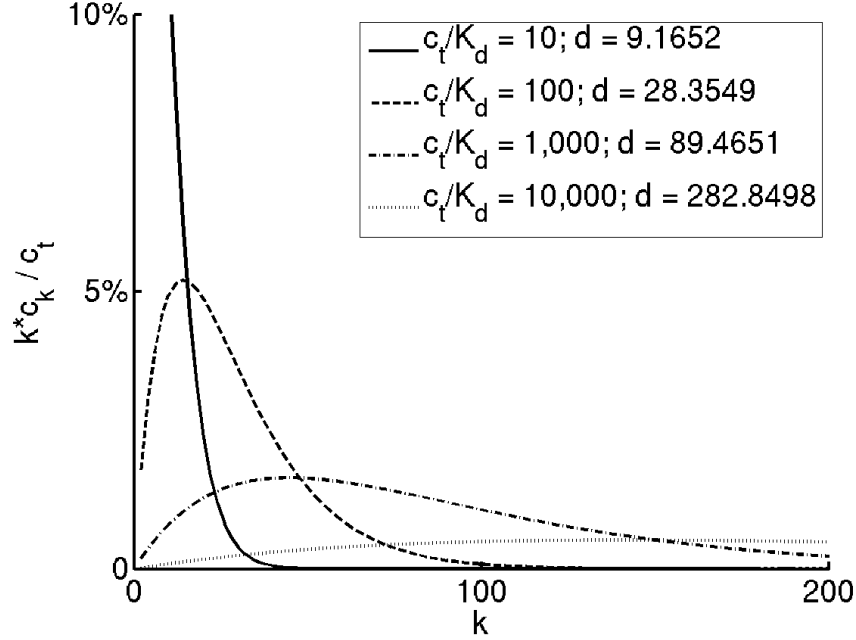


Figure SM1: Plots of the mass fraction of k -mers as expressed in Eq. (13) as a function of k for different values of the ratio c_t/K_d . In each case, the average degree of polymerization [Eq. (14)] is indicated in the legend. Since the distribution depends only on the ratio of c_t and K_d , the solid curve might represent the distribution for $c_t = 100 \mu\text{M}$ and $K_d = 10 \mu\text{M}$ just as well as the situation $c_t = 30 \mu\text{M}$ and $K_d = 3 \mu\text{M}$. The same type of comment holds for the other curves. Qualitatively, the average polymer size as well as the width of the size distribution increase for both increasing c_t (putting more monomers displaces the equilibrium towards the more associated forms) and decreasing K_d .

polymerization and reads:

$$\begin{aligned}
 d(\alpha) &= \sum_{k \text{ even}} k \times \text{mass fraction}(k) \\
 &= \frac{2(1-\alpha)^2}{\alpha} \sum_{l=1}^{+\infty} l^2 \alpha^l \\
 &= \frac{2(1-\alpha)^2}{\alpha} \left(\alpha \frac{d}{d\alpha} \right)^2 \sum_{l=1}^{+\infty} \alpha^l \\
 &= 2 \left(\frac{1+\alpha}{1-\alpha} \right). \tag{14}
 \end{aligned}$$

This measure of the polymer length can help us qualitatively understand the meaning of the dissociation constant K_d for the polymerization process. We see from Eq. (9) that K_d is expressed in units of concentration—it actually represents the characteristic concentration for the onset of polymerization. More specifically, if $c_t = 3K_d/2$, then $\alpha = 1/3$ and $d(\alpha) = 4$, meaning that the MIP-1 molecules are typically in the tetramer form. Lower values of c_t yield mostly dimeric MIP-1, and higher values lead to longer polymers.

The degree of polymerization $d(\alpha)$ is also related to the position of the peak of the distributions pictured in Fig. SM1. Indeed, this peak is characterized by

$$\frac{d[\text{mass fraction}(k)]}{dk} = 0 \quad \Leftrightarrow \quad k = k_{\text{peak}}(\alpha) = -\frac{2}{\ln(\alpha)} \quad (15)$$

Thus the following relationship between $d(\alpha)$ and $k_{\text{peak}}(\alpha)$ holds:

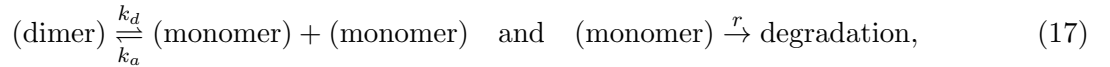
$$d(\alpha) = 2 \times \frac{1 + \exp[-2/k_{\text{peak}}(\alpha)]}{1 - \exp[-2/k_{\text{peak}}(\alpha)]} \sim 2k_{\text{peak}}(\alpha) \quad \text{as} \quad k_{\text{peak}} \rightarrow +\infty. \quad (16)$$

Therefore, for long polymers, the degree of polymerization is equal to twice the length of the most abundant species.

2 Chemokine gradient in the presence of polymerization

2.1 Description of the model

To better understand the interplay between MIP-1 degradation and its dimerization and polymerization in the formation of a spatial chemotactic gradient, we supplement the model of the previous section with the following reactions:



which account for MIP-1 dimerization and degradation. Only monomers are subject to degradation by the protease IDE, as discussed in the main text. The constant degradation rate r assumes a constant concentration of IDE in the region of interest.

We also describe the spatial structure of the MIP-1 gradient, and take into account the diffusion of the different MIP-1 species in a one-dimensional medium parametrized by the spatial coordinate x . For simplicity, we assume that they all have the same diffusion constant D . This yields the following rate equations for the concentrations of the various MIP-1 constructs:

$$\text{monomers:} \quad \frac{\partial c_1}{\partial t} = D \frac{\partial^2 c_1}{\partial x^2} - k_a c_1^2 + k_d c_2 - r c_1 \quad (18a)$$

$$\text{dimers:} \quad \frac{\partial c_2}{\partial t} = D \frac{\partial^2 c_2}{\partial x^2} + \frac{k_a}{2} c_1^2 - \frac{k_d}{2} c_2 - \sum_{i=2,4,6\dots} (g c_2 c_i - f c_{2+i}) \quad (18b)$$

$$k > 2 \text{ polymers:} \quad \frac{\partial c_k}{\partial t} = D \frac{\partial^2 c_k}{\partial x^2} + \frac{1}{2} \sum_{i+j=k \text{ even}} (g c_i c_j - f c_{i+j}) - \sum_{i=2,4,6\dots} (g c_k c_i - f c_{k+i}) \quad (18c)$$

where the concentrations are now taken to be space- and time-dependent and $c_1(x, t)$ is the monomer concentration. We consider a geometry corresponding to the physiological situation of a large² wound located in the $x = 0$ plane. Dendritic cells in the vicinity of this plane would start secreting MIP-1 at a constant rate J , which would then penetrate into the tissue in the direction of positive x s. No MIP-1 dimers or polymers go into or out of the $x = 0$ plane, and we demand that the chemokine concentration vanishes far away from the secretion site. This situation is described by the following boundary conditions:

$$D \frac{\partial c_1}{\partial x}(x = 0) = -J, \quad D \frac{\partial c_k}{\partial x}(x = 0) = 0 \text{ for all } k > 1 \quad \text{and} \quad c_k(x = +\infty) = 0 \text{ for all } k. \quad (19)$$

²In this context, ‘‘large’’ means larger than the depth of the MIP-1 gradient, which is typically 1 mm as discussed below.

2.2 Estimation of the parameters

In the following we assume that the diffusion constant for all MIP-1 species is of order $D = 1 \mu\text{m}^2 \text{s}^{-1}$, which is a typical value for objects with a size of order 10 nm in a medium ten times more viscous than water (this was estimated using the Stokes-Einstein formula—the increased viscosity compared to water is meant to account for the crowded environment of the tissue considered).

According to the main text, MIP-1 forms polymers with a typical degree of polymerization $d(\alpha) = 40$ when a total MIP-1 concentration $c_t \simeq 100 \mu\text{M}$ is used. Using Eq. (14), we find that this corresponds to $\alpha \simeq 0.95$. Combining Eqs. (7) and (10), this implies

$$K_d = \frac{(1 - \alpha)^2}{2\alpha} c_t \simeq 100 \text{ nM}. \quad (20)$$

In the following we assume that $f = 10^{-2} \text{ s}^{-1}$, a value chosen to yield a physiologically reasonable chemokine penetration depth of order 1 mm. Substituting into Eq. (11) yields $g = 10^5 \text{ M}^{-1} \text{ s}^{-1}$.

Consistent with the assumptions of the main text and the discussion of footnote 1, we assume that the dissociation constant $K'_d = k_d/k_a$ for the MIP-1 dimerization reaction is much smaller than K_d . Here we choose $K'_d = K_d/10 = 10 \text{ nM}$. We also choose $k_d = f = 10^{-2} \text{ s}^{-1}$, which implies $k_a = 10^6 \text{ M}^{-1} \text{ s}^{-1}$.

As described above, the source of MIP-1 in our model is the $x = 0$ plane, which can be thought of as a surface onto which MIP-1-secreting dendritic cells are grafted. Assuming that the typical inter-cell distance in this plane is of order $30 \mu\text{m}$ and using a MIP-1 secretion rate of 1 pg s^{-1} as reported in Ref. [2], we calculate that the secretion of MIP-1 per unit time per unit area in the plane is approximately $J = 2 \times 10^{-11} \text{ mol m}^{-2} \text{ s}^{-1}$.

Finally, we assume that MIP-1 degradation by IDE is slow compared to the other reactions described here. Note that if this were not the case and degradation were fast, all the chemokine would be degraded before having the time to dimerize or polymerize. We choose $r = f/10 = 10^{-3} \text{ s}^{-1}$, meaning that a monomer is typically degraded 1000 s after having been secreted. Given the fact that IDE typically degrades a MIP-1 monomer in a time of order 1 s (see main text), this assumption yields rates consistent with an IDE concentration equal to one thousandth of the typical MIP-1 monomer concentration. In the next section we show that the assumptions described here yield MIP-1 monomer concentrations of the order of 100 nM, which implies concentrations of IDE in the 100 pM range.

According to these considerations, our model comprises only one arbitrarily chosen parameter k_d . Moreover, the value of this rate constant has little influence on the results presented in the next section as long as it is significantly larger than r . Our model can thus be expected to offer some valuable insight into the physiological situation.

2.3 Results

We evolve the reaction-diffusion equations Eqs. (18) and (19) numerically starting from a situation where all concentrations are zero until a steady-state is reached. In Fig. 4A of the main text and in the following we present the results from three different situations, which illustrates the role of MIP-1 dimerization and polymerization in the shaping of a chemotactic gradient:

1. *Monomers only.* The numerical values of Sec. 2.2 are used, except for k_a , which we set to zero. This prevents the formation of any dimers or polymers, and yields an exponential decay of the chemotactic gradient which is described by the analytical formula

$$c_1(x, t = +\infty) = \frac{J}{\sqrt{r}} e^{-\sqrt{r}x}. \quad (21)$$

2. *Monomers and dimers.* The numerical values of Sec. 2.2 are used, except for g , which we set to zero. This prevents the formation of any polymers, but allows for dimers. The resulting steady-state monomer and dimer concentration profiles are shown in Fig. SM2(a)
3. *Monomers, dimers and polymers.* All numerical values of Sec. 2.2 are used, meaning that monomers, dimers and polymers are all present. The resulting steady-state concentration profiles are shown in Fig. SM2(b), and the average degree of polymerization of the polymers as a function of x is illustrated in Fig. SM2(c).

In the following we assume that only the MIP-1 monomer has a chemotactic activity, in agreement with Ref. [3]. It is thus interesting to compare the monomer concentration profiles for the three cases considered, which we do in Fig. SM2(d).

One common feature of the “monomers and dimers” and the “monomers, dimers and polymers” profiles plotted in this figure is a boundary region with a steep slope for small ($< 10 \mu\text{m}$) values of x . This is due to the fact that the source in $x = 0$ produces only monomers. Shortly after having been secreted, these monomers react together to form dimers and polymers, hence a decrease in the monomer concentration. Since these aggregation reactions are much faster than the monomer degradation, the amount of monomers degraded in this region is negligible, and the ratios between the various concentrations are locally close to their equilibrium values. Had we assumed that the dendritic cells secrete not monomers, but a mixture of dimers and polymers, those species would also have reached chemical equilibrium within $\sim 10 \mu\text{m}$ of the secretion site, and therefore the shape of the chemotactic gradient outside of that region would be much the same as the one presented here.

There are three noteworthy consequences of MIP-1 aggregation, all of which are more pronounced in the “monomers, dimers and polymers” case than in the “monomers and dimers” case:

- the monomer concentration for small x is reduced compared to the “monomers only” case, due to the assembly of the monomers into higher-order aggregates.
- the slope of the monomer profile is reduced, especially for small x , as degradation proceeds at a slower rate because of the smaller monomer concentration and also because the monomer pool is constantly replenished through the disassembly of the higher-order aggregates.
- the chemotactic gradient reaches further away from the secretion point, which could enable the recruitment of macrophages from a longer distance.

Interestingly, the MIP-1 profile plateaus at intermediate distances in the “monomers, dimers and polymers” case, which suggests that macrophages in this region might not be directed to the inflammation site, but would rather undergo random motion. More quantitatively, it has been reported that chemotaxis can occur only if the chemoattractant concentration drops by more than a quantity of order 1% across the cell length [4, 5]. Denoting the cell size by $a \simeq 10 \mu\text{m}$, this can be expressed mathematically by

$$\frac{c(x) - c(x + a)}{c(x)} > 1\% \quad \Leftrightarrow \quad \left| \frac{1}{c} \frac{\partial c}{\partial x} \right| > \frac{1}{100a} \simeq 10^3 \text{ m}^{-1}, \quad (22)$$

where the equivalence holds if the chemotactic gradient is smooth on length scales of the order of a . As reported in Fig. 4A of the main text, we applied this criterion to the profiles calculated in the “monomers, dimers and polymers” case, and found that the gradient can induce chemotaxis only for³ $x > 530 \mu\text{m}$.

³In the example considered here, the “monomers only” and “monomers and dimers” cases yield chemoattraction for all values of x . Note that the boundary region $x < 10 \mu\text{m}$ is not considered in this discussion.

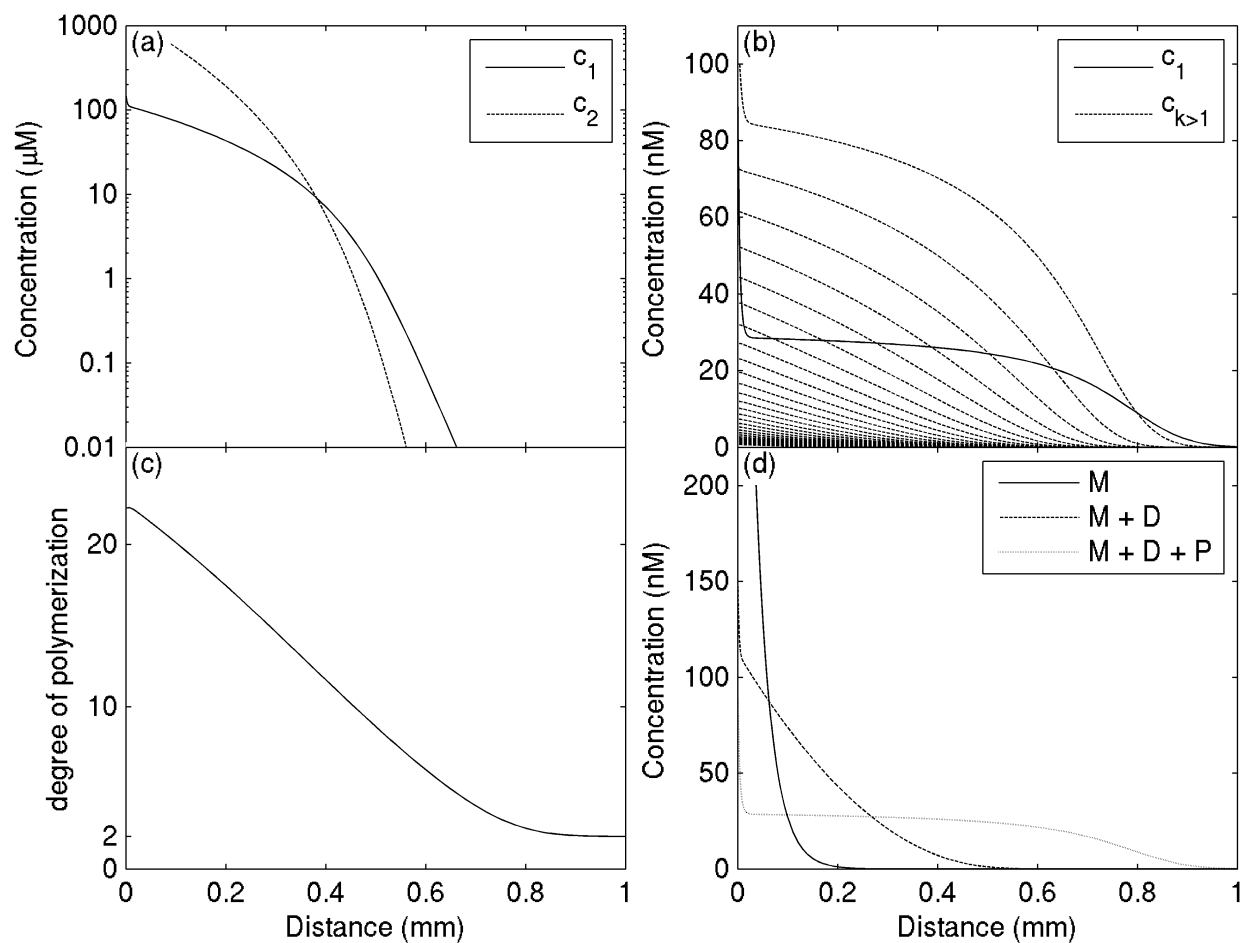


Figure SM2: MIP-1 concentration profiles as calculated from our model. (a) linear-logarithmic plot of the monomer (solid line) and dimer (dashed line) steady-state concentration profiles in the absence of polymerization. Note that most MIP-1 is in its dimer form for small x , *i.e.*, where large concentrations of MIP-1 are present. MIP-1 degradation is considerably hindered in these regions as only a small fraction of the MIP-1 (the monomeric fraction) is accessible to degradation. In regions where the total MIP concentration is smaller than K'_d , monomers are predominant and degradation proceeds unabated. (b) linear-linear plot of the monomer (solid line) and polymer (dashed line) steady-state concentration profiles. The uppermost dashed line represents the dimer concentration, the second one the tetramer concentration, the third the hexamer concentration and so on. (c) Average degree of polymerization as a function of x for the data presented in (b). Highly polymerized forms of MIP-1 dominate for small x and disappear as the chemokine is slowly degraded. Beyond $x = 800 \mu\text{m}$, dimers are the dominant aggregated form of MIP-1, although it is seen in (b) that they are less abundant than monomers. (d) Comparison between the monomer concentrations in the three cases enumerated in Sec. 2.3 as in Fig. 4A of the main text, but using a linear-linear scale instead of a linear-logarithmic one.

These effects might be relevant for macrophage recruitment *in vivo*. Since dimerization and polymerization occur only when a relatively large concentration of MIP-1 is present, we would expect them to preferentially happen following a severe infection. In this situation it could be physiologically profitable to target macrophages to an extended region surrounding the infection site rather than directing them to its exact location. Also, the chemotactic gradient is more extended when polymerization occurs, which would allow the recruitment of macrophages from a wider area, thus providing a more dramatic response to the infection.

References

- [1] P G J van Dongen and M H Ernst. Kinetics of reversible polymerization. *J. Stat. Phys.*, 37(3–4):301–324, 1984.
- [2] Federica Sallusto, Alfonso Martín-Fontecha, and Antonio Lanzavecchia. *Dendritic cell traffic control by chemokines*, volume 1, pages 79–89. Birkhäuser Verlag, 2006.
- [3] Samantha J Allen, Susan E Crown, and Tracy M Handel. Chemokine: receptor structure, interactions, and antagonism. *Annu Rev Immunol*, 25:787–820, 2007.
- [4] Pablo A Iglesias and Peter N Devreotes. Navigating through models of chemotaxis. *Curr Opin Cell Biol*, 20(1):35–40, Feb 2008.
- [5] Jason S King and Robert H Insall. Chemotaxis: finding the way forward with Dictyostelium. *Trends Cell Biol*, 19(10):523–30, Oct 2009.

Figure S1

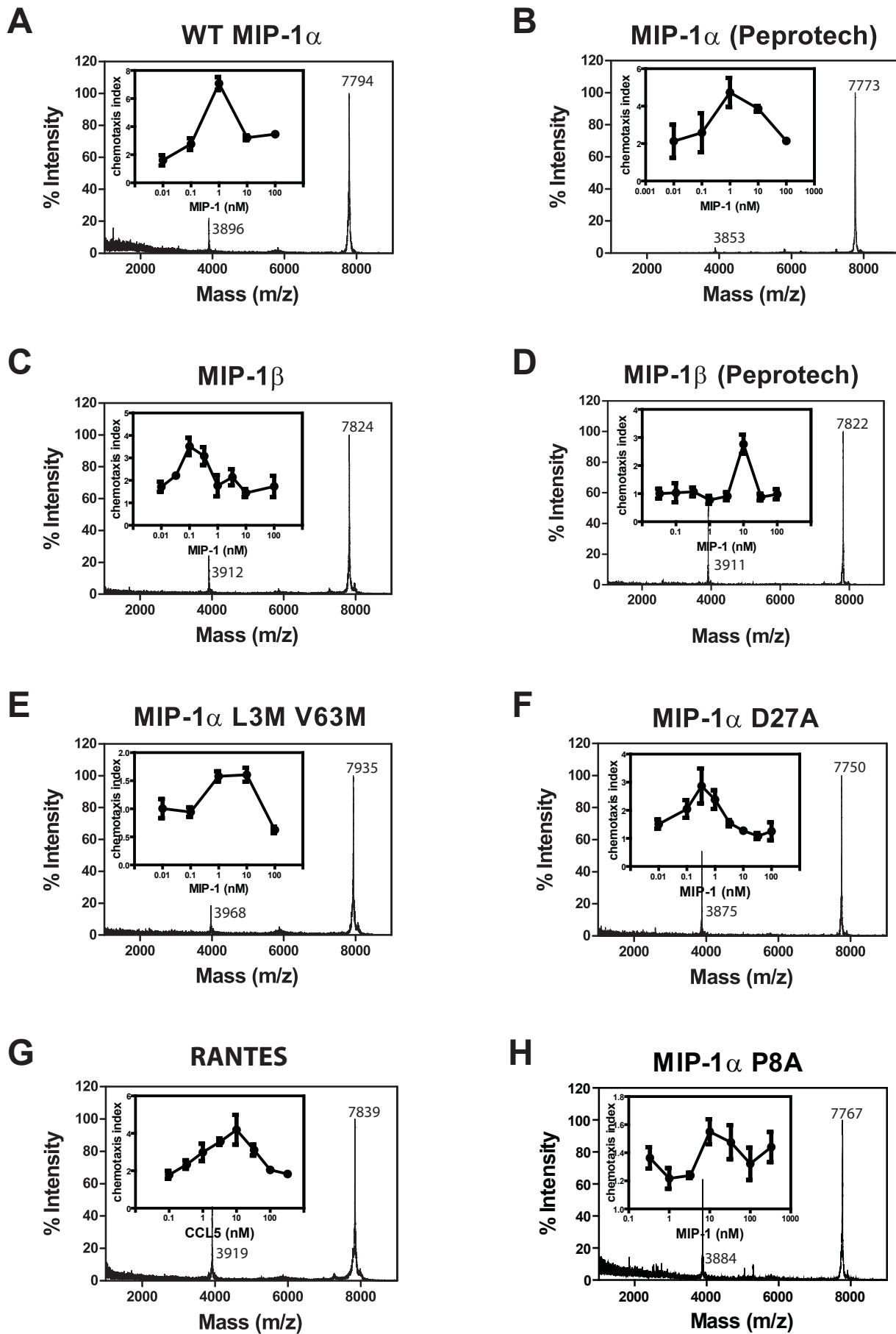
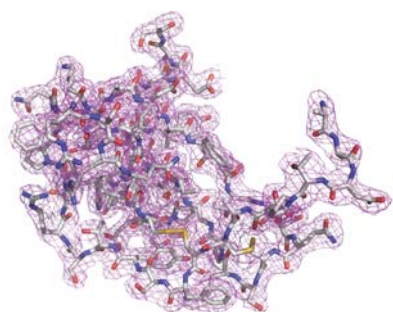
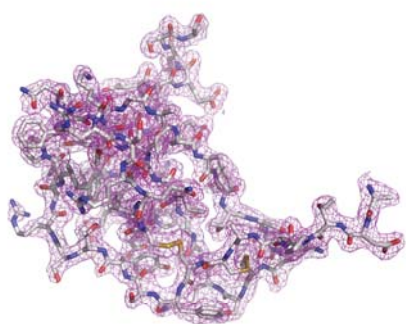


Figure S2

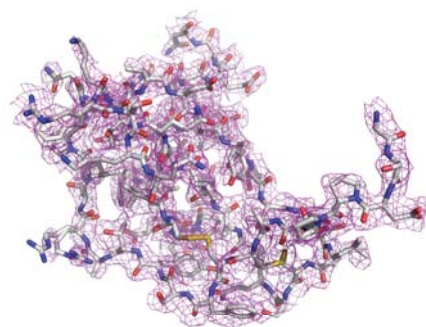
A



MIP-1 α

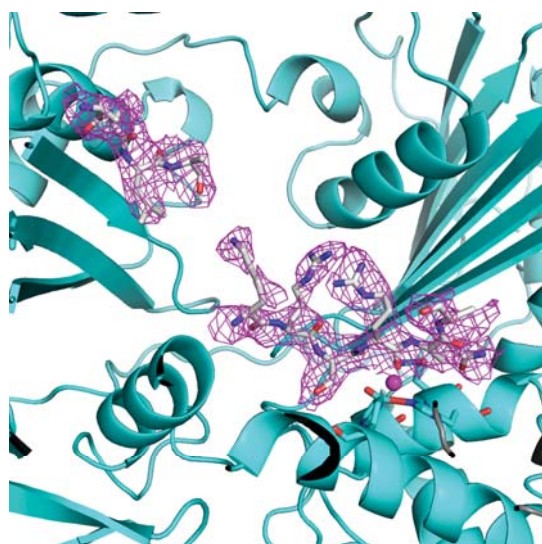


MIP-1 α D27A



MIP-1 β

B



IDE/MIP-1 α

Figure S3

A



MIP-1 α (2x69)



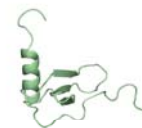
CCL1 (1EL0)



CCL7(1BO0)



CCL8(1ESR)



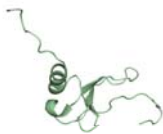
CCL11(1EOT)



CCL13(2RA4)



CCL15(2HCC)



CCL23(1G91)



CCL24(1EIG)

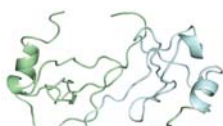


CCL26(1G2S)

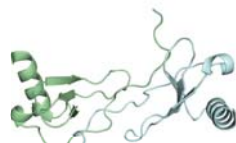
B



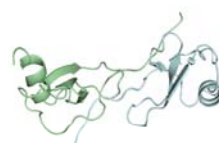
MIP-1 α (2x69)



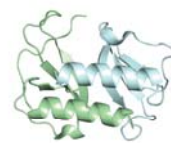
MIP-1 α (1B53)



CCL4(1HUM)

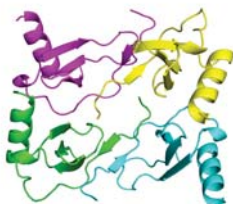


CCL5(1U4L)



CCL20(2HCI)

C



MIP-1 α (2x69)

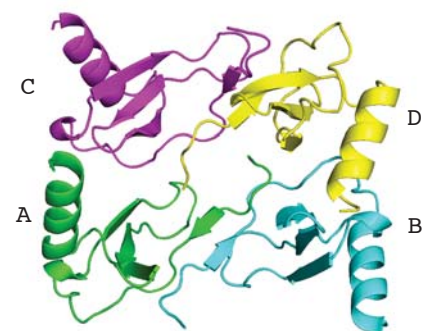


CCL14(2Q8T)

Figure S4-1

A

Residue		Distance		Residue	
Intra layer (between A and B)					
A	SER 14[OG]	2.67	B	ASP 6[OD2]	
A	CYS 51[N]	3.21	B	ASP 6[O]	
A	CYS 11[N]	3.22	B	THR 9[O]	
A	THR 9[N]	2.70	B	CYS 11[O]	
A	CYS 11[O]	2.87	B	THR 9[N]	
A	THR 9[O]	2.89	B	CYS 11[N]	
A	ASP 6[OD2]	3.21	B	SER 14[OG]	
A	ASP 6[OD1]	3.67	B	THR 16[OG1]	
A	ASP 6[O]	3.20	B	CYS 51[N]	
Crosslink (between A and D)					
A	SER 32[N]	3.59	D	ALA 5[O]	
A	SER 32[OG]	3.69	D	ASP 6[OD2]	
A	SER 33[N]	3.20	D	ASP 6[OD2]	
A	ASP 6[OD2]	3.40	D	SER 32[OG]	
A	ASP 6[OD1]	3.02	D	SER 33[N]	
A	ASP 6[OD2]	3.41	D	SER 33[OG]	
Interlayer(Between B and D)					
B	SER 17[OG]	3.79	D	SER 33[O]	
B	ARG 18[NH1]	3.55	D	GLU 30[OE1]	
B	ARG 46[N]	2.74	D	GLU 67[OE1]	
B	ARG 46[NE]	2.87	D	ASP 27[OD1]	
B	ARG 46[NH1]	2.92	D	LEU 66[O]	
B	ARG 46[NH2]	3.69	D	ALA 26[O]	
B	ARG 48[NH1]	3.85	D	GLU 30[OE2]	
B	ARG 48[NH2]	3.19	D	TYR 28[OH]	
B	TYR 15[O]	2.82	D	SER 33[OG]	
B	ARG 18[NH1]	3.55	D	GLU 30[OE1]	
B	ARG 46[NE]	2.87	D	ASP 27[OD1]	
B	ARG 46[NH2]	3.49	D	ASP 27[OD1]	
B	ARG 46[NH2]	3.98	D	ASP 27[OD2]	
B	ARG 48[NH1]	3.85	D	GLU 30[OE2]	



B

Residue	ASA(Å ²)	BSA(Å ²)
B SER 14	80.82	32.02
B TYR 15	62.20	12.67
B THR 16	40.89	8.14
B SER 17	105.57	26.97
B ARG 18	197.98	87.34
B ASN 23	113.41	27.02
B PHE 24	102.94	85.60
B THR 44	17.96	11.66
B LYS 45	141.14	39.21
B ARG 46	193.14	124.97
B ARG 48	145.30	84.39

Residue	ASA(Å ²)	BSA(Å ²)
D ALA 26	51.32	9.20
D ASP 27	57.58	35.45
D TYR 28	37.72	24.16
D PHE 29	90.78	24.95
D GLU 30	119.10	40.94
D THR 31	16.49	0.25
D SER 32	45.37	1.11
D SER 33	118.81	71.42
D GLN 34	156.14	25.30
D PRO 38	92.73	25.27
D GLY 39	1.60	0.29
D PRO 54	32.43	22.18
D SER 55	83.54	0.73
D GLN 60	96.51	0.61
D VAL 63	27.43	14.90
D SER 64	43.34	15.73
D LEU 66	55.26	30.83
D GLU 67	104.99	104.37
D LEU 68	150.12	58.39
D SER 69	134.67	18.50

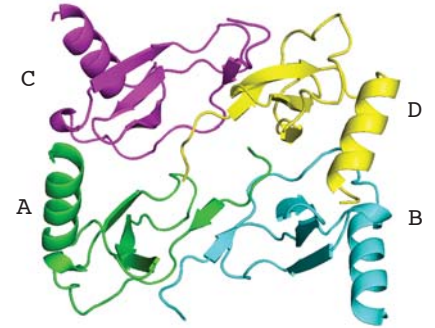
C

Monomer1	Monomer2	Interface(Å ²)
A	B	678.2
A	D	286.5
B	D	533.4

Figure S4-2

A

Residue		Distance	Residue	
Intra layer (between A and B)				
A	SER 14[OG]	3.53	B	ASP 6[OD1]
A	CYS 51[N]	3.04	B	ASP 6[O]
A	CYS 11[N]	2.69	B	THR 9[O]
A	THR 9[N]	2.67	B	CYS 11[O]
A	CYS 11[O]	2.61	B	THR 9[N]
A	THR 9[O]	2.81	B	CYS 11[N]
A	ASP 6[OD1]	2.60	B	SER 14[OG]
A	ASP 6[O]	3.05	B	CYS 51[N]
Crosslink (between A and D)				
A	SER 5[N]	2.69	D	GLU 30[O]
A	SER 32[OG]	2.65	D	ASP 6[OD1]
A	SER 33[N]	3.41	D	ASP 5[O]
A	SER 34[N]	2.79	D	ASP 6[OD1]
A	ASP 5[O]	2.84	D	SER 33[N]
A	ASP 6[OD2]	2.86	D	SER 33[N]
A	ASP 6[OD1]	2.42	D	SER 33[OG]
Interlayer(Between B and D)				
B	LYS 45[N]	2.90	D	GLU 67[OE1]
B	ARG 46[N]	3.19	D	GLU 67[OE1]
B	ARG 48[NZ]	3.64	D	ASP 27[OD1]
B	ARG 48[NZ]	3.71	D	ASP 27[OD2]
B	TYR 15[O]	3.21	D	SER 33[OG]
B	ARG 46[NE]	3.99	D	ASP 27[OD1]
B	ARG 48[NZ]	3.64	D	ASP 27[OD1]
B	ARG 48[NZ]	3.71	D	TYR 27[OD2]



B

Residue	ASA (\AA^2)	BSA (\AA^2)
B SER 14	81.14	41.77
B TYR 15	67.29	10.44
B THR 16	33.95	7.34
B ALA 17	109.07	19.77
B ARG 18	196.30	109.47
B PRO 21	61.88	21.31
B ASN 23	113.35	33.69
B PHE 24	109.24	102.99
B THR 44	13.13	7.70
B LYS 45	137.78	42.52
B ARG 46	179.35	79.95
B ARG 48	120.98	66.23

Residue	ASA (\AA^2)	BSA (\AA^2)
D VAL 26	71.40	2.09
D ASP 27	68.21	32.85
D TYR 28	46.32	33.43
D TYR 29	88.16	10.87
D GLU 30	99.73	22.80
D THR 31	14.14	5.83
D SER 32	37.97	1.85
D SER 33	113.65	68.65
D GLN 34	156.79	24.75
D PRO 38	96.06	45.20
D ALA 39	0.58	0.58
D PRO 54	32.26	5.18
D VAL 63	26.58	14.22
D TYR 64	141.06	50.79
D LEU 66	40.03	23.85
D GLU 67	106.15	104.56
D LEU 68	126.70	67.47
D ASN 69	146.99	2.33

C

Monmer1	Monmer2	Interface (\AA^2)
A	B	604.8
A	D	271.2
B	D	530.2

Figure S4-3

IDE Residue		Distance	MIP-1 α Residue	
GLY	361[N]	3.11	ALA	1[O]
HIS	332[ND1]	3.82	SER	2[OG]
HIS	336[N]	3.40	SER	2[OG]
GLY	339[O]	2.94	ALA	1[N]
GLU	341[OE1]	2.63	ALA	1[N]
LEU	359[O]	3.10	ALA	1[N]
TYR	609[OH]	3.74	SER	2[N]
GLY	361[O]	3.17	LEU	3[N]
THR	220[OG1]	3.02	SER	18[OG]
THR	142[N]	2.99	SER	18[O]
GLN	111[NE2]	3.46	SER	18[O]
HIS	112[NE2]	2.80	ARG	19[O]
HIS	108[NE2]	3.53	ARG	19[O]
ASN	139[ND2]	2.63	GLN	20[O]
THR	142[O]	3.31	SER	18[N]
GLU	189[OE2]	2.81	ARG	19[N]
ALA	831[OH]	3.76	ALAL	21[N]

Figure S5

A

	MW(kd)	PI	id(%)	Receptor		1	11	21	31			
h_CCL3	7.8	4.77	100.0	CCR1/5	-----	ASLAADTPTA	CCFSYTSRQ	IPQNFADYF	ETSS	QCSKPGV		
h_CCL4	7.8	4.77	67.1	CCR5	-----	APMGSDPPTA	CCFSYTARK	LPRNFVVDY	ETSS	LCSQPAV		
h_CCL1	8.6	9.91	32.4	CCR8	-----	SKSMQVPPSR	CCFSFAEQE	IPLRAILCY	RNTSS	ICSNEGL		
h_CCL2	8.7	9.39	34.2	CCR2	-----	QPDAINAPVT	CCYNFTNRK	ISVQRLAS	YRRITSS	KCPKEAV		
h_CCL5	7.9	9.24	44.3	CCR1/3/5	-----	SPYS	SDTTP	CCFAYIARP	LPRAHIKY	EYFYTSG	KCSNPAV	
m_CCL6	10.7	9.22	33.3	CCR3/5	GLIQEIE	KEDRRYNPPI	IHQGFQD	TSSD	CCFSYATQ	IPCKRFIY	YFPTSG	GCIKPGI
h_CCL7	9.0	9.74	31.6	CCR2	-----	QPVGINTSTT	CCYRFINKK	IPKORLES	YRRITSS	HCPREAV		
h_CCL8	8.9	9.30	34.2	CCR2/5	-----	QPDSVSIPIT	CCFNVINRK	IPIQRLES	YTRITNI	QCPKEAV		
m_CCL9/10	11.6	8.87	28.4	CCR1	QITHATETKEV	QSSSLKAQQGLE	IEFMHMGFQD	SSD	CCLSYSNR	IQCSRFIG	YFPTSG	GCTRPGI
h_CCL11	8.4	9.92	34.2	CCR3	-----	GPASV	PTT	CCFNLANRK	IPLORLES	YRRITSG	KCPQKAV	
m_CCL12	9.3	9.27	29.3	CCR2/5	-----	GPDAVSTPVT	CCYNVVKQK	IHVRKLKS	YRRITSS	QCPREAV		
h_CCL13	8.7	9.98	35.5	CCR2	-----	MQPDALNVPST	CCFTFSSKK	ISLQRLKS	YVITTS	RCPQKAV		
h_CCL14	8.7	8.73	45.3	CCR1	-----	TKTESSSRGPYH	PSE	CCFTYITTK	IPRQRIMDY	YETNS	QCSKPGI	
h_CCL15	7.2	9.01	47.9	CCR1/3	-----	HFAAD	CCTSYISQS	IPCSLMKS	YFETSS	ECSKPGV		
h_CCL16	11.5	9.65	23.8	CCR1/3	-----	SRSQPKVPEWV	NTPST	CCLKYVEKV	LPRRLVVG	YRKALN	CHLPAI	
h_CCL17	8.1	9.46	25.0	CCR4	-----	ARGTNVGR	ECCLEYFKGA	IPLRKLKT	WYQTS	DCSRDAI		
h_CCL18	7.9	9.21	60.0	Unknown	-----	AQVGTN	KEL	CCLVYTSWQ	IPQKFLV	DYSETSP	QCPKPGV	
h_CCL19	8.8	9.84	26.3	CCR7	-----	GTNDAED	CCLSVTQKP	IPGYIVRN	FHYLLIKD	GCRPAV		
h_CCL20	7.9	9.70	27.0	CCR6	-----	ASNFD	CCLGYTDRI	LHPKFIVG	FTRQLANE	GCDINAI		
h_CCL21	12.3	10.04	21.1	CCR7	-----	SDGGAQD	CCLKYSQRK	IPAKVVRS	YRKQEPSL	GCSIPAI		
h_CCL22	8.1	9.07	29.6	CCR4	-----	GPYGANMEDSV	CCRDYVRYR	LPLRVVKH	FYWTSD	SCPRPGV		
h_CCL23	8.9	9.38	44.2	CCR3	-----	MDRFHATSAD	CCISYTPRS	IPCSLLES	YFETNS	ECSKPGV		
h_CCL24	8.3	9.97	35.1	CCR3	-----	VVIPSP	CCMFVSKR	IPENRVVS	YQLSSRS	TCLKAGV		
h_CCL25	14.2	10.30	14.2	CCR9	-----	QGVFED	CCLAYHYPIG	WAVLRRAWT	YRIOEVSG	SCNLPA		
h_CCL26	8.4	10.22	37.5	CCR3	-----	TRGS	DISKT	CCFCQYSHKP	LPWTWVRS	YEFTSN	SQSRVAV	
h_CCL27	10.2	9.10	11.1	CCR10	-----	FLLPPTA	CCTQLYRKP	LSDKLLRK	VIQVELQ	EADGD	CHLQAF	
h_CCL28	12.4	10.23	11.0	CCR10	-----	SEAILPIASS	CCTEVSHH	ISRRLLE	RVNMCR	IQRADGD	CDLAAV	
h_CCL3					41	IFLTKRSR	QVCADPSE	EWVQKYVS	DL	ELSA	-----	70
h_CCL4						VFQTKRSK	QVCADPSE	SWVQYVY	DL	ELN	-----	69
h_CCL1						IFKLRGK	EACALDTV	GWVQRHRK	ML	RHCPSKRR	-----	74
h_CCL2						IFKTIVAK	EICADPKQ	KWVQDSMD	HL	DQOTQTPKT	-----	76
h_CCL5						VFVTRKNR	QVCANPEK	KWVREYIN	SL	EMS	-----	68
m_CCL6						IFISRRGT	QVCADPSD	RRVORCLS	TL	KOG	PRSGNKVIA	95
h_CCL7						IFKTKLDK	EICADPTQ	KWVQDFMK	HL	DKKTQTPKL	-----	76
h_CCL8						IFKTORGK	EVCADPKE	RWVRDSMK	HL	DQIFQNLKP	-----	76
m_CCL9/10						IFISKRGF	QVCANPSD	RRVORCIE	RL	EQNSQPRTYKQ	-----	101
h_CCL11						IFKTKLAK	DICADPKK	KWVQDSMK	YL	DQKSPTPKP	-----	74
m_CCL12						IFRTILDK	EICADPKE	KWVKNSIN	HL	DKTSQTFILEPSCLG	-----	82
h_CCL13						IFRTKLGK	EICADPKE	KWVQNYMK	HL	GRKAHTLKT	-----	76
h_CCL14						VFITKRGH	SVCTNPSD	KWVQDYIK	DM	KEN	-----	74
h_CCL15						IFLTKKGR	QVCAKPSG	PGVQDCMK	KL	KPYSI	-----	66
h_CCL16						IFVTKRNR	EVCTNPND	DWVQYIKDPNL	PLL	PTRNLSTVKIITAKNGQPQLLSQ	-----	100
h_CCL17						VFVTVOGR	AICSDPNN	KRVKNAVK	YL	OSLRS	-----	71
h_CCL18						ILLTKRGR	QICADPNK	KWVQYIS	DL	KLNA	-----	69
h_CCL19						VFITLRGR	QLCAPPDQ	PWVERIQ	RL	ORTSAKMRRSS	-----	77
h_CCL20						IFHTKKKL	SVCANPKQ	TWVKYIVR	LL	SKKVKN	-----	69
h_CCL21						LFVPRKRS	QAEICADPKE	LWVQQLMQ	HL	DKTPSPQKPAQGCRKDRGASKTGKKGKSGKGRKTERSQTPKGP	-----	111
h_CCL22						VLVTRFDK	EICADPRV	PWVKMILN	KL	SQ	-----	69
h_CCL23						IFLTKKGR	RFCANPSD	KQVQVCMR	ML	KLDTRIKTRKN	-----	77
h_CCL24						IFTTKKGQ	QSCGDPKQ	EWVQRYMK	NL	DAKOKKASPR	-----	73
h_CCL25						IFVLPKRHR	KVCGNPKS	REVQRAMK	LL	DARNKVFAKLHHNMQTFQAGPHAVKLLSSGNSKLSSSKFSNPISSSRKNVSLILISANGL	127	
h_CCL26						IFTTKRGR	KVCTHPRK	KWVQYIS	LL	KTPKQL	-----	71
h_CCL27						VLHLAQRS	ICIHQNPSSL	QWFEHQER	KL	HGTLPKLNFGLRKM	-----	88
h_CCL28						ILHVKRRR	ICVSPHNHTVKQ	WMKVQA	AKKNGKGNV	CHRKKHHGKRNSNRAHQKHETYGHKTPY	-----	108

B.

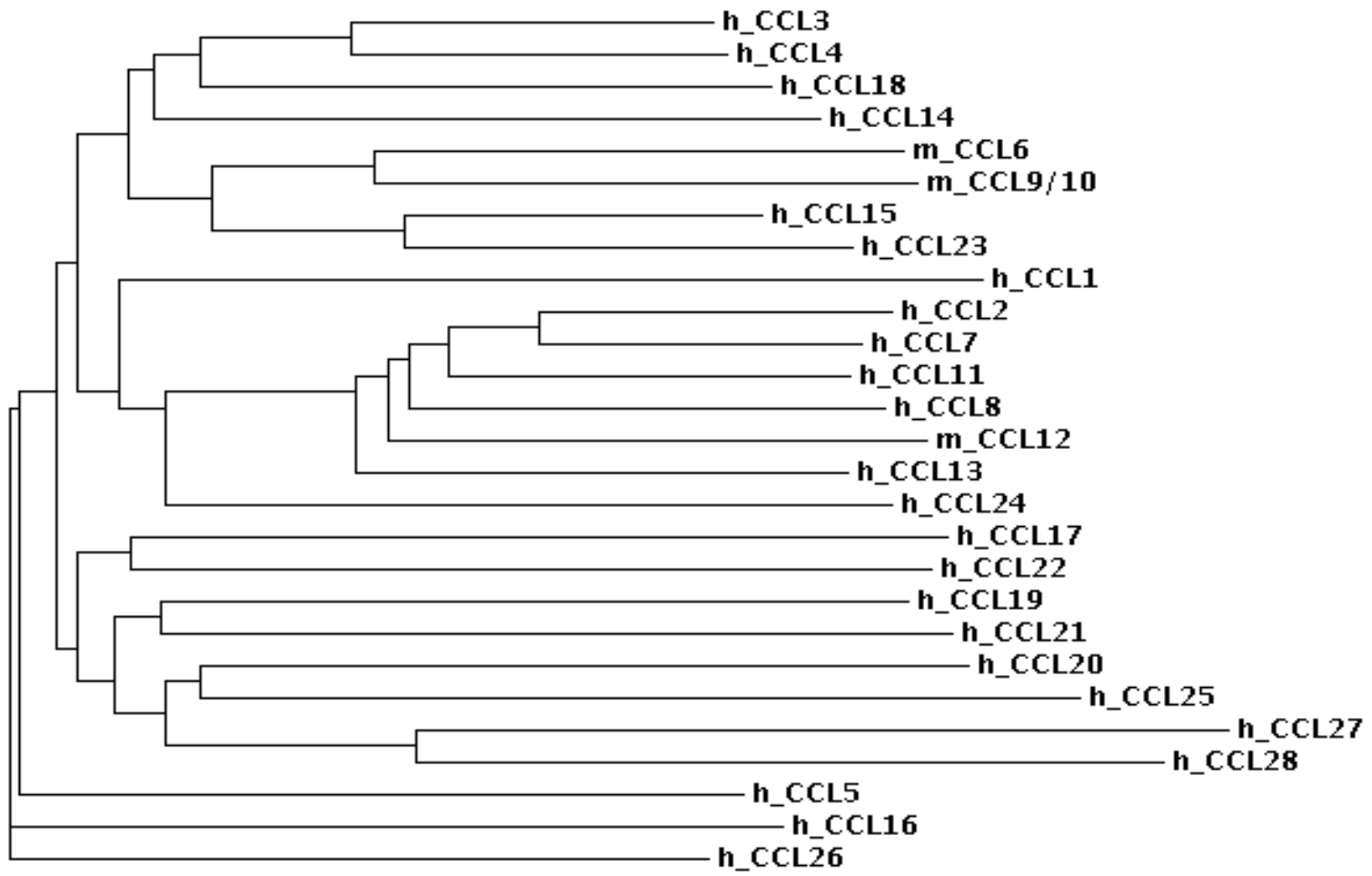


Figure S6

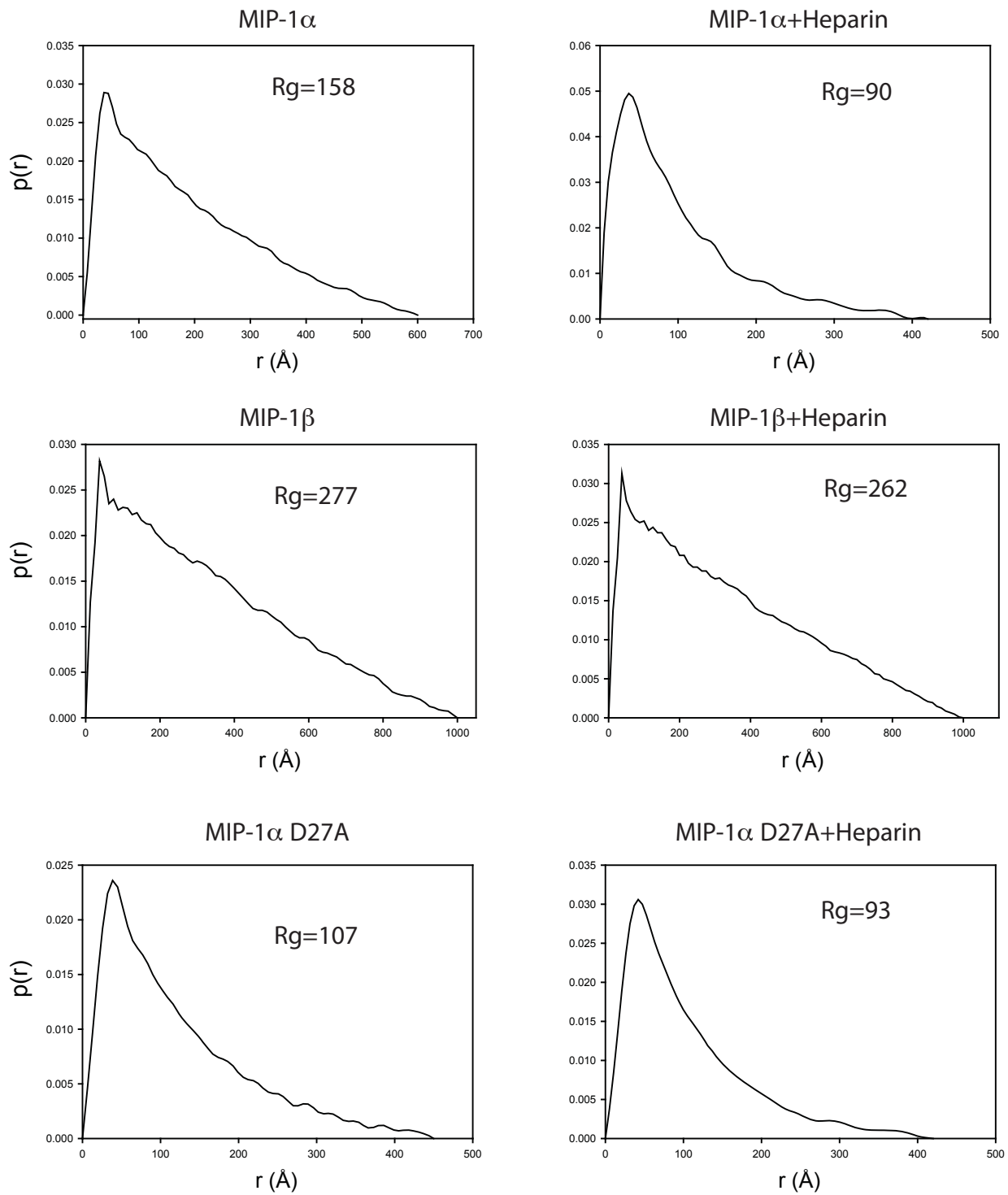
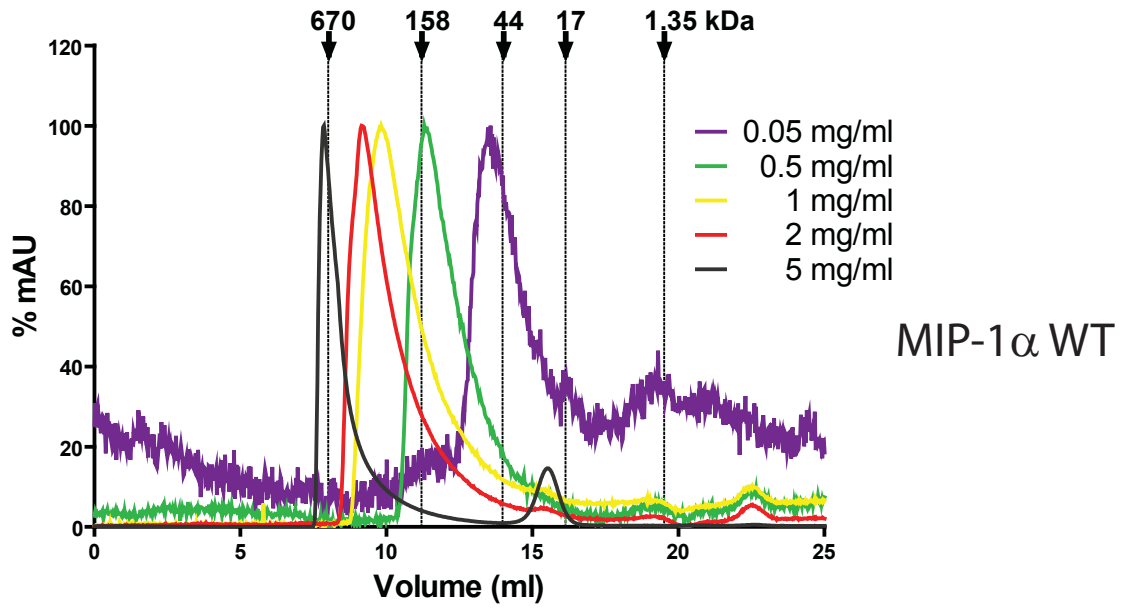
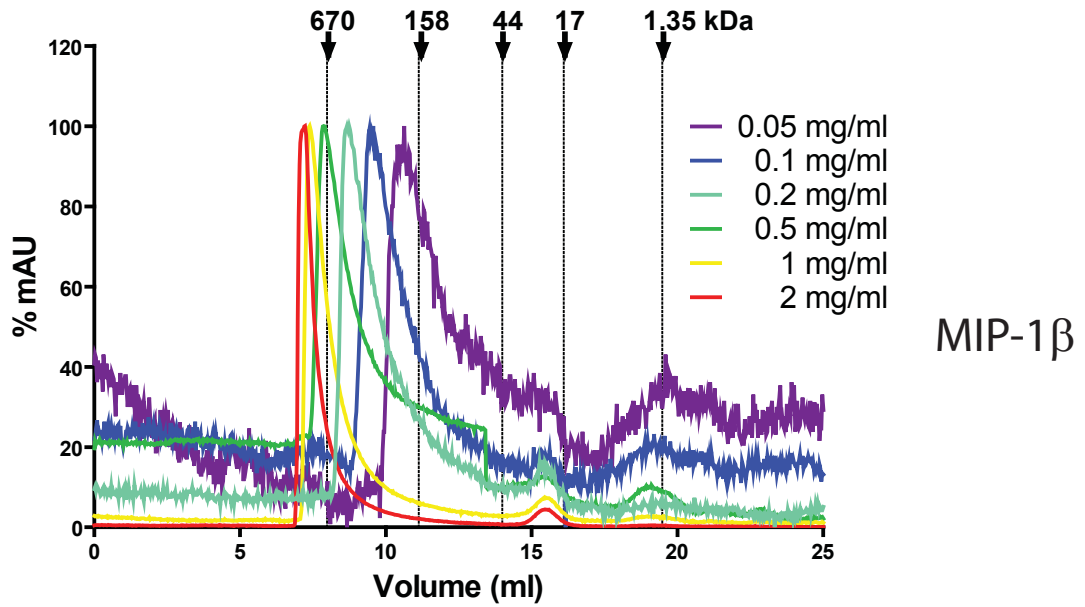


Figure S7

A



B



C

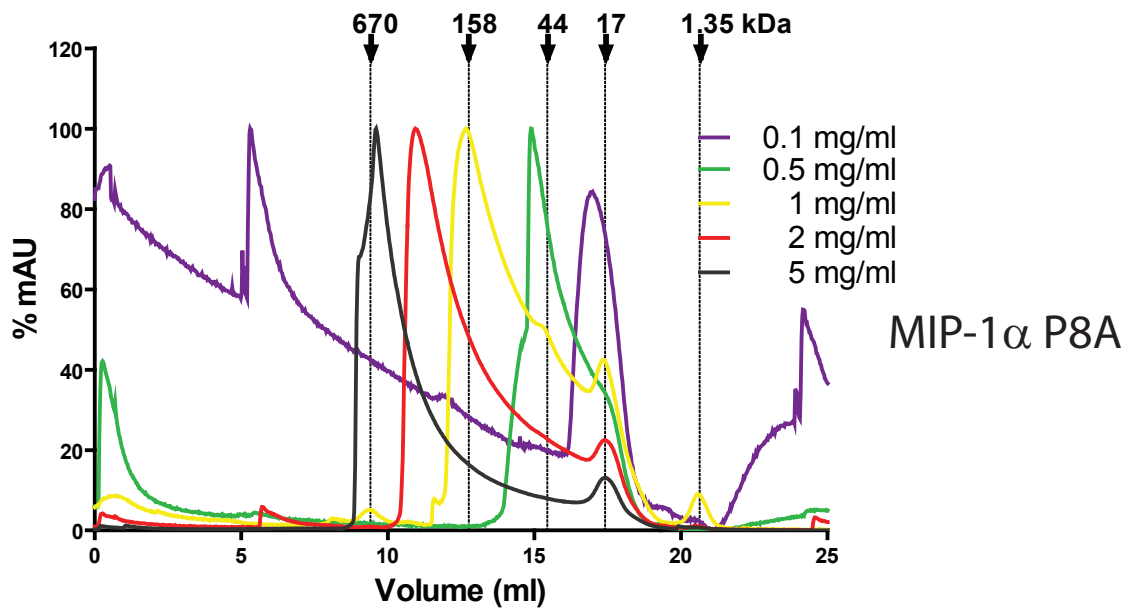
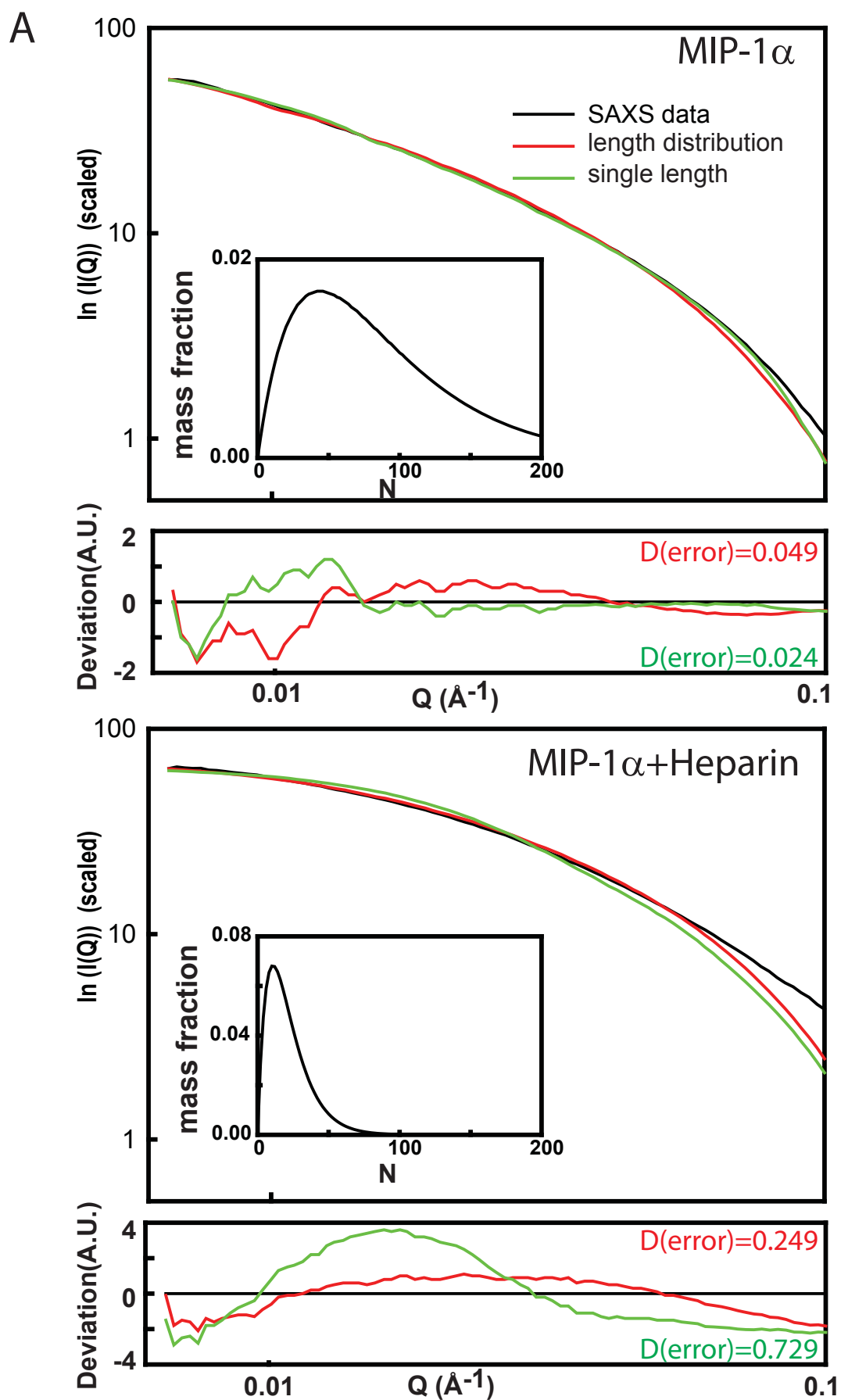
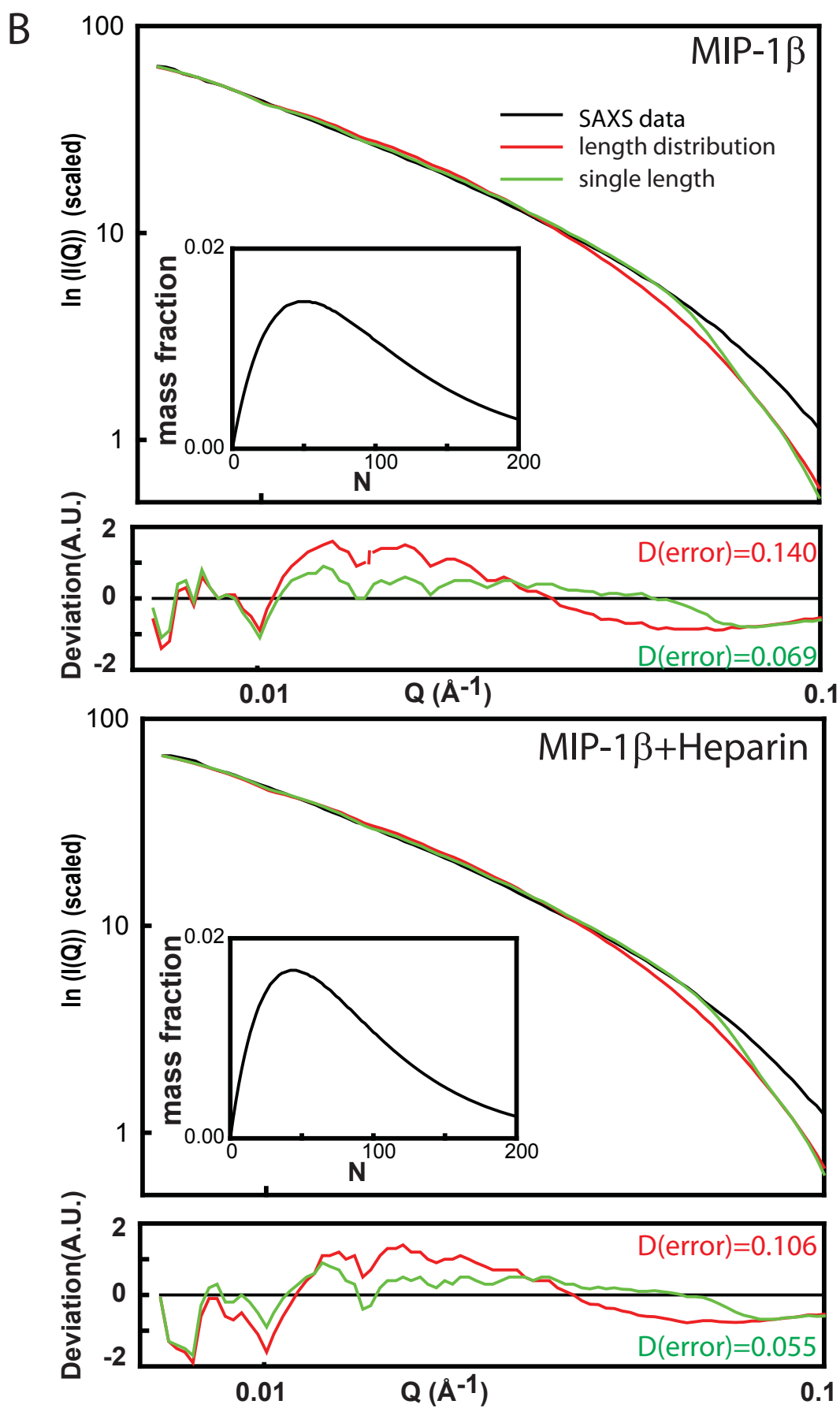


Figure S8





C

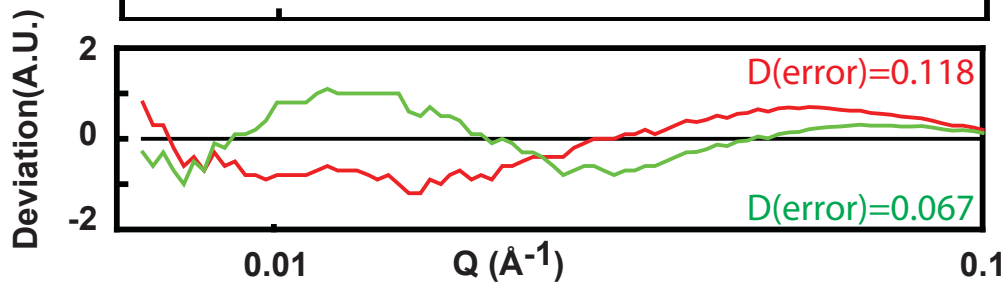
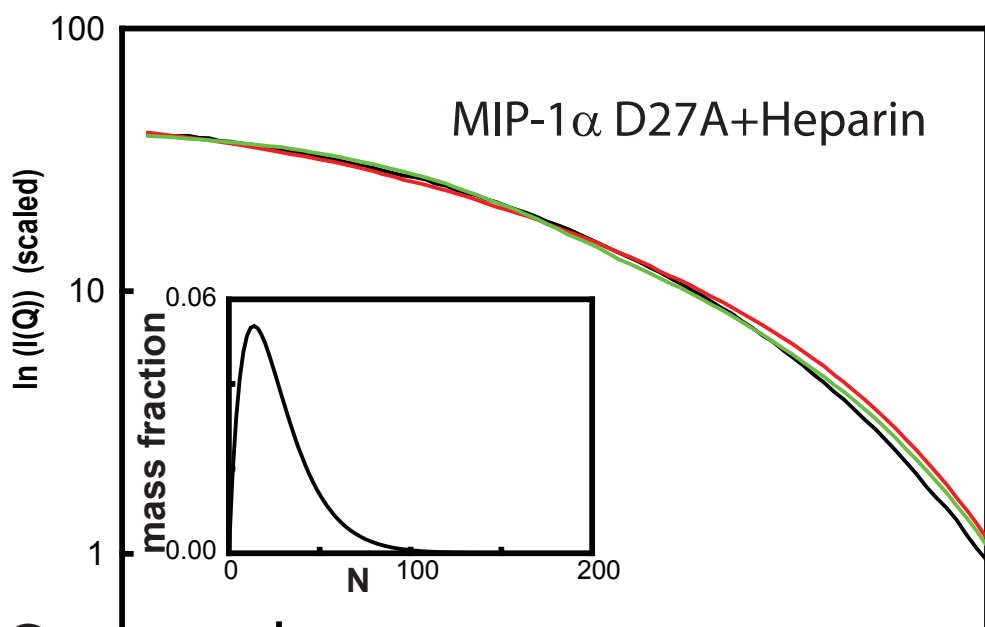
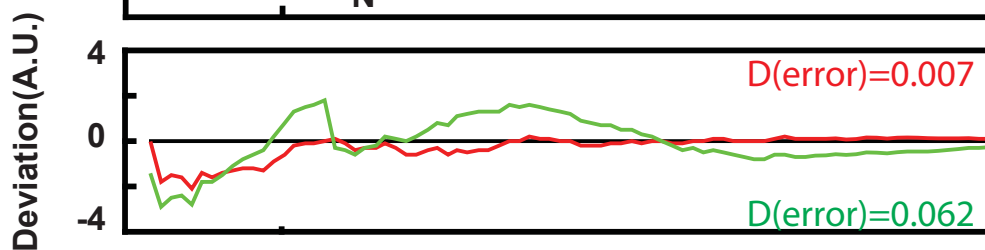
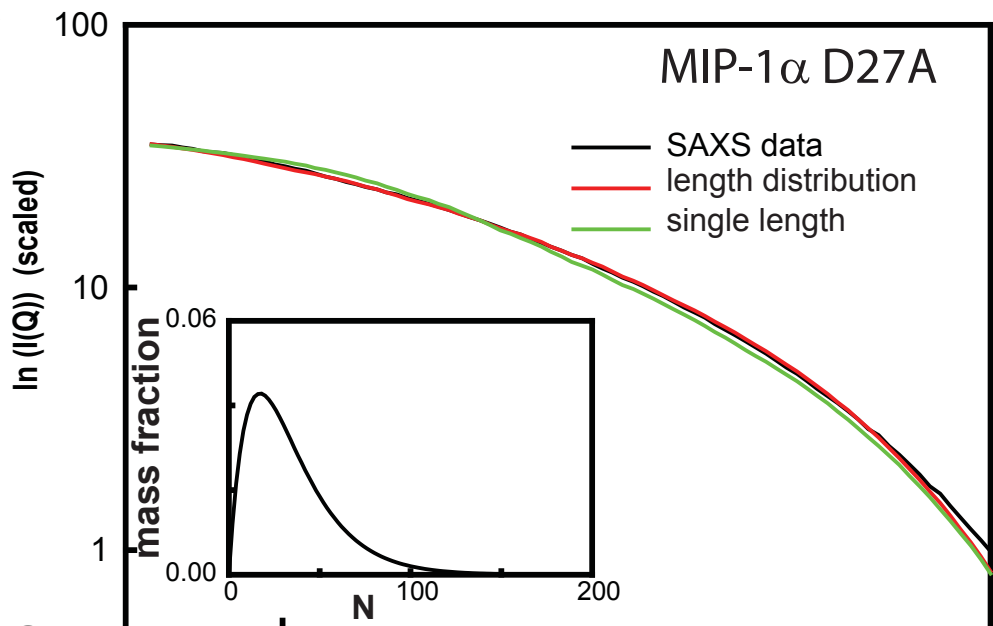
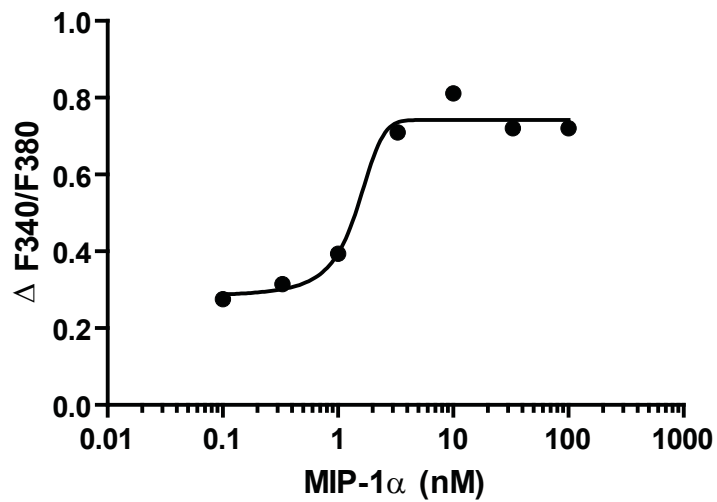


Figure S9

A



B

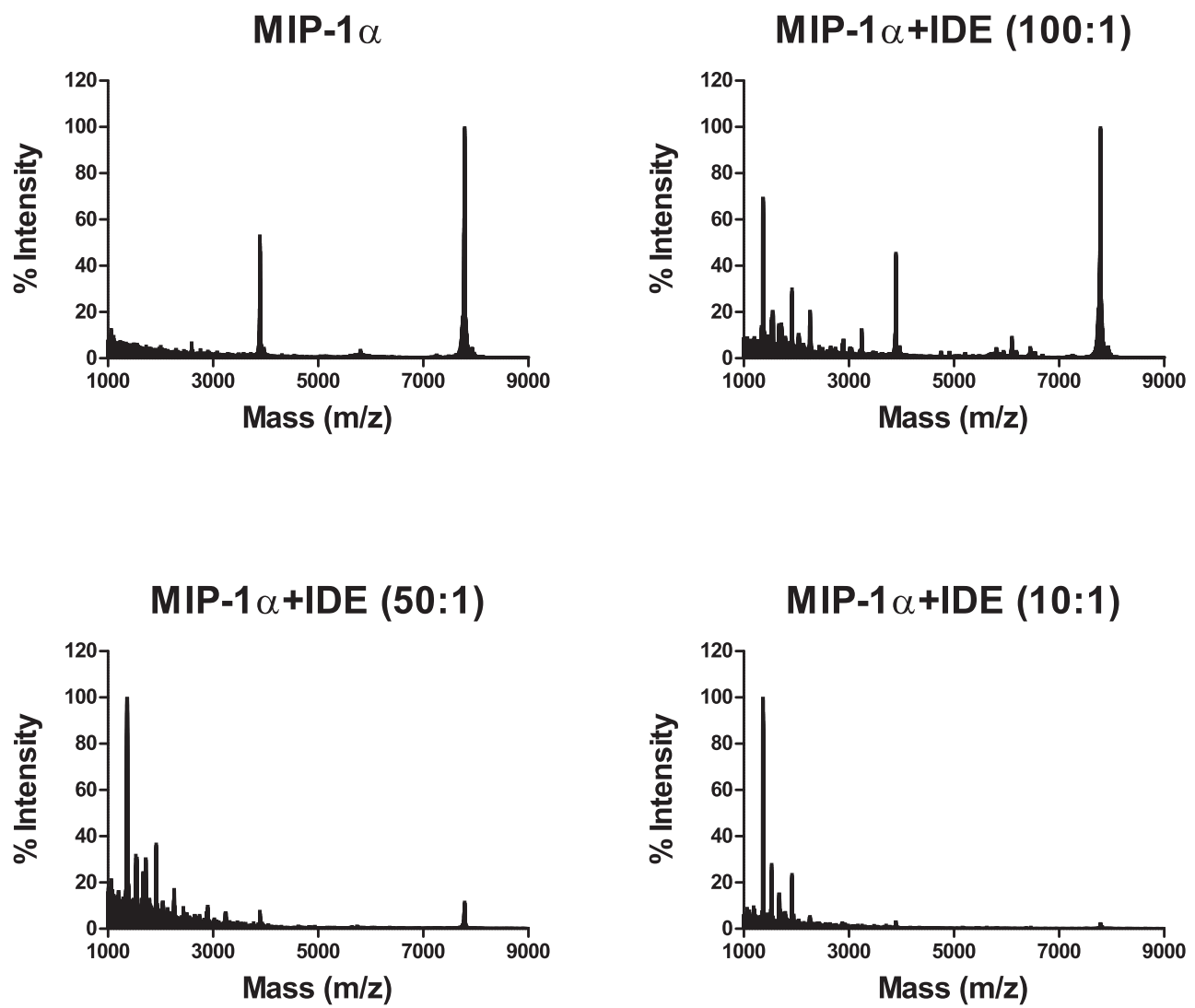


Figure S10

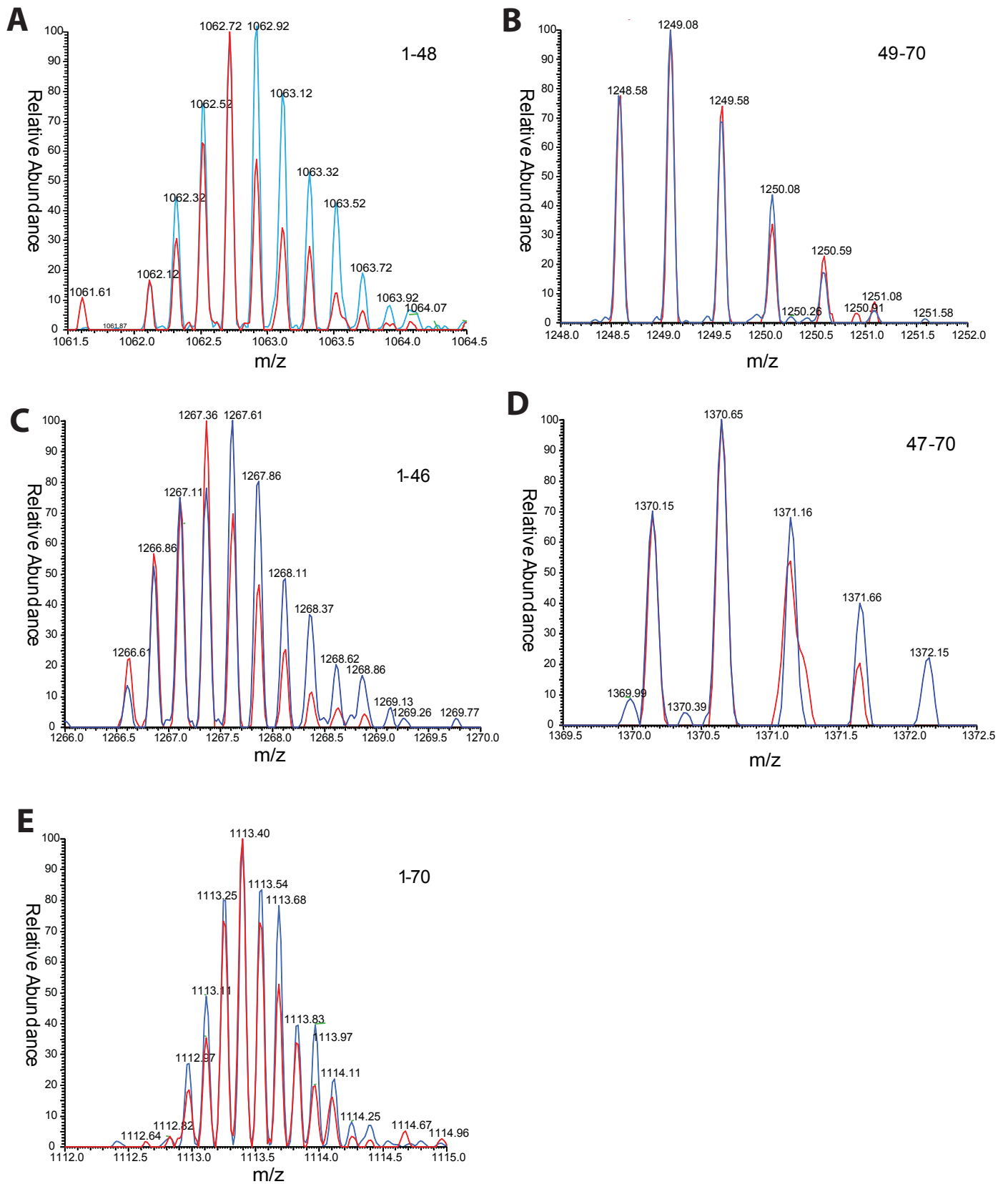
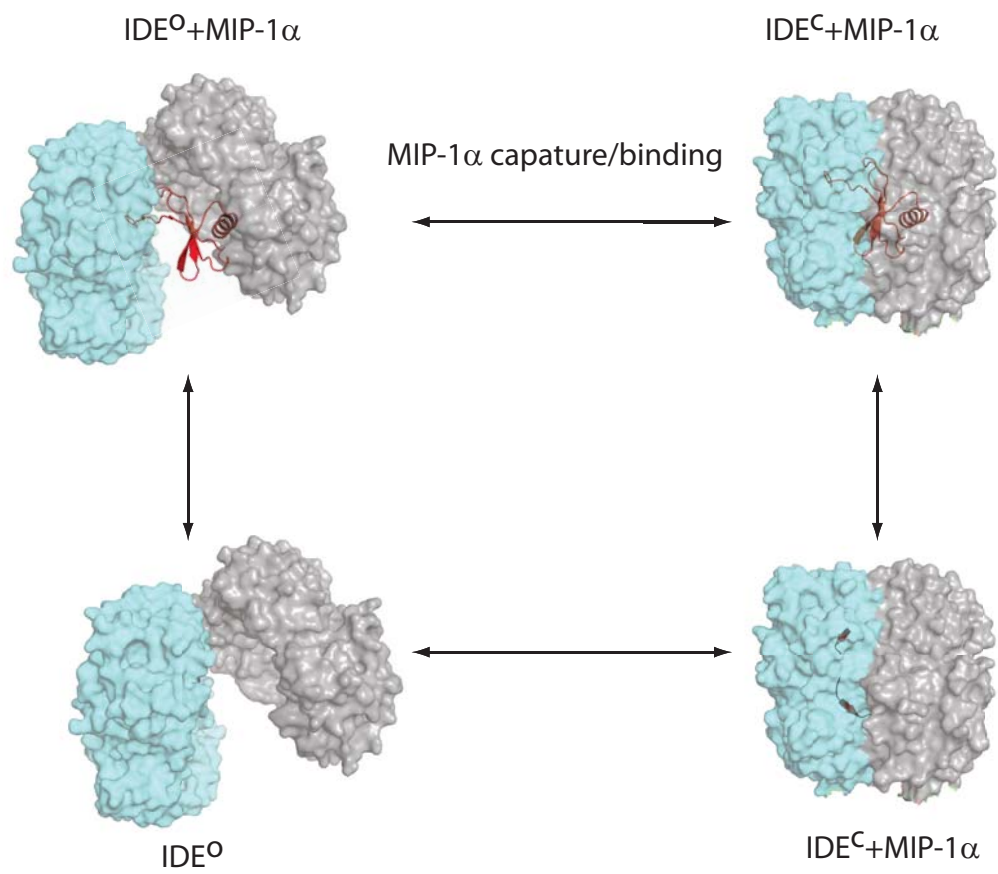


Figure S11



Supplemental table 1: Crystallographic statistics of Se_MIP-1 α (V3M/L63M)

Data collection			
	G7	G7	X53
Wavelength (Å)	0.97939(peak)	0.97953(inflexion)	0.97939
Space group	C2	C2	C2
Cell dimension(Å)			
a	309.5	309.2	308.2
b	178.0	178.0	178.6
c	77.4	77.5	77.4
α	90	90	90
β	89.8	89.9	90.1
γ	90	90	90
Resolution (Å)	50-3.1	50-3.2	50-2.7
Rsym (%) ^a	12.6(59.2) ^e	13.4(57.5)	10.8(51.5)
I/sigma	29.3(3.2) ^e	25.8(3.9)	21.3(2.5)
Redundancy ^b	7.2(7.1) ^e	7.2(7.2)	3.6(3.7)
Completeness (%)	99.9(100.0) ^e	99.9(100.0)	99.8(100.0)
Unique reflections	78012	75739	113405
Figure of merit	0.874		
Refinement			
R _{work} ^c			0.204
R _{free} ^d			0.241
No. atoms			
Protein			15920
Water			385
B-factors			
Protein			38.2
Water			41.3
r.m.s. deviations			
Bond lengths (Å)			0.021
Bond angles (°)			1.949
Ramachandran plot (%)			
Favorable region			93.1
Allowed region			6.7
Generously allowed region			0.2
Disallowed region			0

^a $R_{\text{merge}} = \Sigma (I - \langle I \rangle) / \Sigma \langle I \rangle$

^b $N_{\text{obs}} / N_{\text{unique}}$

^c $R_{\text{work}} = \Sigma_{hkl} ||F_{\text{obs}}| - |F_{\text{calc}}|| / \Sigma_{hkl} |F_{\text{obs}}|$

^d R_{free} , calculated the same as for R_{work} but on the 5% data excluded from the refinement calculation.

^e the outer resolution shell. Values in parentheses indicate the highest resolution shell

Supplemental Table-2

	MIP-1 α	MIP-1 α +Heparin	MIP-1 α D27A	MIP-1 α D27A +Heparin	MIP-1 β	MIP-1 β +Heparin
Radius of Gyration (Å)						
R_g (Guinier) ¹	130	80	100	80	150	140
R_g ($\rho(r)$) ²	160	90	100	90	280	260
R_c ³	17	15	17	19	17	17
Width (Å)						
Diameter ⁴	49	42	49	55	47	47
Length (Å)						
R_c+R_g (Guinier) ⁵	430	270	330	280	510	490
$R_c+R_g(\rho(r))$	540	310	370	320	960	910
D_{max} (Å)	600	420	450	420	950 ⁶	950 ⁶
Subunits in polymer						
SEC	90	70	4	20	230	200
R_c+R_g (Guinier) ⁷	40	25	30	25	46	44
$R_c+R_g(\rho(r))$ ⁷	50	30	30	30	90	80
Length distribution ⁸						
Single length ⁸	60	22	34	28	100	88
	50	24	34	28	72	64
Kd(nM) ⁹						
Length distribution ⁸	290	2130	890	1310	100	130

¹ The value of the radius of gyration (R_g) was derived from the Guinier approximation: $I(q) = I(0) \exp(-q^2 R_g^2/3)$, in the q -range $qR_g < 1.3$, where $I(q)$ is the scattered intensity and $I(0)$ is the forward scattered intensity

² The Radius of gyration (R_g) defined by $P(r)$ was calculated by using the following formula:

$$R_g^2 = \frac{\int_0^{D_{max}} r^2 P(r) dr}{\int_0^{D_{max}} P(r) dr}$$

³ The value of the radius of gyration (R_c) was derived from the Guinier approximation: $q \cdot I(q) \sim q \cdot I(0) \exp(-q^2 R_c^2/2)$, in the medium q -range, where $I(q)$ is the scattered intensity and $I(0)$ is the forward scattered intensity.

⁴ Diameter of the cross-section was calculated by using the following equation: $D = 2 \cdot 2^{1/2} \cdot R_c$

⁵ Length (L) was calculated by using the following equation $L = (12 \cdot (R_g^2 - R_c^2))^{1/2}$

⁶ listed D_{max} were maximal value based on the measurement limits of the experiment and generated by software GNOM

⁷ Subunits in polymer was calculated by following calculation: $N = L/22 \cdot 2$ while 22Å is the distance between two dimers.

⁸ Curve fitting use theoretical SAXS scattering

⁹ Dissociation constant corresponding to the breaking of a dimer-dimer bond. In accord with Eqs. (14) and (20) of the Supplemental Mathematical Modeling, this constant is calculated as $K_d = \frac{8c_i}{d^2 - 4}$, where c_i is the initial MIP monomer concentration and d , the average degree of polymerization, is determined from the "length distribution" fit to the SAXS data.

Table S3 Summary of mass spectrometry analysis of MIP1 α fragments resulting from IDE initial cleavage.

FRAGMENT	CAL MASS (M+H)	OBS MASS (M+H) (LC-FT-ICR)	Δ ppm	MS/MS (b/y ions)	O18 labeling
1-70	7783.713	7783.677	4.57		no ^a
1-45	4907.336	4907.321	3.07	b5-7, b16, b19; y5, y11	yes
46-70	2895.394	2895.388	1.94	b7-8, b ⁺⁺ 6-8, b ⁺⁺ 11-23; y10, y17, y ⁺⁺ 9, y ⁺⁺ 14-16, y ⁺⁺ 18, y ⁺⁺ 21, y ⁺⁺ 24-25	no
1-46	5063.438	5063.424	2.77	b4-b7, b12-15; y4-5, y7, y9-11, yes ^a y14	
47-70	2739.293	2739.288	1.68	b5-b16; y10-y15, y17	no ^a
1-48	5306.571	5306.557	2.65	b4-8, b11; y5, y10, y12,	yes ^a
49-70	2496.160	2496.153	2.74	b5, b8-10, b12-17; y7-10, y12- 14, y17	no ^a
1-18	1864.820	1864.814	3.18	b4-13, b15; y3-15	yes
19-70	5937.910	5937.907	0.47	b8-9; , b ⁺⁺ 12, b ⁺⁺ 18-21, b ⁺⁺ 25, b ⁺⁺ 35; y7-13, y17, y ⁺⁺ 13-14, y ⁺⁺ 17-20, y ⁺⁺ 22, y ⁺⁺ 28, y ⁺⁺ 25	no

Summary of mass spectrometry analysis of MIP-1 α fragments resulting from IDE initial cleavage. Calculated and observed masses are shown as singly charged monoisotopic mass (M+H). Observed b/y ions according to the specific fragment from tandem mass spectrometry analysis are listed. MIP-1 α was digested with IDE in 50% ¹⁸O water. The fragments labeled with ¹⁸O are marked as “yes” in the last column. ^aExample spectrums of ¹⁸O labeling experiment were shown in Fig. S10.

Table S4 Summary of mass spectrometry analysis of IDE degraded MIP1 α fragments .

FRAGMENT	CAL MASS (M+H)	OBS MASS (M+H) (LC-FT-ICR)	OBS MASS (M+H) (MALDI-TOF)	Δ ppm
4-18	1593.667	1593.660	N/D	4.83
5-18	1522.630	1522.620	N/D	6.63
6-18	1451.5929	1451.597	N/D	2.83
8-18	1235.518	1235.516	N/D	1.79
8-46	4434.136	4434.126	N/D	2.11
21-46	2976.492	2976.476	N/D	5.68
25-46	2490.250	2490.306	N/D	22.69
26-46	2377.186	2377.182	N/D	1.40
27-46	2306.149	2306.153	N/D	1.78
30-46	1880.990	1880.979	N/D	5.95
31-46	1751.947	1751.945	N/D	1.26
26-48	2620.319	2620.310	N/D	3.39
17-28	1451.728	N/D	1451.724	2.55
18-28	1364.696	N/D	1364.693	1.97
14-24	1340.659	N/D	1340.661	1.26
1-13	1270.544	N/D	1270.720	138.52
15-27	1552.775	N/D	1552.762	8.63